Progress towards Building a Quantum Network Node using Near-Concentric Resonant Cavities

by

Christopher B. Young

A dissertation submitted in partial fulfillment of
the requirements for the degree of

Doctor of Philosophy
(Physics)

at the
UNIVERSITY OF WISCONSIN-MADISON
2022

Date of final oral examination: 01/21/2022

The dissertation is approved by the following members of the Final Oral Committee:

Mark Saffman, Professor, Physics

Thad Walker, Professor, Physics

Deniz Yavuz, Professor, Physics

Mikhail Kats, Associate Professor, Electrical and Computer Engineering

Contents

List of Figures

Abstract

This thesis reports on the progress made towards the design and construction of a neutral atom quantum network node using near-concentric cavities. Development of quantum network nodes is an outstanding problem towards the construction of a distributed quantum network. Fast generation of atom-atom entanglement is an important condition to make a functioning quantum node. We propose a design that uses a near-concentric cavity which is large enough to form a MOT directly inside of the cavity, while having a small enough mode volume that the photon collection efficiency is 48%: better then any free space collection method using a high-NA lens. Furthermore, the design is compact and scalable. A chip based design will limit the number of moving parts and external optics, and make the device easier to use. Future goals are to interpose a duel species array into the cavity, creating a quantum node that contains memory and processing, as well as an interface between matter qubits and photons that mediate entanglement distribution. In this work an analysis is presented showing the efficacy of the proposed platform and how it has the capability of surpassing existing entanglement generation rates using neutral atoms. Design, construction and testing of the device are ongoing.

Additionally, in this thesis there is a discussion about the work done towards using neutral Rubidium 87 atoms to make Rydberg-mediated ensemble qubits. We worked to improve and fix the existing apparatus including the implementation of an automatic beam alignment system which achieved a 1σ pointing stability of 60 nm between our dipole traps and the 780nm addressing beam. Multiple improvements were made to lower laser noise and stabilize experimental conditions. Problems arising in the experiment and the solutions taken to address those problems are discussed.

Chapter 1

Introduction

Companies including Google, IBM, Intel, and many others have all invested heavily in quantum information research. The main resource that all of these projects share, regardless of their individual merits, is entanglement. Entanglement is a strange property of certain quantum systems where by two or more particles exist in a state that can not be described as a product of two individual states. That is to say, that each particle of the system cannot be described independently of the others. They are entangled. This is what allows quantum processors to theoretically out perform thier classical counterparts [70]. Given the state of current architectures however, scaling quantum processors to a size that will allow them to truly outperform classical machines is still not attainable. Currently the largest quantum processors have on the order of 10^2 qubits and are almost entirely dominating by superconducting architectures. While it has been claimed by that we have been able to show quantum supremacy [4, 80], these have typically been under very specific conditions. Meanwhile, classical machines have also continued to develop at an extremely fast pace with transistors densities in the hundreds of millions per square millimeter and increasing(although they are approaching a fundamental limit). In order for quantum computer to really realize their full potential, they will need to vastly increase in size

IBM Eagle	127 Superconducting qubits
USTC Jiuzhang	76 photonic qubits
Google Bristlecone	72 Superconducting qubits
IBM Manhatten	65 Superconducting qubits
Intel Tangle Lake	49 Superconducting qubits

Table 1.1: To date largest quantum processors

and power. It is therefore important for a quantum computing architecture to be scalable. This is why neutral atoms are very promising; they have high scalability. Since neutral atoms have no charge, they can be be densely packed in tight arrays containing hundreds of atoms that are only a few hundred microns across[10, 69, 62, 52]. Even topologically intricate 3D arrays have been demonstrated[6]. Neutral atoms also have long qubit lifetimes, and don't interact much unprovoked making ideal for quantum memory. And while there may be a quantum processor built in the future that is a stand alone unit with millions of qubits, that is far beyond the engineering capabilities of today. Such a device will still need to be able to store and transmit quantum information to function. Since quantum states can not be copied, this means that entanglement between quantum memory and communication qubits is necessary for the transmission of entanglement. Neutral atoms make for good quantum memory but they do not make good communication qubits. Photons on the other hand are an ideal candidate for communication qubits as they can travel long distances in optical fibers without information loss. Atoms and photons also interact very strongly, and this makes atom-photon systems an ideal candidate for quantum nodes and repeaters: devices which can be chained together to transfer entanglement from two spatially separated processors. The first half of this thesis will discuss plans to build a duel-species neutral atom quantum network node based of of near-concentric resonant optical cavities. The design goal is to construct a quantum node capable of

rapid and high fidelity entanglement generation, in a compact form factor that lends itself to high scalability. Using a resonant cavity for photon collection gives collection efficiency superior to lenses or mirrors, while also being smaller and less cumbersome. While small cavities made from the faces of optical fibers can provide almost unity photon collection efficiency, their small size prohibits forming a MOT directly in the cavity. Atoms can be shuttled into the cavity, but this adds time and complexity [26]. Cavities with lengths in the cm range are large enough to form a MOT directly inside of the cavity. Because the time and complexity associated with shuttling the atoms into a fiber cavity is large, using a longer cavity can improve the atom-atom entanglement generation rate. With the designs proposed here we plan to construct a neutral atom quantum node which will have atom-atom entanglement generation rate of greater than 1500Hz.

The second part of this thesis discusses the work and progress towards using Rb87 atoms as ensemble qubits. As was previously mentioned, qubits encoded onto the hyper-fine levels of neutral atoms are a very promising platform for quantum processors. Neutral atoms can be deterministically loaded into dipole traps using optical tweezers [10, 69, 52, 6]. An alternative method is to load more than one atom into the trap as one has to simply overlap a cloud of cold atoms with optical tweezers for short period of time. These atomic ensembles are comprised of multiple identical atoms, each of which contains the ability to store quantum information. The encoding scheme uses a logical qubit basis which consists of the ground state and a maximally entangled W-state where a single excitation is shared amongst all the atoms in the ensemble. In this thesis I will discuss the progress and difficulties we experienced in building and maintaining an apparatus for preparing and using ensembles of Rb87 atoms and how we addressed those problems.

Chapter 2

Theory and Background

2.1 Two Level Atom

The electrons in atoms can occupy an infinite number of discrete energy levels, with approximate energy values given by the Bohr Energy level equation:

$$E_{\mathrm{n}} = \frac{-m_e c^2 \alpha^2 Z_{\mathrm{eff}}^2}{2n^2}$$

(2.1)

where m_e is the electron mass and α is the fine structure constant. These energy levels are, to very good approximation, accurate for the one electron atom hydrogen, but for even helium the spin-orbit interactions are large enough that they become necessary to account for. These energy level shift come from the interactions of the electron spin and the orbital angular momentum of the electron. These are the so called fine energy shifts. There are even more subtle shifts caused from the interaction of the spin of the nucleus and the electron which give rise to hyper-fine structure. These interactions lead to a rich structure of energy levels. For an atom like Rb, which only

has a single valence electron, it would be prohibitively difficult to fully account for all the energy levels of the atom. However, in the case where the electron is only being driven by a field which is near or on-resonance to a single transition between two energy levels, the Hamiltonian of the electron can be effectively reduced to have only two levels. Let us consider the two energy levels, which are eigenstates of our system, as:

$$|\mathrm{g}\rangle = \begin{pmatrix} 0 \\ 1 \end{pmatrix} |e\rangle = \begin{pmatrix} 1 \\ 0 \end{pmatrix} \tag{2.2}$$

Where $|0\rangle$ is the ground state of our system, and $|1\rangle$ is our excited state. Our Hamiltonian for the atom with no driving field is:

$$\mathrm{H}_0 = \hbar\omega_\mathrm{e} |\mathrm{e}\rangle \langle \mathrm{e}| + \hbar\omega_\mathrm{g} |\mathrm{g}\rangle \langle \mathrm{g}|$$

2.1.1 AC stark shift

When the system is exposed to an oscillating electric field, it interacts via the electric dipole interaction,$-\hat{d} \cdot E$, where d is the dipole moment operator $-e\hat{r}$ and E is the electric field driving the interaction. Since the dipole moment operator is a rank one tensor operator, it can only connect states of opposite parity to first order. The diagonal components of this interaction are zero as connecting a state to itself would break parity conservation (to first order) thus the interaction Hamiltonian is:

$$\mathrm{H_i} = \begin{pmatrix} 0 & -\mathrm{d} \cdot \mathrm{E} \\ -\mathrm{d}^* \cdot \mathrm{E} & 0 \end{pmatrix}$$

And the total Hamiltonian can be written as

$$\mathrm{H_{tot}} = \mathrm{H}_0 + \mathrm{H_i} = \begin{pmatrix} \hbar\omega_g & -\mathrm{d} \cdot \mathrm{E} \\ -\mathrm{d}^* \cdot \mathrm{E} & \hbar\omega_e \end{pmatrix}$$

Where E is an electromagnetic field $\mathrm{E} = \varepsilon_0 e^{-i\omega t} + \varepsilon_0^* e^{i\omega t}$. If the frequency of the driving field is such that the detuning, $\delta = \omega - (\omega_e - \omega_g)$, is small than we can make the rotating wave approximation and rewrite the Hamiltonian in the dressed state as

$$\mathrm{H_d} = \begin{pmatrix} \frac{-\hbar\delta}{2} & \frac{\hbar\Omega}{2} \\ \frac{\hbar\Omega}{2} & \frac{\hbar\delta}{2} \end{pmatrix}$$

The eigenvalues of this matrix, which represent the atomic energy levels in the presence of this driving field are given by

$$\mathrm{E_i} = \pm\frac{\hbar}{2}\sqrt{\delta^2 + \Omega^2} = \pm\frac{\hbar\Omega'}{2} \tag{2.3}$$

The eigenstates of this system are the dressed states, and they are superpositions of the un-driven atomic energy levels

$$|0\rangle = \sin\left[\arctan\left[\frac{\Omega}{\Omega' - \delta}\right]\right]|e\rangle + \cos\left[\arctan\left[\frac{\Omega}{\Omega' - \delta}\right]\right]|g\rangle$$
$$|1\rangle = \cos\left[\arctan\left[\frac{\Omega}{\Omega' - \delta}\right]\right]|e\rangle - \sin\left[\arctan\left[\frac{\Omega}{\Omega' - \delta}\right]\right]|g\rangle$$

In the limit that the detuning is zero, then the splitting of the dressed states is proportional to the Rabi-frequency Ω. In the limit that the detuning is very large, then the dressed states become the un-driven atomic states. This splitting of the energy levels in the presence of a driving electric dipole field is called Autler-Townes Splitting.

2.2 Microwave Rotations

One way to do single atom rotations between the hyper-fine basis states other than Raman is to rotate the atoms globally using a microwave pulse. The microwaves can drive magnetic dipole transitions(as opposed to electric dipole) and directly drive a transition between the hyper-fine levels.

Consider an electron orbiting the nucleus of an atom at a distance $\vec{r}$. This can be thought of as a current loop with radius r and

$$\mathrm{I} = q\frac{\vec{v}}{2*\pi r}$$

This would mean that our electron would have an orbital magnetic moment:

$$\mu_L = A \times I = \frac{q}{2}\vec{r} \times \frac{\vec{p}}{m_e} = \frac{q}{2m_e}L$$

Likewise, we must also consider the intrinsic magnetic moments of the electron and the nucleus, which have similar forms, scaled by a factor g, the gyromagnetic ratio.

$$\mu_S = \frac{qg_s}{2m_e}S$$
$$\mu_I = \frac{qg_I}{2m_e}I$$

This means that our total interaction Hamiltonian for a Magnetic Dipole transition (M1) looks like

$$\mu \cdot B = \frac{q}{2m_e}(L + g_s S + g_I I) \cdot \vec{B}$$

In the case relevant for our discussion here, we are driving a transition between hyper-fine levels within the $5S_{1/2}$ ground state of Rb_{87}, L = 0. Additionally, g_S = 2.0(Neglecting higher order corrections) and $g_I = 0.0$. Therefore, for our discussion of global rotations, the Interaction Hamiltonian becomes:

$$H_i = \frac{q}{m_e}S \cdot \vec{B}$$

If we enforce a quantization axis along $\vec{z}$ using a weak magnetic field, and we wish to drive our M1 transition between the $m = 0$ hyper-fine levels of our ground state, then our B field in this case is that of an electromagnetic wave linearly polarized along the z-axis. The form of our B field is:

$$\vec{B} = \frac{B_0}{2}(e^{-i\omega t} + e^{i\omega t})(\vec{k} \times \vec{E})$$

and our Interaction Hamiltonian is

$$H_i = \frac{q}{m_e} S \cdot \frac{B_0}{2}(e^{-i\omega t} + e^{i\omega t})(\vec{k} \times \vec{E})$$

Thus, in the $|M_s, M_I\rangle$ basis the M1 transition looks like:

$$\epsilon \cdot d_{eg} = \langle F = 2, m = 0| \, H_i \, |F = 1, m = 0\rangle$$
$$|F = 2, m = 0\rangle = \frac{1}{\sqrt{2}}(|\tfrac{-1}{2}, \tfrac{+1}{2}\rangle + |\tfrac{+1}{2}, \tfrac{-1}{2}\rangle)$$
$$|F = 1, m = 0\rangle = \frac{1}{\sqrt{2}}(|\tfrac{-1}{2}, \tfrac{+1}{2}\rangle - |\tfrac{+1}{2}, \tfrac{-1}{2}\rangle)$$

We can now use the formula for the Rabi Frequency and obtain

$$\Omega_{M1} = \frac{\epsilon \cdot d_{eg}}{\hbar} = B_0 \frac{q}{4m_e} = B_0 \frac{\mu_B}{2\hbar}$$

Where μ_B is the Bohr magneton.

Since $B_0 = \frac{1}{\sqrt{\epsilon_0 \mu_0}} E_0$, we can calculate the expected Rabi frequency using the MW power at the atoms. For a power of 3W emitted from a horn with an opening of 2" x 1.5", assuming uniform radiation since the horn is quite close to the atoms, then the Rabi frequency will be

$$\Omega_{M1} = 2\pi \times \frac{\mu_B \sqrt{\frac{2P_{MW}}{A\epsilon_0 c}}}{2\hbar c}$$
$$\Omega_{M1} \approx 2\pi \times 8kHz$$

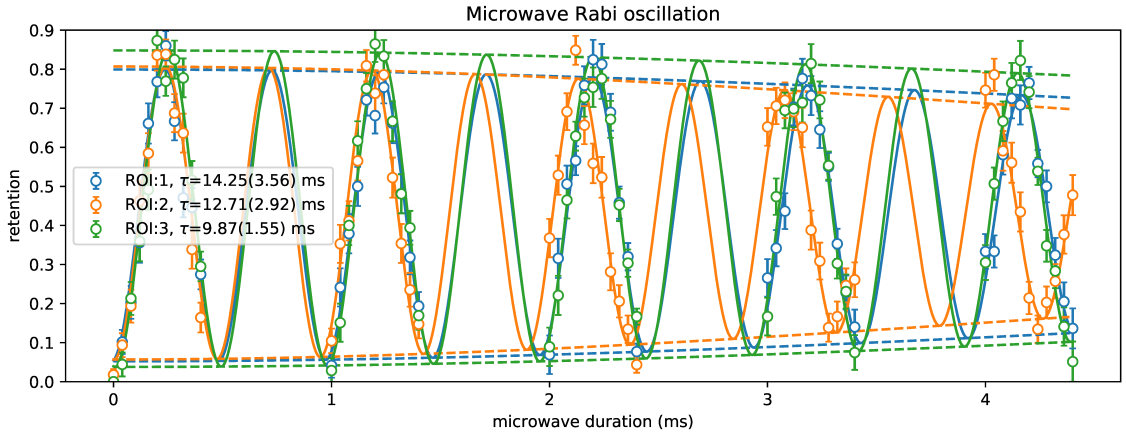

Figure 2.1: Example Microwave Rab showing the dephasing in the three center dipole traps. Data collected by Minho Kwon 2018.08.26

2.3 Jaynes-Cummings Model: Atom-Cavity Interaction

Consider the case of an atom inside of an optical cavity which only supports a few modes widely spaced in frequency. The electric field mode inside of this cavity is of the form

$$\hat{E} = e(\frac{\hbar\omega}{\epsilon_0 V})^{\frac{1}{2}}(\hat{a} + \hat{a}^\dagger)\sin(kz) \tag{2.4}$$

If we define operators σ_i such that

$$\sigma_+ = \sigma_-^\dagger = |e\rangle\langle g|$$

$$\sigma_z = |e\rangle\langle e| - |g\rangle\langle g|$$

$$[\sigma_+, \sigma_-] = \sigma_z$$

$$[\sigma_z, \sigma_\pm] = 2\sigma_\pm$$

then we can write the dipole operator, $\hat{d}$, as

$$\hat{d} = d(\sigma_+ + \sigma_-)$$

since only the off diagonal terms of the dipole operator are nonzero due to parity. This means that the interaction Hamiltonian is

$$\hat{H}_i = -d(\frac{\omega\hbar}{\epsilon_0 V})^{\frac{1}{2}}(\sigma_+ + \sigma_-)(\hat{a} + \hat{a}^\dagger)\sin(kz) \tag{2.5}$$

If we dress the states such that the zero energy is defined as being half way between the ground and excited states, then we can write the free-atomic and free-field Hamiltonians as

$$\hat{H}_A = \frac{1}{2}\hbar\omega_0\sigma_z$$
$$\hat{H}_F = \hbar\omega\hat{a}^\dagger\hat{a}$$

And our complete Hamiltonian becomes

$$\hat{H} = \hat{H}_i + \hat{H}_A + \hat{H}_F$$
$$\hat{H} = \frac{1}{2}\hbar\omega_a\hat{\sigma_z} + \hbar\omega_c\hat{a}^\dagger\hat{a} + \hbar g(\mathbf{r})(\hat{\sigma_+} + \hat{\sigma_-})(\hat{a} + \hat{a}^\dagger)$$

where $g(\mathbf{r}) = -d(\frac{\omega}{\epsilon_0 V\hbar})^{\frac{1}{2}}sin(kz)$ is the coupling. We can further simplify the Hamiltonian by making the Rotating Wave Approximation (RWA). This allows us to neglect the terms in the Hamiltonian that go like $\hat{\sigma_+}\hat{a}^\dagger$ or $\hat{\sigma_-}\hat{a}$, which both nominally describe processes that violate energy conservation and can therefore only happen on timescales that are dictated by the uncertainty principle. Removing those terms we have

$$\hat{H} = \hat{H}_i + \hat{H}_A + \hat{H}_F$$
$$\hat{H} = \frac{1}{2}\hbar\omega_a\hat{\sigma_z} + \hbar\omega_c\hat{a}^\dagger\hat{a} + \hbar g(\mathbf{r})(\hat{\sigma_+}\hat{a} + \hat{\sigma_-}\hat{a}^\dagger) \tag{2.6}$$

which is the Jaynes-Cummings Hamiltonian [39]. If you solve Eq 2.6 by diagonalizing it, you find that the eigenstates of the system are of the form

$$|n,+\rangle = \cos\theta\,|n-1,e\rangle + \sin\theta\,|n,g\rangle$$

$$|n,-\rangle = -\sin\theta\,|n-1,e\rangle + \cos\theta\,|n,g\rangle$$

$$\theta = \arctan\frac{g(\mathbf{r})}{\sqrt{g(\mathbf{r})^2 + (\frac{\Delta_{ac}}{2})^2} - \frac{\Delta_{ac}}{2}}$$

If the coupling $g(\mathbf{r})$ is zero, then the cavity-atom states are just the product states of the atom and cavity eigenstates. If $g(\mathbf{r})$ is non-zero, then the states are coupled together. If the cavity frequency and atom frequency are the same, then $\Delta_{ac} = 0$ and the states become maximally entangled Bell-states

$$|n,\pm\rangle = \frac{1}{\sqrt{2}}\left(|n-1,e\rangle \pm |n,g\rangle\right)$$

Further discussion of a single atom in a resonant cavity is in section 4.3

2.4 Fabry-Perot Resonators

A Fabry-Perot Resonator is in general two mirrors facing each other. Each of the mirrors has a radius of curvature R_i, and they are separated by a distance $\mathrm{L}_{\mathrm{cav}}$, the cavity length. Photons inside of the cavity bounce between the mirrors, sometimes hundreds of thousands of times, before they exit. While inside of the cavity, the photons will interfere with each other, such that only certain modes of the cavity are supported. In general, not all mirror configurations have such modes, but if they do then the cavity is considered stable. The stability condition for a cavity can be derived by considering whether a Gaussian beam mode can perfectly fit within the cavity. You can write the stability condition in terms of the cavity length and mirror

curvatures as[71]

$$0 \leq \left(1 - \frac{\mathrm{L_{cav}}}{R_1}\right)\left(1 - \frac{\mathrm{L_{cav}}}{R_2}\right) \leq 1 \tag{2.7}$$

Typically this is written in the following form

$$0 \leq \mathrm{g_1 g_2} \leq 1 \tag{2.8}$$

where the stability parameter g_i has been substituted for $\left(1 - \frac{\mathrm{L_{cav}}}{R_i}\right)$. In terms of the stability parameter, the waist size in the center of the cavity can be written as[71]

$$\omega_0^2 = \frac{\mathrm{L_{cav}}\lambda}{\pi}\sqrt{\frac{\mathrm{g_1 g_2}(1 - \mathrm{g_1 g_2})}{(\mathrm{g_1} + \mathrm{g_2} - 2\mathrm{g_1 g_2})^2}} \tag{2.9}$$

where λ is the wavelength of the light resonating in the cavity. The waist size on mirror i with opposing mirror j can be written as

$$\omega_\mathrm{i}^2 = \frac{\mathrm{L_{cav}}\lambda}{\pi}\sqrt{\frac{\mathrm{g_j}}{\mathrm{g_i}\,(1 - \mathrm{g_i g_j})}} \tag{2.10}$$

These equations only give real answers if Eq. 2.7 holds. Fig 2.2 shows a plot of the space spanned by g_1 and g_2 and the possible configurations of stable cavities. The red 45 degree line represents symmetric cavities.

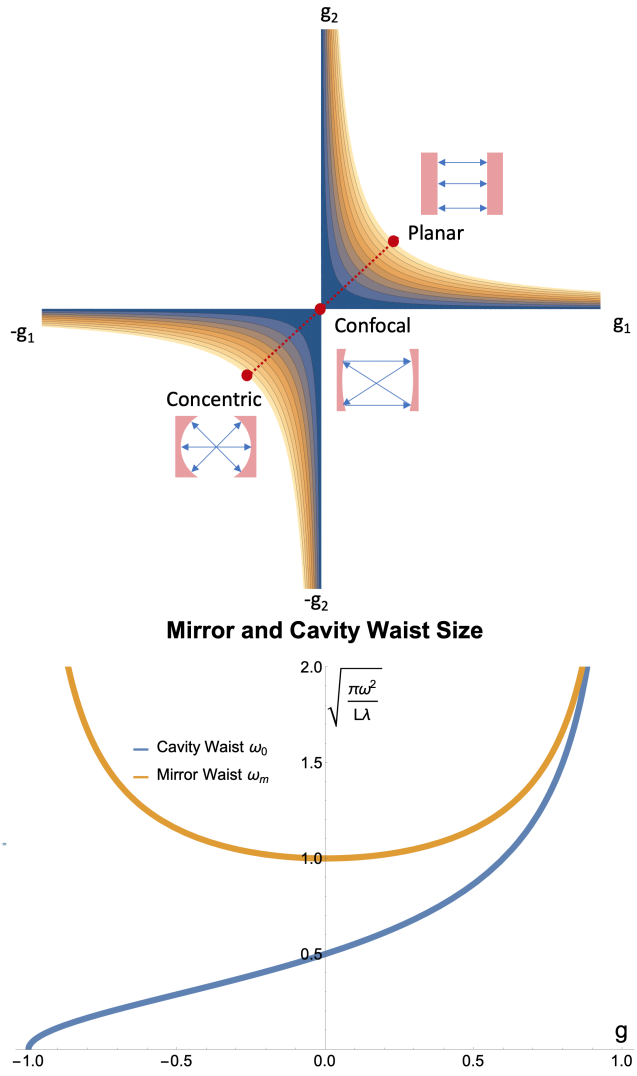

Figure 2.2: Plot of the stability parameter $0 \leq g_1 g_2 \leq 1$. Red dotted line represents symmetric cavities where planar, confocal and concentric have been represented by a ray-picture diagram. Bottom images shows the waist size in the cavity and at the mirrors for a symmetric cavity

2.5 Rydberg Atoms

The binding energy of an electron in an hydrogenic atom is:

$$\mathrm{E} \approx \frac{-\mathrm{Ry}}{(\mathrm{n} - \delta_{\mathrm{n,l,j}})} \tag{2.11}$$

Where Ry is the Rydberg constant, $\frac{m_e e^4}{8(\varepsilon_0 h)^2} \approx -13.6eV$, and $\delta_{n,l,j}$ is the quantum defect, an empirically determined quantity based on spectroscopic measurements. The wave-function for this electron, which is given by the Schrodinger equation, is:

$$[-\frac{1}{2\mu}\nabla^2 + V(r)]\ \psi(r,\theta,\phi) = \hat{U}\ \psi(r,\theta,\phi) \tag{2.12}$$

This is given in atomic units, where μ is the reduced mass, (r, θ, ϕ) are the coordinates of the electron is spherical coordinates, and V(r) is the electric potential from the core of the atom. The angular independence of the potential term allows us to separate the wave-function into a radial and angular components, $\psi(r,\theta,\phi) = R(r)Y_l^m(\theta,\phi)$, where the $Y_l^m(\theta,\phi)$ is a spherical harmonic. We can write the radial wave function in the following form

$$[\frac{-1}{2\mu}\left(\frac{d^2}{dr^2} + \frac{2d}{rdr}\right) + \frac{l(l+1)}{2\mu r^2} + V(r)]\ R(r) = \hat{U}\ R(r) \tag{2.13}$$

Rydberg Blockade

When two neutral atoms are near each in the presence of an oscillating electric field, the interaction strength between them can be described to leading order by the dipole-dipole interaction Hamiltonian

$$\hat{\mathrm{V}}_{\mathrm{dd}} = \frac{1}{4\pi\epsilon_0 r^3}\,(\hat{p}_{\mathrm{A}} \cdot \hat{p}_{\mathrm{B}} - 3(\hat{p}_{\mathrm{A}} \cdot \hat{n})(\hat{p}_{\mathrm{B}} \cdot \hat{n})) \tag{2.14}$$

This Hamiltonian describes the coupling between an atom A, with an oscillating dipole moment, radiating an electromagnetic field and interacting with the dipole moment of atom B an internuclear distance r away. $\hat{n}$ is the unit vector connecting

the atoms and p_i is the electric dipole operator. It is helpful to rewrite this in a spherical basis

$$\begin{aligned}\hat{V}_{dd} = \frac{1}{4\pi\epsilon_0 r^3}[&\left(p_{A+}p_{B-} + p_{B+}p_{A-} + p_{Az}p_{Bz}(1-3\cos^2\theta)\right) \\ &-\frac{3\sin^2\theta}{2}\left(p_{A+}p_{B+} + p_{A+}p_{B-} + p_{A-}p_{B+} + p_{A-}p_{B-}\right) \\ &-\frac{3\sin\theta\cos\theta}{\sqrt{2}}\left(p_{A+}p_{Bz} + p_{A-}p_{Bz} + p_{Az}p_{B+} + p_{Az}p_{B-}\right)]\end{aligned}$$

where (+,-,z) indicates the polarization of the oscillating dipole moment. This Hamiltonian mixes two atom pair states with other dipole-allowed pair states, that is states with l$\pm$1. In general the energy shift needs to be summed over all the infinite possible pair states, but this is not necessary in practice since typically a few pair states which are nearly degenerate with the original state dominate the interaction. These nearby states couple to the original state in a Förster process. If we consider the case where the two atoms are both in the same initial state, $|nl;nl\rangle$, then the energy difference, or Förster defect of the mixed state is[43]

$$\hbar\delta = E(n_A j_A l_A) + E(n_B j_B l_B) - 2E(nlj) \tag{2.15}$$

Consider 2 atoms in pair state with a Förster defect δ. Solving for the eigenvalues of the Hamiltonian gives

$$E(r) = \frac{\delta}{2} \pm \sqrt{\frac{\delta^2}{4} + \frac{C_3^2}{r^6}D} \tag{2.16}$$

where $D = \langle njl;njl|\,\hat{V}_{dd}^{\dagger}\hat{V}_{dd}\,|njl;njl\rangle$ and $C_3 = e^2\langle r\rangle_{nl}^{n_A l_A}\langle r\rangle_{nl}^{n_B l_B}$[63, 67, 65]. From Eq 2.16, you can see that for any given pair-state, with a defect δ there is a critical distance $R_c = \sqrt[6]{\frac{C_3^2}{\delta^2}}$ called the van der Waals radius, where the interaction shifts from the "Strong Dipole Regime"(where the interaction scales like $\sim \frac{1}{r^3}$) to the van der Waals regime (where the interaction scales like $\sim \frac{1}{r^6}$).

$$\text{if } r \gg R_c\text{: } E(r) = \frac{C_3\sqrt{D}}{r^3}$$
$$\text{if } r \ll R_c\text{: } E(r) = \frac{C_3^2 D}{\delta r^6} \sim \frac{C_6 D}{\delta r^6}$$

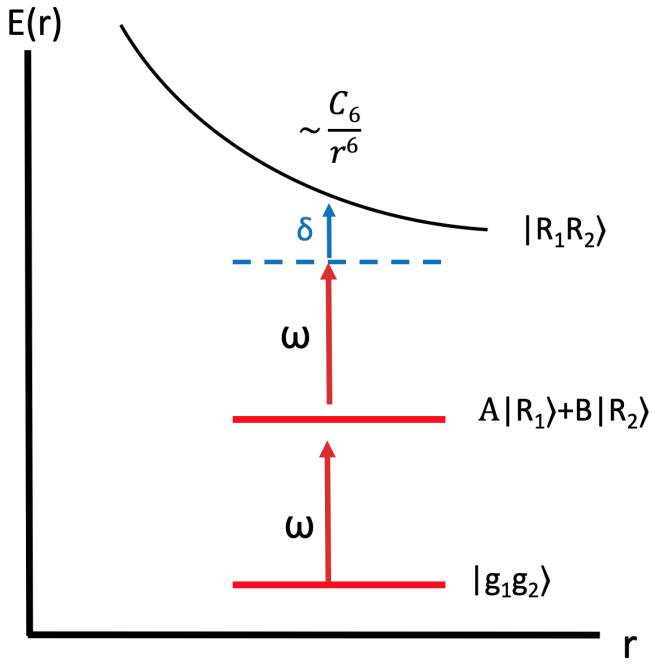

Figure 2.3: Rydberg Blockade for a pair of atoms. As the distance r between the atoms gets smaller, the interaction strength grows. The Energy shift δ from the un-shifted double-Rydberg state is shown in blue .

After summing over all possible pair-state contributions, if the energy shift is large enough, then the excitation to the double Rydberg state will be blocked. This is what is known as Rydberg Blockade.

Ensemble Qubits

Multiple atoms within a single blockade radius can all be addressed at the same time. The Rydberg blockade between the atoms prevents more than excitation, but that excitation is shared among all the atoms (Fig 2.4). The result is that the atoms form what is called a W-state.

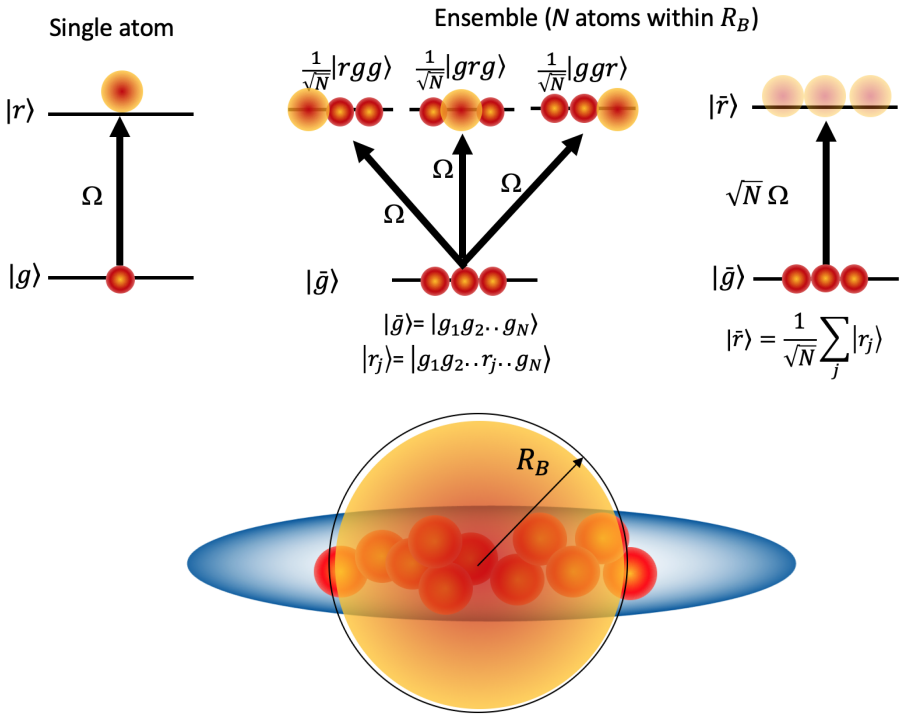

Figure 2.4: Upper image shows a diagram of how the W-state of the ensemble qubit is generated. Ensemble exists within the blockade radius RB of the atoms. This prevents more than one excitation among the atoms within the ensemble who share this single excitation. The collective interaction gives a $\sqrt{\mathrm{N}}$ enhancement to the Rabi frequency[18]

$$|\bar{r}\rangle = \frac{1}{\sqrt{\mathrm{N}}} \sum_i |g_1 g_2 ... r_i ... g_\mathrm{N}\rangle \tag{2.17}$$

for N atoms participating in the ensemble. This is a symmetric state sharing a single excitation among all the atoms [16]. One of the benefits of using an ensemble of atoms is that the interaction strength scales like the square root of the number of particles. For a single atom,

$$\Omega_\mathrm{r} = \langle r| H |g\rangle$$

however, for an ensemble of atoms,

$$\Omega_{\bar{\mathrm{r}}} = \langle \bar{r}| H |\bar{g}\rangle \, \Omega_{\bar{\mathrm{r}}} = \frac{1}{\sqrt{\mathrm{N}}} \left(\langle r_1 g_2 ... g_\mathrm{N}| H |g_1 g_2 ... g_\mathrm{N}\rangle + ... \langle g_1 g_2 ... r_\mathrm{N}| H |g_1 g_2 ... g_\mathrm{N}\rangle \right) \Omega_{\bar{\mathrm{r}}} = \sqrt{\mathrm{N}} \langle r| H |g\rangle$$

This shows that the ensemble has a Rabi frequency $\sqrt{\mathrm{N}}$ times larger than a single atom being equivalently addressed. Since Rydberg atoms have relatively short lifetimes, this Rydberg W-state can be mapped onto the ground state manifold to create a W-state between the two hyper-fine levels of the $5\mathrm{S}_{1/2}$ state. For more details about ensemble qubits and how they have been used in this experiment see [41, 17].

Chapter 3

Rb Ensemble Qubit Experiment

3.1 Scientific Background and Goals

Neutral atoms are a strong candidate for building qubits for use in quantum information processing. Specifically, using the hyper-fine levels of neutral atoms to define a qubit basis and performing operations using coherent light or atomic collisions. However, neutral atoms have specific challenges that must be overcome in order to be used as a platform for quantum computation. One of those challenges is the non-deterministic loading of atoms into an array. This problem has been solved for the most part with the use of atomic tweezers, which allows for the deterministic loading of a sub-region of the array [9, 10, 69, 52, 6]. In this way, Poissonian-loading of arrays is no longer really an issue as arbitrary patterns can be created from a partially filled array. Another hurdle for neutral atoms is that atoms can be lost from the trapping region, either due to heating or collisions with background atoms. A qubit lost in this way results in a loss of quantum information associated with the qubit, and can ultimately result in a failure of the quantum computation. A solution to both of these problems is to use an ensemble of atoms as a single qubit [19]. Ensembles consist of multiple indistinguishable particles which each participate in the creation of a single

qubit, shared amongst all of the constituents of the ensemble. Ensembles are easier to load in a deterministic fashion, are insensitive to atom number or loss, and have an enhanced interaction with addressing fields. While ensembles have to contend with inhomogeneous broadening and collisional decoherence channels, the previously stated benefits of ensembles make ensembles an interesting area of research and a potentially promising addition to the quantum information arsenal. In this section we are going to look at my contributions to the Rubidium ensemble qubit experiment and how those contributions helped to improve stability and quality of the results.

3.2 Temperature Controlled Box

One of the main challenges we faced in our lab is that of temperature control. Specifically the Rydberg addressing beams are very sensitive to temperature fluctuations as can be seen in Figure A.9. A parallel effort that we took to the Automatic Alignment System was to build a temperature controlled box around the main experiment to shield against temperature changes in the main lab space. The construction of the box also gave an opportunity to add passive RF shielding.

Passive Temperature Control

The box was designed such that the sides of it can be taken on and off. The only openings in the box when it is closed are small holes that allow optical fibers to pass through. All of the BNC, SMA, and XLR cables have isolated feedthroughs in the walls and top of the box. The walls of the box are constructed with corrugated plastic, a layer of copper sheet, and then two layers of foam. One of the layers is just normal foam, and the second layer is microwave absorbing foam (Laird Eccosorb QR-13AF), both of which provided some temperature protection.

Active Temperature Control

The active component of the temperature control consists of 4 computer fans attached to radiators which are cooled/heated with water. The water is part of a closed loop system consisting of a chiller and heater, along with a controller which measures the box temperature using a thermistor and feeds back to the current of the heater to maintain a constant temperature. Refer to Figure 3.1 for a detailed description of the system along with part numbers. The water in the chiller is over cooled to ∼18C, and is then subsequently heated to the correct temperature to maintain the temperature in the box.

Passive Radio Frequency Shielding

As mentioned above, the box is lined with copper to shield the inside from external sources of RF, including RF generators used to drive AOMs/EOMs and also Wi-Fi. Additionally, Microwave absorbing foam on the interior of the box is there to prevent standing waves from forming due to the microwaves that we intentionally introduce for global state rotations. Figure 3.2 shows the attenuation measured due to the walls of the box. Measurement was taken using two microwave horns, one as a source and one as a receiver, and comparing how much power the receiver can pick up when the wall of the box is not present vs when the wall of the box is between the horns. We were able to observe an attenuation of 30-40dB over the range of frequencies that we were most concerned about for interfering with our Rydberg states.

3.3 Alignment System

One of the main challenges associated with using tightly focused lasers to address atoms is maintaining environmental stability. Small fluctuations in temperature (and

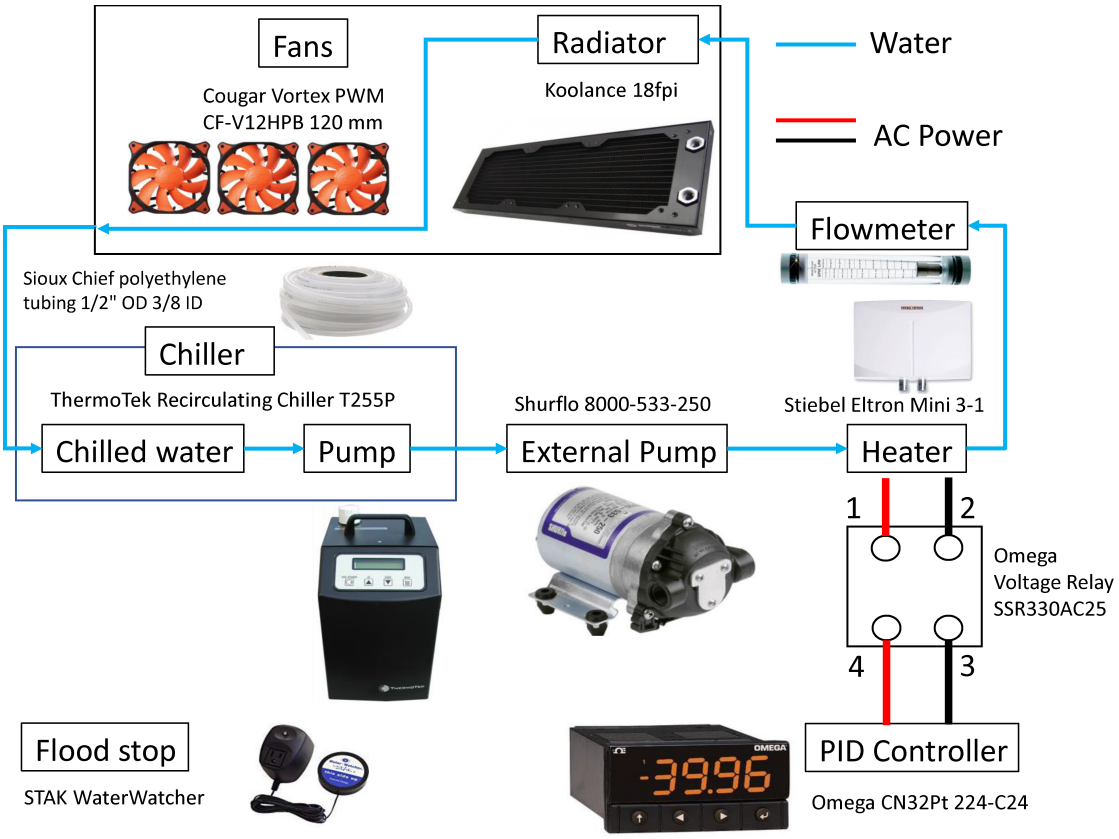

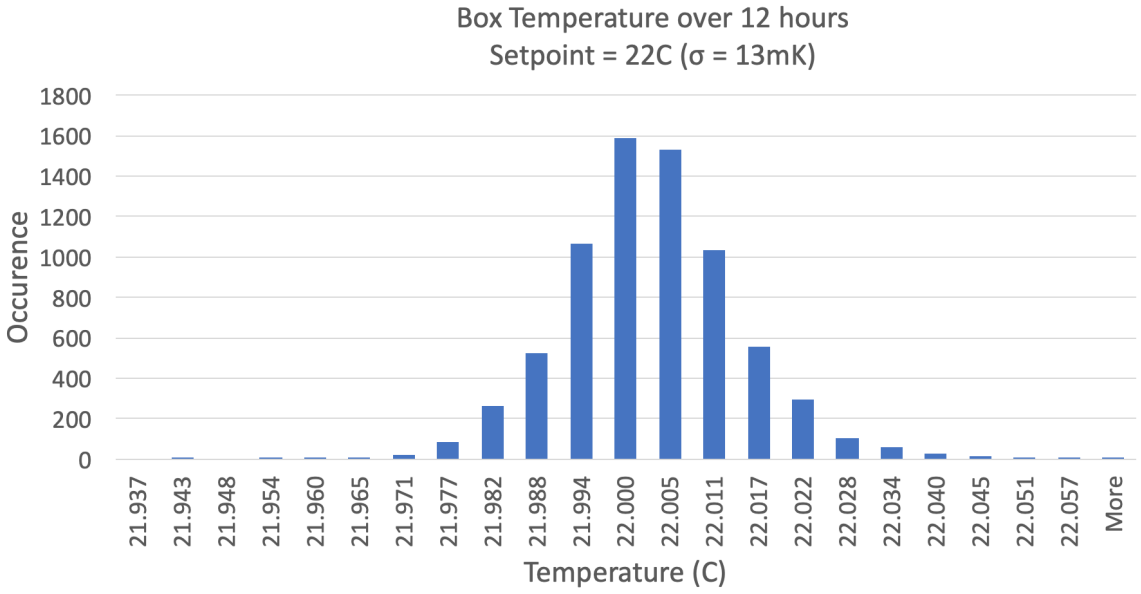

Figure 3.1: Temperature controlled box stability over 12-hour measurement period. Temperature remained stable to within 13mK.

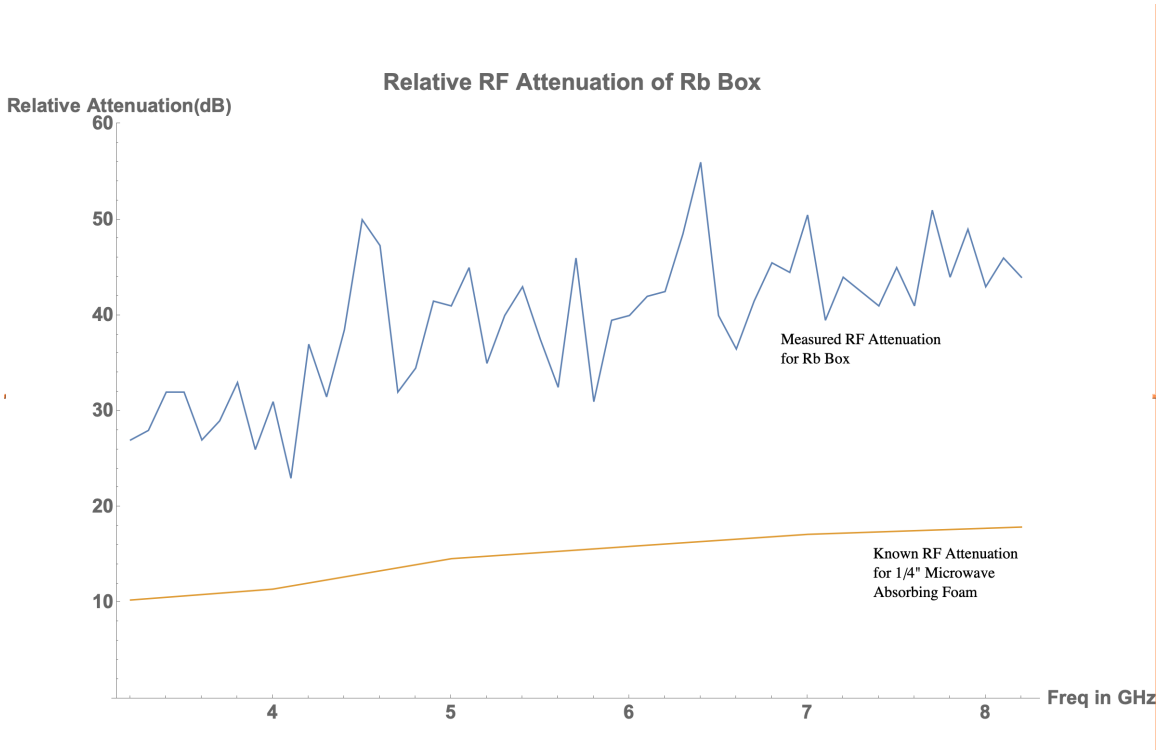

Figure 3.2: RF attenuation of the box. Blue curve is measured attenuation of a single wall. Orange curve is attenuation from 1/4" Laird Eccosorb QR-13AF[118]. Dashed line is a linear fit to the data.

to a lesser extent humidity) can have a significant effect on the beam alignments due to expansion/contraction of optical components. The main source of temperature fluctuations in our lab that we had to control was the room temperature, due to the fact that our lab lacks a dedicated HVAC. Additionally, when this alignment system was proposed and initially constructed there was no thermal shielding for our experimental apparatus. Beam adjustments were frequently required so that they properly overlapped with the atoms. The process required to do this is intensive, as both the 780nm and 480nm Rydberg beams need to be realigned. Additionally, there is the added complication that the optical components exhibit a hysteresis which means that even if the temperature is corrected after the fact, the alignment will not return to the state it was in before the temperature change. For these reasons, we sought to construct a system which was capable of imaging the addressing lasers using CCD cameras, and feeding back to Pico motors attached to lenses that would correct for any misalignment sensed by the camera.

3.3.1 Basic Configuration of Automatic Alignment System

The Automatic Alignment System(AAS) has three main components that work together to keep the addressing beams focused onto the atoms. The first component is a set of re-imaging optics which images the beams at the atom plane onto a CCD camera. The second component, which includes the CCD camera, images the beams, and processes the images to calculate the position error. And finally, the third system calculates the correction of the beam positions that need to take place, and then moves lenses in the 780nm addressing and 480nm addressing optical trains using Pico motors.

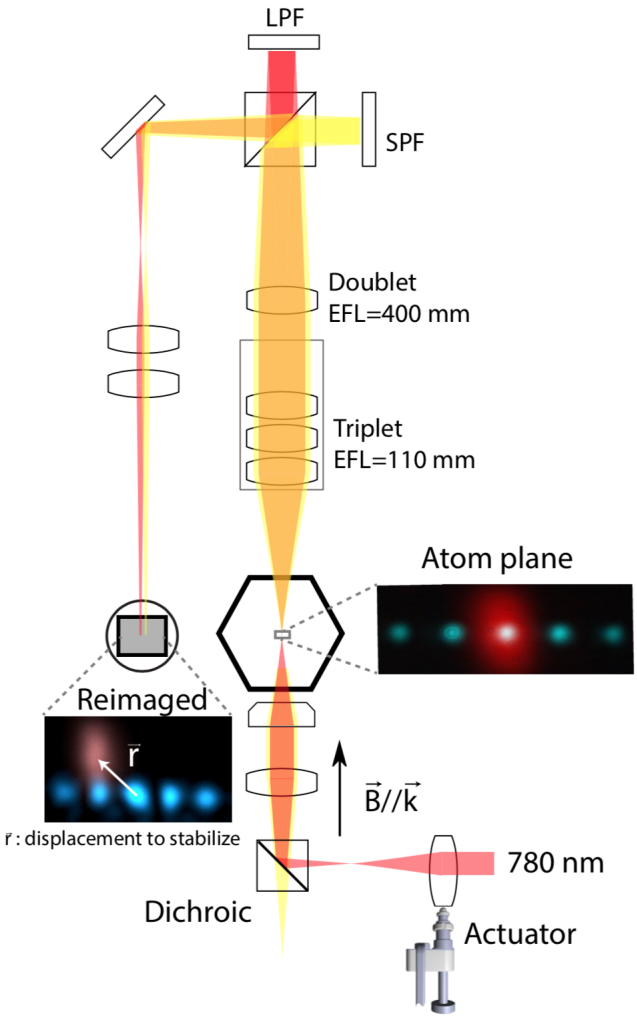

Figure 3.3: A schematic of the AAS optics. Atoms are trapped in a hexagonal vacuum cell in 5 ODT trap sites spaced linearly. The 780 nm addressing laser is combined with the ODT laser using a Dichroic beam splitter (DBS) cube. One lens in each of the 780 and 480 nm paths is placed on a computer controlled 2-axis transverse alignment stage, and is used to maintain the long-term relative alignment to the ODT laser. The EMCCD camera is used to image the atom trap population via fluorescence. The CCD camera is used to re-image both the ODT laser and 780 laser in separate 1-2 ms exposures. [41]

3.3.2 Automatic Alignment System Re-imaging optics

Figure 3.3 shows the optical train used for the AAS of the 780nm addressing beam. In order to image both the 780nm addressing beam and the 1064nm trapping laser on the same camera, given the achromaticity of the triplet and doublet for those wavelengths, a construction using a short pass and long pass filter was made so that the path lengths could be adjusted individually. Using a 50/50 beam splitter cube, the two exits paths of the cube would only reflect either the 1064nm or the 780nm beams. The correction needed after the triplet was 9mm, so by introducing a 4.5mm path length difference in the arms, the focal points of the two beams were able to be overlapped. An important note here is that only one of the axes of the 780nm addressing beam was able to be imaged, as a significant astigmatism is introduced onto that beam from the fast switching AOM used upstream for beam position control. This astigmatism, which corresponds to a waist position difference of 260μm for the x and y waists, is large enough at the imaging plane of the AAS that there is no practical way to focus both on the camera. The decision was made to image the x waist only, as not only is the x waist smaller, and thus more sensitive to alignment, but also the x-waist corresponds to the axis of our 5 traps, which makes keeping the x component of our beam aligned more important.

3.3.3 Automatic Alignment System-CCD Imaging and Image Processing

A CCD camera (BFLY-PGE-12A2M-CS), is used to image the 780nm laser, as well as the sites of the optical dipole trap. The 480nm portion of the Automatic alignment system is imaged onto the EMCCD camera that is used to collect the fluorescence from the atoms during the experiment. Images are taken during each experiment cycle, where they are processed to check if the images are of a sufficient quality to

fit, and also scaled such that the pixel values correspond to physics units in the atom plane, as well as offset so that the background amplitude corresponds to zero intensity. These images are then fit to X and Y centroids as initial guesses for later fitting. This is done mainly because the centroid calculation, which boils down to calculating the center of mass of the image, is very computationally easy. This initial guess saves time down the road when the Gaussian fits are done, because we can hand this centroid to our 5 site Gaussian fit. Since we know the site separations in the atom plane and the magnification on the camera (~ 18), we can give the fit accurate guesses of the locations which greatly reduces the resources required for the fits. Additionally, to offset possible beam distortion on the images, they are integrated in either the X or Y axes and then fit to 1D Gaussians. The positions of the beams are then passed to the software that calculates the error signal.

3.3.4 Automatic Alignment System Error Signal Calculation and Pico-Motor Correction

Beam locations on the image are used to calculate the displacement of the addressing beam from the FORT. Starting beam locations are determined by using a Ramsey measurement of the atoms. Once the starting location is determined, the displacement of the 780 addressing beam with respect to the trap sites is used to determine the error signal. Motion of the FORT, which should not be moving on timescales relevant for this analysis are assumed to be common mode. Displacement of the 780 beam on the camera is then translated to a corrective adjustment of the Pico motors. This correction is applied at the end of every experiment iteration.(For a more complete description of the Pico motor setup, refer to Minho's thesis)

3.3.5 Automatic Alignment System initialization of 780 Addressing beam using atom signal

In order to verify that the automatic alignment procedure is correctly aligning the laser to the atoms, it is necessary to use an atom based method for measuring the degree of alignment error. To do this we use the 780A Rydberg laser as an AC stark shifting beam that imposes alignment-dependent shifts onto atoms on different trap sites. The AC stark shifts $\langle \Delta_{AC} \rangle$ are measured by performing a Microwave Ramsey sequence. Maximal AC Stark shift will be observed when the beam is well aligned to the atoms.(Fig 3.4) If we control the total power in the 780 laser, then $\langle \Delta_{AC} \rangle$ can be used to determine the magnitude of the alignment error with respect to the atoms. The ground clock states used for this measurement only have a scalar AC stark shift, and so it can be calculated that for a beam with a power of a few μW and a detuning of $\sim -2GHz$ that the AC stark shift is of order 100s KHz. Our method for initializing the alignment system is to just scan across the FORT sites with the AC stark beam using a pulse that is $\sim \frac{\pi}{2}$ of a full population inversion when the beam is aligned to a single site. This gives clear peaks at specific Pico motor values that we can then use to initialize the error correction. By positioning the Pico motors such that the center frequency of the pointing AOM(160MHz) corresponds to the center FORT site, we can then calculate our corrections from there.

3.3.6 780 Addressing beam

To track the stability of the Automatic Alignment System, we position the AC stark shifting beam directly between the two sites, such that the frequency of the Ramsey fringes is the same for both sites. This has two main advantages. First, the beam position is between the sites, the rate of change of the signals is maximized for both sites being observed. This gives us a more sensitive measurement than if we were

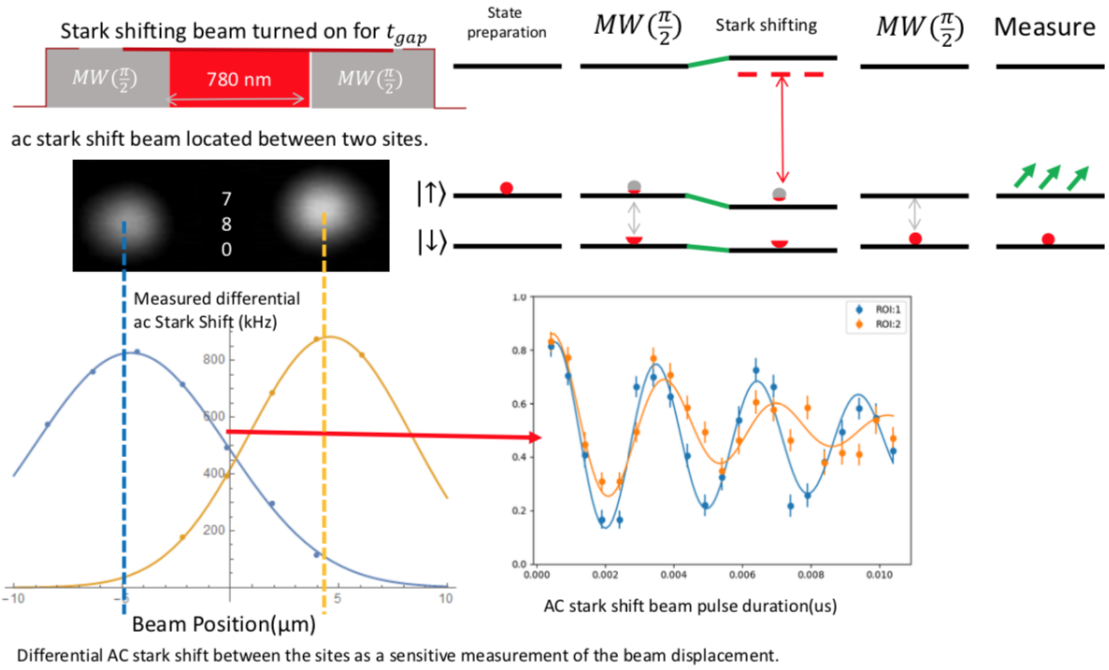

Figure 3.4: Overview of AAS process for detecting the misalignment of 780 Addressing Laser. The 780 Addressing beam used as an AC stark shift beam to do a Ramsey style measurement of the atoms. The beam is positioned between two of the dipole traps where the frequencies of the Ramsey fringes are most sensitive to its motion. The difference between the frequencies of the two signals is used to determine the relative motion of the beam. Motion in the vertical direction will affect both signals symmetrically while motion in the horizontal direction will affect the signals asymmetrically.

sitting directly on a single site observing the atom signal. Additionally, measuring the fringes in this position also gives us the most information about which direction the beam has shifted per unit distance of drift. Specifically, because we are between the two sites, we can distinguish a horizontal drift from a vertical drift by observing whether the change in frequency is common or differential mode. A common mode change indicates a vertical drift, a differential change indicates a horizontal drift. Also, if there is a horizontal drift, we will know which direction the drift was based on which of the sites has a decrease in the frequency and which one has an increase. By measuring this atom signal periodically, we can determine how much drift is occurring and whether or not that drift is reflected on the camera and if it is being corrected.

480 Addressing beam

As mentioned above, the 480nm addressing beam is not visible on the PointGrey CCD used for the 780 addressing beam alignment. Therefore, we imaged the 480nm beam onto the ANDOR EMCCD camera used to observe atom fluorescence. This has two major drawbacks when compared to the setup with the 780nm addressing beam. Firstly, there is not a good reference point to compare the position of the 480nm beam. It is possible to use the atom fluorescence signal as a reference, but the position of that signal is not consistent shot to shot. Depending on which of the sites is loaded, and where in the trap the atom is when the fluorescence is emitted effects the position of the signal on the camera. This can be averaged out over time, but it is not as straight forward as the other case. Additionally, the magnification of the 480 nm beam on the EMCCD camera is quite low, such that the signal is almost entirely within a 3x3 pixel square. We know that the 480 nm addressing beam has a waist at the atoms of $\sim 4\mu m$, while 3 pixels on the camera corresponds to about $\sim 12\mu m$ at the atom plane based on the magnification. This means that position

information from each shot is limited. However again, this can be overcome with statistics. Because the 480nm Rydberg beam is so far detuned from any transitions in Rb_{87}(the closest is the $5S_{\frac{1}{2}}$ to $6P_j$ at ∼420nm), the differential AC stark shift of the ground clock states is far too small to measure with a Ramsey fringe as we did for the 780nm Addressing beam. Even at 20mW, the absolute AC stark shift is only $\sim 600kHz$. This is too small to measure without atom fluorescence. Therefore, the method that we used for our 480nm Addressing beam alignment is to measure the amplitude and dephasing of a Ground-Rydberg Rabi Oscillation. If the 480nm beam drifts, then we will observe both a lower two photon Rabi frequency as the intensity of the light at the atom lowers ($\Omega_2 pho \approx \sqrt{I_{480} I_{780}}$. Additionally, as the beam drifts, the variation in light intensity seen by the atoms will also increase as they move around inside of the dipole traps, and so the observed dephasing of the signal will also increase.

3.3.7 Conclusion

Our main method of testing the AAS was to use the temperature controlled box to ramp the temperature of the experiment artificially, and then correct the atom position using the Pico motors. The results of such a run can be seen in figs A.9, A.10, A.11. Initially, the runs seemed to show that the AAS was performing substantially better than the open loop. However, over time, as we continued to cycle the temperature of the box, we found that the corrections to the beam placement on the camera, which had been consistent at first, became unpredictable and required higher order corrections beyond quadratic. Additionally, we found that the hysteresis associated with the temperature change was no longer happening to the extent that it had been originally. What we believe happened is that over the course of many thermal cycles, we may have effectively "annealed" our system into a state where there was very

little hysteresis to correct. Looking at figure A.12, you can see the measurements associated with one of these temperature cycles near the end of the period where we were testing the system. There is no statistical difference between the beam position measured at the atoms for the closed and open loop. The AAS helped to keep the atoms in focus when the temperature inside of the box had changed, but with the temperature controlled box this was unlikely to happen unless we experienced a temperature fluctuation that was beyond the capabilities of the box to correct. This did in fact happen a few times a year. However, without a clear improvement in the hysteresis over the passive stability, the usefulness of the AAS to us was in question.

3.4 Aligning to and locking the ULE cavity

One of the most challenging technical problems that we face in order to probe the physics of Rydberg atoms is the need to maintain a laser system that has a very narrow linewidth, of the order ∼100s Hz. The reason we need to do this is that the Rydberg transitions we want to address also have linewidths of order 100s Hz. Since the state lifetime is about $\approx 630\mu s$ for a Rydberg atom in the $84D_{\frac{5}{2}}$ state then our linewidth is $\lambda \approx 1500Hz$. To narrow our lasers to this level we lock our lasers to a high finesse ULE cavity. All three of our Rydberg lasers are locked to the same ULE cavity (refer to fig A.7 in the appendix for a full layout). When one of the three lasers is already locked to the cavity, aligning a second laser is relatively simple to start, and the pre-locked laser can be used as a reference showing the location and shape of the cavity mode. However, if you are trying to align a laser to the cavity from scratch that is more difficult. One way to align the laser to the cavity is to put a large photo-detector at the output of the cavity and to roughly set the mode of the laser to the cavity mode, and align the beam tp the input mirror of the cavity by eye. The input mode of the mirror can be calculated by finding the mode waist of the cavity

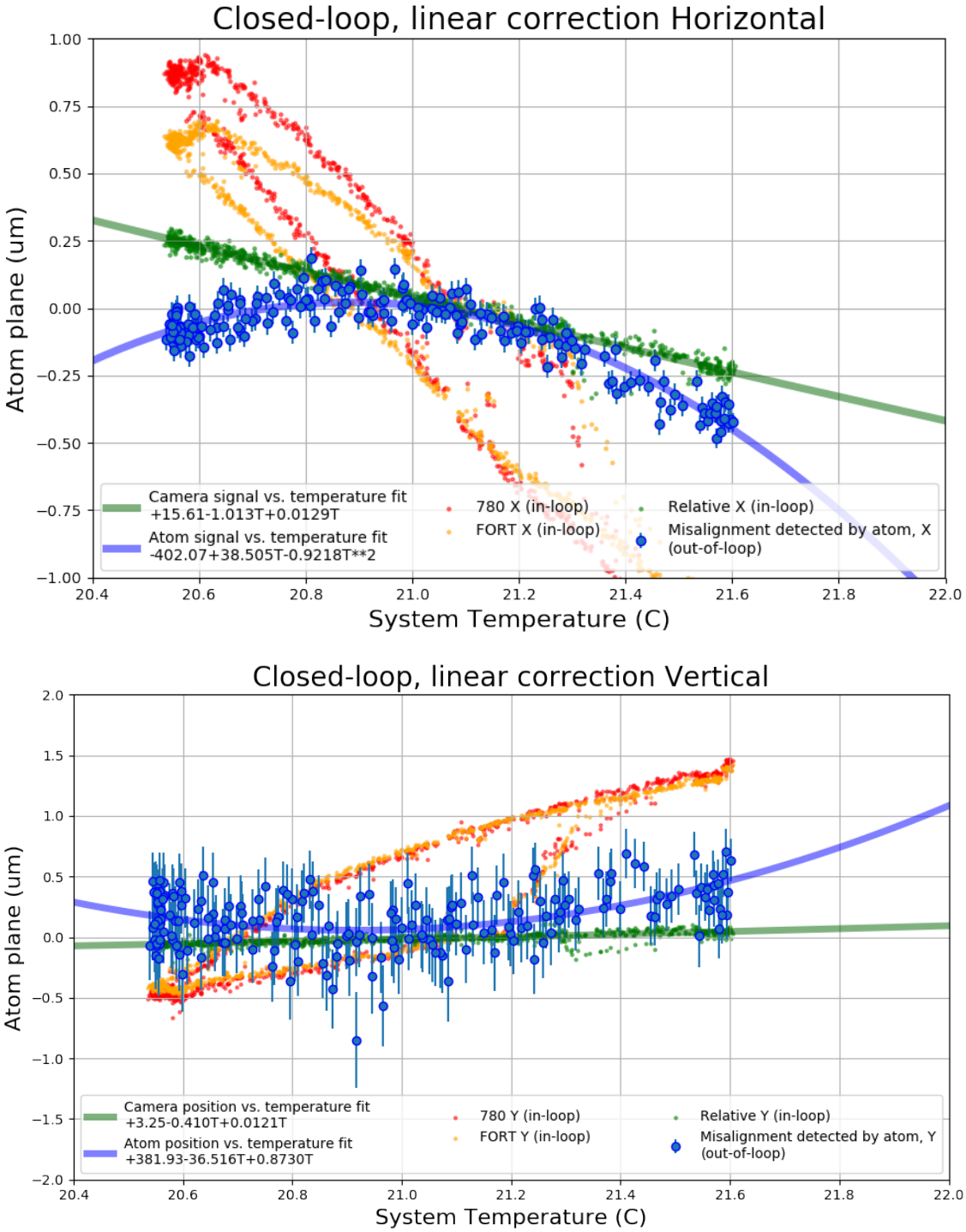

Figure 3.5: Closed-loop alignment versus temperature.showing a linear temperature correction to the beam position. Data taken on 2018-07-14

.

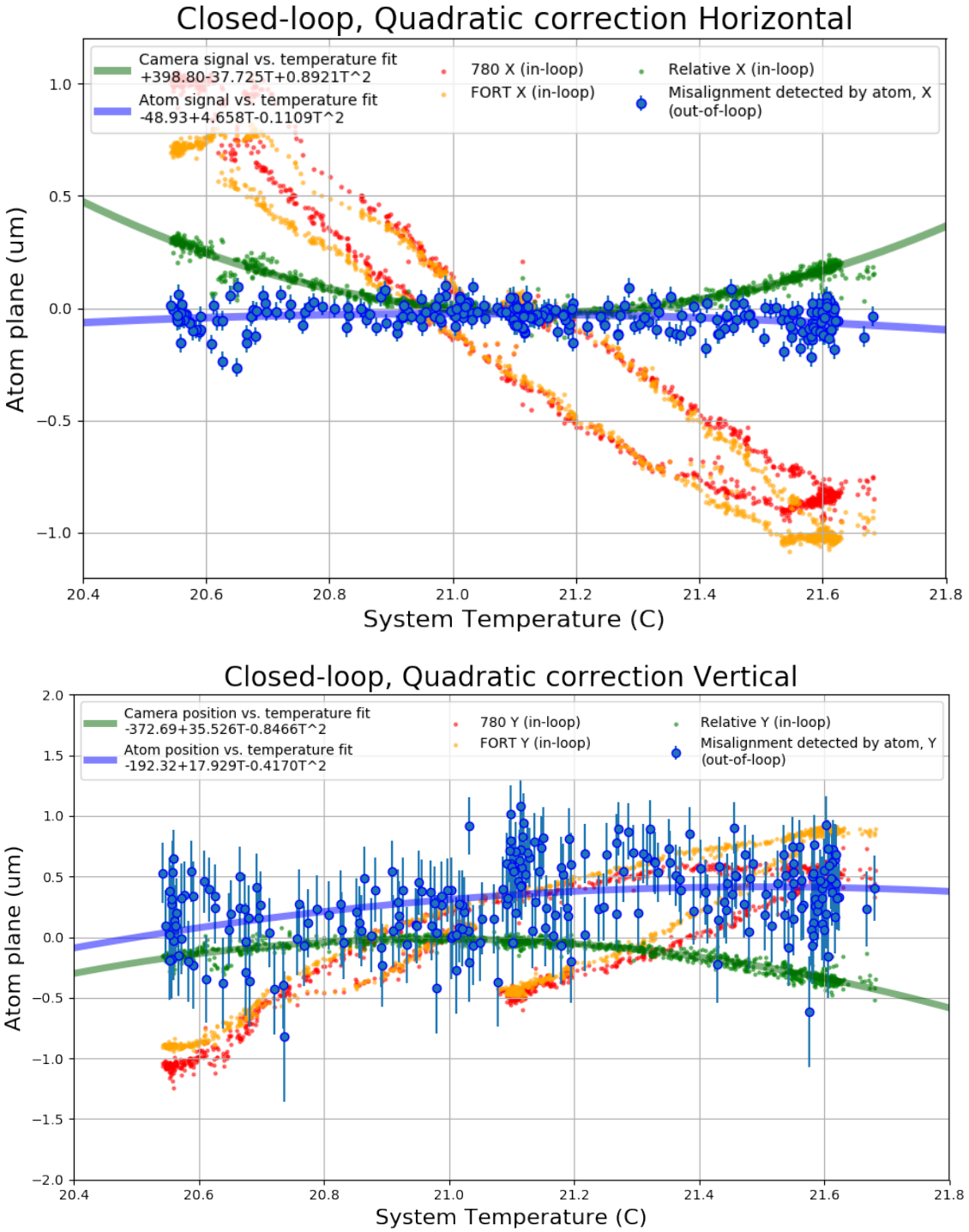

Figure 3.6: Closed-loop alignment versus temperature showing a Quadratic temperature correction to the beam position. Data taken on 2018-07-14

.

and focusing your beam into the cavity such that the waist size and location overlap the cavity mode (in general you must take the index of refraction of the mirrors and cavity medium into account). Then, with the laser sweeping (preferably more than an FSR of the cavity, in our case the $FSR = C/2L \approx 500MHz$) you walk the input beam around the transverse plane of the mirror and attempt to detect a signal on the detector. Unfortunately, this process is an exercise of patience. You would predict that care taken in setting the beam size and location would improve your odds but luck is also a factor here. However, once a signal of any size is detected, it can be used to rapidly improve the signal. Also I want to specifically point out that, as visible in the optics diagrams for both the ULE and the Servo-bump filtering cavities, that we have moved to a layout which has the main portion of the optics associated with the laser separated from the optics associated with the mode matching and locking of the cavities. The reason for this is that it allows for the adjustment, or replacement of optics ahead of the fiber without disrupting the cavity alignment. For the ULE cavity in particular this has been a huge improvement, as a week spent realigning to the cavity will quickly show. It does result in a small loss of laser power associated with the fiber coupling, but in most cases this loss does not interfere with the locking of the cavity. It is important that the face of the photo-detector is large enough that you can be absolutely certain that the outgoing light from the cavity will hit it, and initially it will be very weak and if the light is not hitting the detector directly you will not see a signal. Once there is a signal, the next step is to maximize the magnitude of the signal. This should be done without any feedback to the laser at this point. Changing the scanning range so that the frequency is only scanning right around one resonance will make the peak higher and easier to see. By adjusting the location, angle, and divergence while scanning the beam over this resonance, you can improve the SNR up to a point. It is typically very difficult to observe a very high, clean peak

with good SNR unless the laser is already quite narrow with low noise. Additionally, if the peak is high enough that you can start to establish feedback using PDH, then there is diminishing returns in continuing this step, and better gains can be made by switching over to using feedback. The schematic for our PDH lock and feedback system is show in Fig A.6. Once the signal through the cavity is strong enough that the fast feedback loop starts to drag out the signal, you can adjust the alignment to the cavity so that the dragged-out peak gets taller. In general, it is good practice to switch back and forth between optimizing the peak height with and without the fast feedback on because ideally you would perfect the alignment to the cavity with no feedback. However, in practice this is not always feasible and using the feedback to help guide you can expedite the process substantially.

3.4.1 Rydberg laser servo bump filter cavities

As a method of reducing laser noise, we constructed servo-bump filtering cavities. The cavities are constructed with 0.5in cavity mirrors within an INVAR housing. The mirror spacing is widely adjustable, but we constructed the cavities to be ∼10cm in a non-confocal arrangement. Active control of the cavity length is done with a stacked ring piezo.(Constructed cavity is shown in Fig 3.7. The optical train for the servo bump filtering cavities is shown in FigA.8. PDH locking electronics are shown in Fig A.6. The cavities have a typical linewidth of $\sim$ 300 kHz, corresponding to a finesse of $\sim$ 5000 (FSR $\sim$ 1.5 GHz). Using these filter cavities, we were able to clip off the ∼1MHz servo bumps put onto the Rydberg lasers by the ULE lock. Fig 3.8 shows the efficacy of the filter at reducing the high-frequency noise. Amplitude noise on the transmission of the filter cavity was reduced by "Fast-noise eating" using a Red-Pitaya STEM 125-14 V1.0 FPGA board and PyRPL software connected to an AOM. The AOM is used to modulate the power of the light transmitted through the

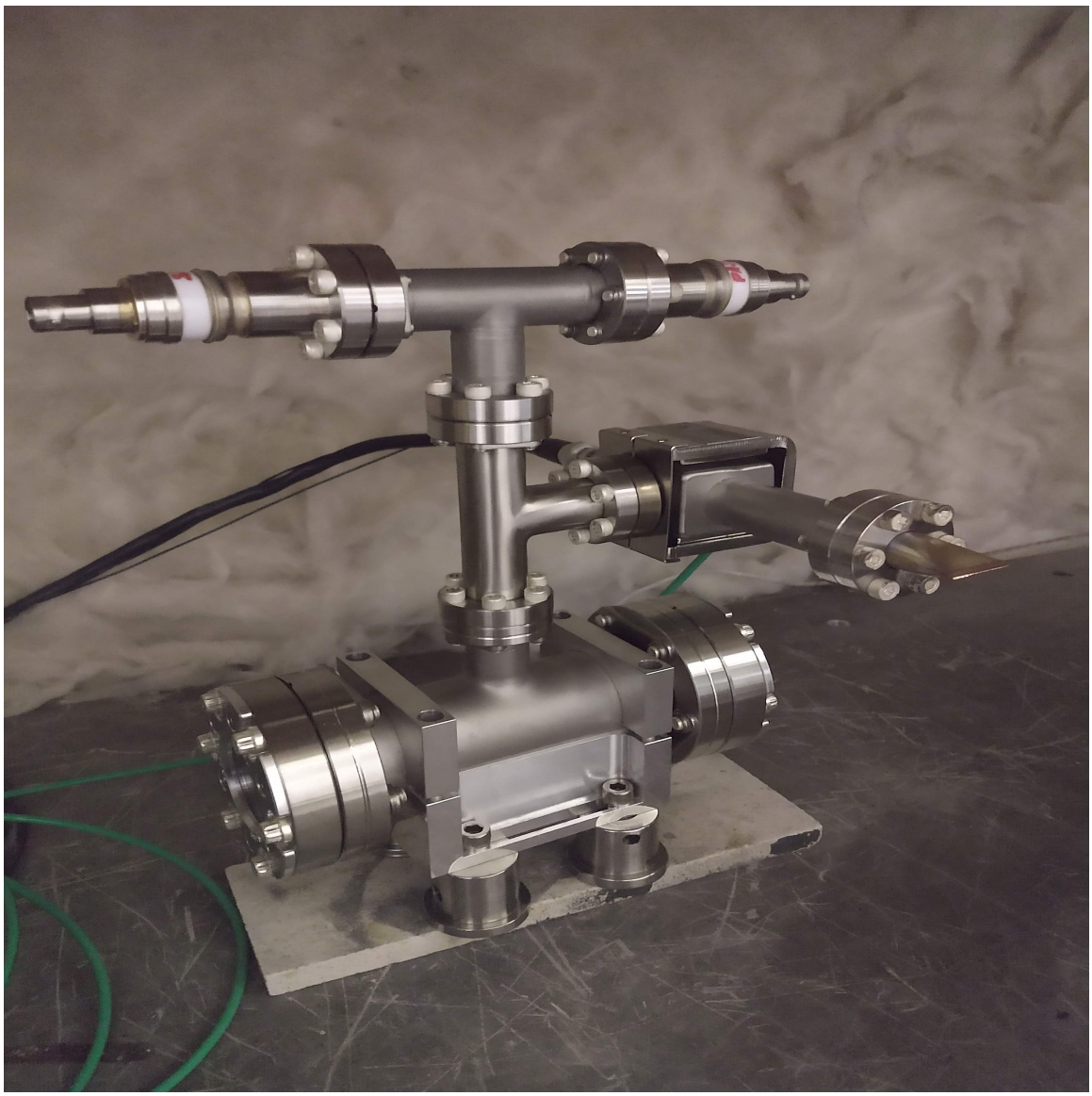

Figure 3.7: Constructed Filter Cavity in a vacuum can.

filter cavity. Fig 3.9 shows the reduction in amplitude noise observed. While we have finished construction, and installed the 780-filter cavity, the 960 filter cavity is also constructed but awaiting installation.

3.4.2 Rydberg Reference Cavity lock monitors

Rydberg Laser lock monitors are critical for smooth operation of the experiment. We designed multiple ways of monitoring the status of the Rydberg laser locks. To check if the Rydberg lasers are locked to the ULE cavity, we have cameras positioned on the outputs of the ULE cavity which can see the mode exiting the cavity. This output is shown in Fig 3.10. RaspPi computers are used to monitor the cavity output flag when the transmission drops below a certain threshold. We had tried with limited success to also monitor the mode shape in this way, to check that the laser is locked to the fundamental mode of the cavity. This is certainly possible but we checked the frequency in a different, more direct way. By beating the 780nm rydberg laser with light locked to the cooling transition, we were able to observe a beat-note at 2.94GHz. This beat-note is then down-mixed to 50MHz (this was just convenient, could be anything) and passed the signal to a frequency counter (TTi TF930) which we can use to monitor the frequency of the beat-note. Since the Cooling light is locked to a spectroscopic signal, we can use this as a reliable frequency reference for the cavity. We also created a beat-note between the repumper and the $5S_{1/2}\,|F=1\rangle \rightarrow 84D_{5/2}$ Rydberg laser, although it required much more down mixing. These two monitors allow us to check that the 780 addressing lasers are locked to the ULE cavity and have the correct frequency. This method is not possible with the 960. We had tried to use the Frequency Comb as a monitor with little success. Ultimately, we used the transmission monitor of the 480nm SHG cavity as the frequency monitor for the 960nm Rydberg laser because we don't have a reference to beat it with. The frequency

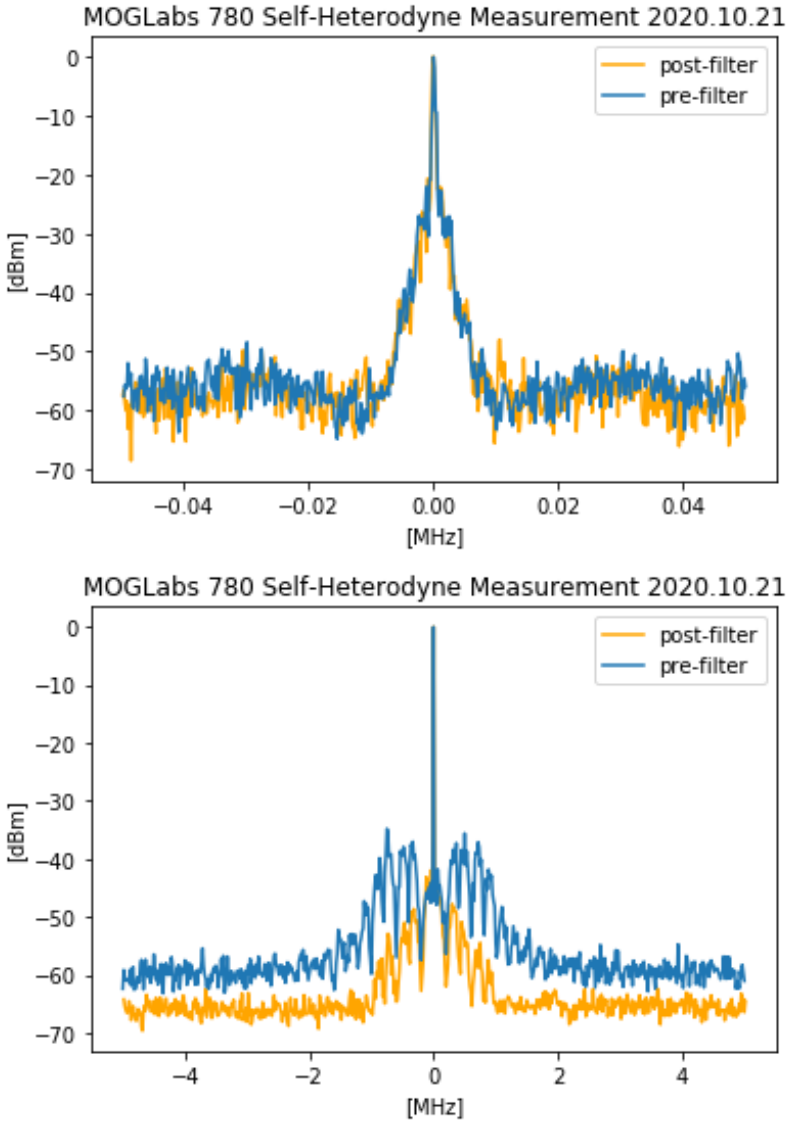

Figure 3.8: Self-Heterodyne Measurements showing the removal of the servo-bumps caused by the ULE lock from the 780nm Moglabs laser. Data Collected by Preston Huft.

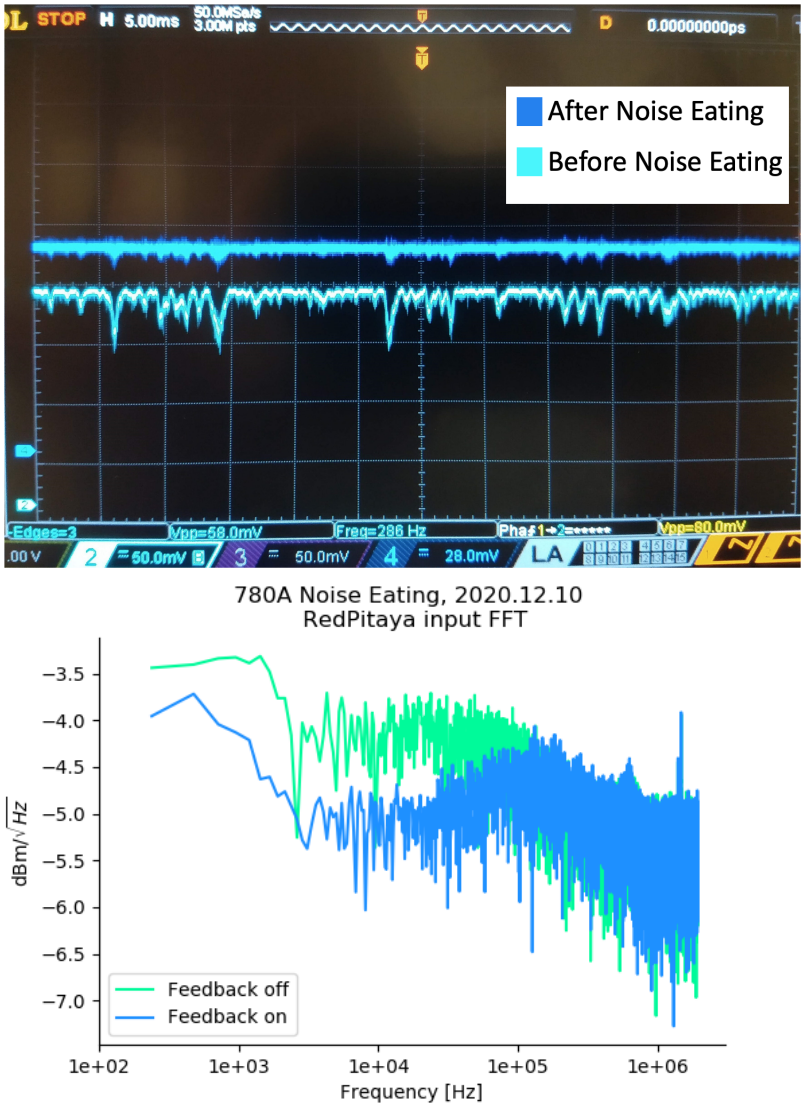

Figure 3.9: Oscilloscope trace showing the reduction in amplitude noise on the output of the servo-bump filtering cavity due to fast noise eating. Lower figure shows the reduction in noise. Data Collected by Preston Huft.

Figure 3.10: Pictures showing the ULE transmission monitors. Top image shows the transmission 780nm light locked to the TEM00 mode of the ULE cavity, Bottom image shows the transmission 960nm light locked to the TEM00 mode of the ULE cavity.

sensitivity of the SHG cavity is great enough however that is if the ULE lock hops modes, the power output of the SHG cavity will drop substantially (if it also stays locked). A word of caution with the beat-note monitor: when making a beat-note in this way, even with the down-mixing, there is going to be another beat-note on the "opposite" side of where you want to be. That is, if our raw beat-note is 2.94GHz, that means our 780A laser could be 2.94GHz below the cooling transition (correct), or 2.94GHz above the cooling transition (incorrect). In general, these will show up as the same on the frequency monitor even when down-mixed. This is a limitation of this design, and we ultimately had to use the visible shape of the beat-note on the spectrum analyzer, or measure the frequency directly to determine if we were on the "right side" of the beat-note. A less reliable method is to change the frequency of the laser and see how the frequency of the beat-note changes. The direction of movement should be opposite for opposite sides of the beat-note, but this is not a particularly reliable method.

3.4.3 Vacuum chamber/Structure

The part of the experiment under vacuum is comprised of two Pyrex cells connected by a differential pumping tube. The 2D MOT chamber, initially constructed as the upper cell, has a square cross section. This cell has an atom pressure of $\sim 5 * 10^{-8}$ torr. The 3D mot cell, initially constructed as the bottom cell, has a hexagonal cross section. The pressure in this cell is about 1000 time less[41]. The differential pumping tube is what allows us to maintain this large difference in pressure between the cells, while also allowing the atoms from the upper cell to be corralled down into the lower chamber. At the low pressures inside of the cells, the physics of the gas molecules can be treated ballistically. That is to say that they behave like hard spheres which move independently of each other. If we consider the atoms in the cell when the MOT is not

Figure 3.11: Image showing the two vacuum cells, 2D-MOT chamber on top with the 3D-MOT and science region below. The two halves are separated by a differential pumping tube with the dispensers in the upper region. Image taken from Matthew Ebert's Thesis [17]

engaged, their temperature would be room temperature, about 25C. Additionally we may assume at this temperature that the scale over which the atoms in the chamber interact with each other is very small, about of the same order as their diameter. Then the mean free path, l, of the atoms in the upper chamber follows this formula:

$$l = \frac{k_b T}{\sqrt{2}\pi d^2 p}$$

Where k_b is the Boltzmann Constant, T is the temperature, d is the "diameter" of the gas molecule/atom, and p is the pressure. For Rb87 at room temperature and 5×10^8 torr, this gives a mean free path of about $\sim$ 630 meters. This is much larger than the size of the cell, and so it can be assumed that each atom in the cell bounces off the walls of the cell many times before colliding with another atom. It is this behavior, paired with the fact that the atoms have a propensity to stick to the metal in the differential pumping tube that prevents them from traveling into the lower chamber. Since they do not collide, it is very unlikely for the atoms to end up on a path heading directly down into the lower chamber without colliding with the tube. As will be discussed later, in the case where the 2D MOT is running, a large flux of atoms are directed through the differential pumping tube into the 3D MOT in the chamber below.

3.4.4 Trapping

Trapping of the atoms is done with a dipole trap at 1064nm. A single 1064nm source beam is split into 5 sites using a fixed diffractive element. Characterization of the sites give x,y waists of $\sim 3\mu m$ at the atom plane. Typical power used for the FORT is 400mW, which gives a depth for the center site of $\sim 1.2mK$. Since the sites

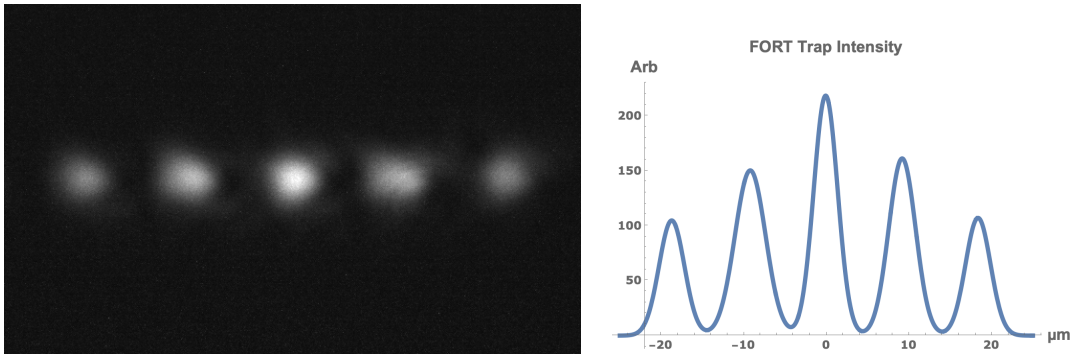

Figure 3.12: Image of 5 FORT sites taken in the atom plane. A slight tilt of a few degrees has been corrected in the image, but is visible on the CCD for the ASS and in the atom signal on the Andor.

have different depths, atoms in different sites have different life times, and experience different AC stark shifts. This necessitates that during the cooling, readout, and addressing phases of our experiment that the trapping light is turned off. Full Diagram is given in Fig A.5.

3.4.5 MOT

Our experiment uses a double MOT, where one feeds the other. We accomplish this by having two chambers separated by a differential pumping tube. In the upper chamber (Fig 3.11) the enriched Rb87 dispensers feed a 2D-MOT oriented such that it cools the atoms in the horizontal plane. Another weak "push" beam from above sends atoms through the differential pumping tube separating the two chambers, in the lower chamber, a 3D-MOT is located in the path of the stream of atoms from the upper chamber. This lower chamber is our science chamber and where we load our dipole traps. Because of this setup loading of the 3D-MOT requires that the 2D-MOT is feeding it, as the atom density in the lower chamber is not sufficient to load the dipole traps from the background alone. Atoms are loaded into the chamber via a

dispenser, and additionally via UV light exposure using a Thorlabs M405L2-C2-UV (405 nm) Collimated LED which shines on the glass walls of the upper chamber. In this way, we can increase the atom pressure in the upper chamber to increase our loading rate.

3.5 Polarization Gradient Cooling

As mentioned previously, when we load our dipole traps from the MOT, they have an atom temperature of $\sim 100\mu K$. This temperature however is still hotter than we would like, as it significantly effects our retention during our readout, and it also effects our dephasing during Ground-Rydberg Rabi oscillations. During both the readout and our Rydberg pulses, the dipole traps are turned off, and higher temperature atoms are more likely to move outside of the region where they will be recaptured by the trap when it comes back on. Additionally, when the atoms are hotter they occupy a larger volume inside of the trap. This causes dephasing during atom addressing as the atoms will sample a larger range of laser powers. The cooling method that we use, called Polarization Gradient Cooling (PGC), is a method whereby the atoms are exposed to an electric field polarization that varies with position. In the case of $\sigma+/\sigma-$ PGC, the polarization is linear everywhere within the field but the axis along which it is polarized varies with position. For an atom at rest at some point in this field, the atoms will be preferentially pumped into the M=0 state due to the Clebsch-Gordon coefficients favoring that state through decay. As the atom moves through the field, the quantization axis turns. It can be shown[46] that as the atom moves towards the $\sigma+$ light, the atoms bunch into the m=-1 sublevel. This is due to the fact that there is a lag between the atom moving to a location with a different quantization axis, and the M-levels redistributing. This causes an increase in scattering from the $\sigma+$ light. Similarly, as the atom moves towards the $\sigma-$ light,

the atoms bunch into the m=+1 sublevel. this causes an increase in scattering from the $\sigma-$ light. The end result is a velocity dependent scattering which dampens the motion of the atoms, preferentially scattering them towards a lower velocity state. Just like our MOT, the PGC does not work on the atoms while they are in the dipole trap. The reason for this is that the $5P_{\frac{3}{2}}$ state has a substantial tensor AC stark shift due to the nearby $6S_{\frac{1}{2}}$. This means that while the atom is in the trap, the different m-levels in the $5P_{\frac{3}{2}}$ F=3 state have different energy levels. Additional, since the traps have different depths as well, the different sites experience different AC stark shift. The energy difference between the m-levels for a π-polarized dipole trap where there is no vector shift goes like $-m_f^2$, with a magnitude of order $\sim \Gamma$, the linewidth of the cooling transition. This means in practice that the atoms cannot be effectively cooled or imaged inside of the 1064nm dipole trap. this necessitate the use of a chopping procedure, whereby we chop the FORT on and off with a frequency of $\sim 1MHz$. This frequency is chosen such that we are not exciting any of the resonance modes of the atom inside of the trap, which would quickly cause loss of the atom. When the FORT is turned off, the cooling lasers come onto resonance with the atoms such that cooling is possible. When the FORT turns back on, it confines the atom to stay in the same location, as the entire cooling procedure can take several ms, during which time the atom can move far beyond the trapping region if it is not confined. Using this method, we have been able to cool our atoms down to a minimum of $\sim 40\mu K$. The fact that this number is still quite high when compared to what should be achievable with PGC for Rb87 is likely due to imperfect zeroing of the B-field, imperect beam alignment, or the chopping of the FORT and cooling light.

Procedure to find zero of B-field

As mentioned in sec 2.2, to rotate between our two qubit states we use π-polarized MWs to drive the $|F = 1, m_f = 0\rangle \rightarrow |F = 2, m_f = 0\rangle$ transition. However, due to reflections within our system, there are other polarization components that can drive transitions if the detuning of the MW is changed. To find the zero-point of our B-field we used the following procedure: Since our Z-shim coil (measured $9.29\frac{G}{A}$) defines our quantization axis, then ideally when we induce a Zeeman-shift between our m-levels, the transverse field would be zero. However, in general this isn't true. But we can assume that for a high bias field, of about 3-4G, that the stray transverse fields should only manifest as a small change in the magnitude of the bias field, if our X and Y shim settings are correct and they are canceling out the background magnetic fields. By varying the X and Y shim coil currents we were able to find the current settings that minimized the frequency shift between the $|F = 2, m_f = 0\rangle \rightarrow |F = 1, m_f = 0\rangle$ and $|F = 2, m_f = 0\rangle \rightarrow |F = 1, m_f = -1\rangle$ transitions. Once we found the correct settings for the transverse field shims. We were able to measure the shift due to the bias field shim directly. This was done by measuring the MW frequency at a few points well above the zero-field point and then extrapolating the fit to find where the z-shim current needed to be to have zero B-field at the atoms. This was confirmed by measuring the quadratic shift of the $|F = 1, m_f = 0\rangle \rightarrow |F = 2, m_f = 0\rangle$ transition, which agreed to within 5mG. This is shown in fig 3.13. After zeroing the B-field, we were very quickly able to observe sub-Doppler cooling in our system, getting our atom temperature down to a minimum of $\approx 40\mu$K. Another thing that we tried to do to maximize the effect of our cooling is to leave the cooling light on as we chopped the trap around it. This would effectively have the atoms come in and out of resonance with the cooling light as the trapping light flashes on and off around them. The idea being that by leaving the cooling light on all the time, we could maximize the amount

of time that cooling light was meaningfully interacting with the atoms. Additionally, since the effective energy of the cooling transition is raised when the trap light is on the red-detuned cooling light will not pass through resonance with the transition as the FORT comes on and off and so it should not have a significant effect on the scattering or heating of the atoms. This actually turned out to not have a noticeable effect on our atom temperature after PGC, but it did reduce the complexity of our experimental sequence and it significantly increased the fluorescence measured during our readout, which doubled as our first stage of cooling (molasses). So, this turned out to be an improvement over switching both the trapping laser and the cooling lasers on and off.

3.6 Optical Pumping and Heating Simulation

3.6.1 Intro

One of the ways in which we unintentionally heat our atoms is through optical pumping. Optical pumping is a process whereby atoms addressed with light in such a way that they will absorb and emit photons to eventually end up in some desired state. In the case of our experiment we pump ^{87}Rb into the $|F = 2, m_f = 0\rangle$ state. This is done using the D1 line of ^{87}Rb using the following scheme. The atoms are pumped towards the "Dark state": a hyper-fine level which does not interact with the pumping light. As the atom absorbs and emits photons, it will change its hyper-fine projection until it ends up in the dark state where it will no longer absorb light. In the case depicted in Fig. 3.16, this is the $|F = 2, m_f = 0\rangle$ clock state. You can do a very rough estimation of the heating involved by just analyzing the branching ratios of the different levels. Consider the case of pumping to the clock state with linearly polarized pumping light. If the atom in question starts in the dark state, then clearly there will be no

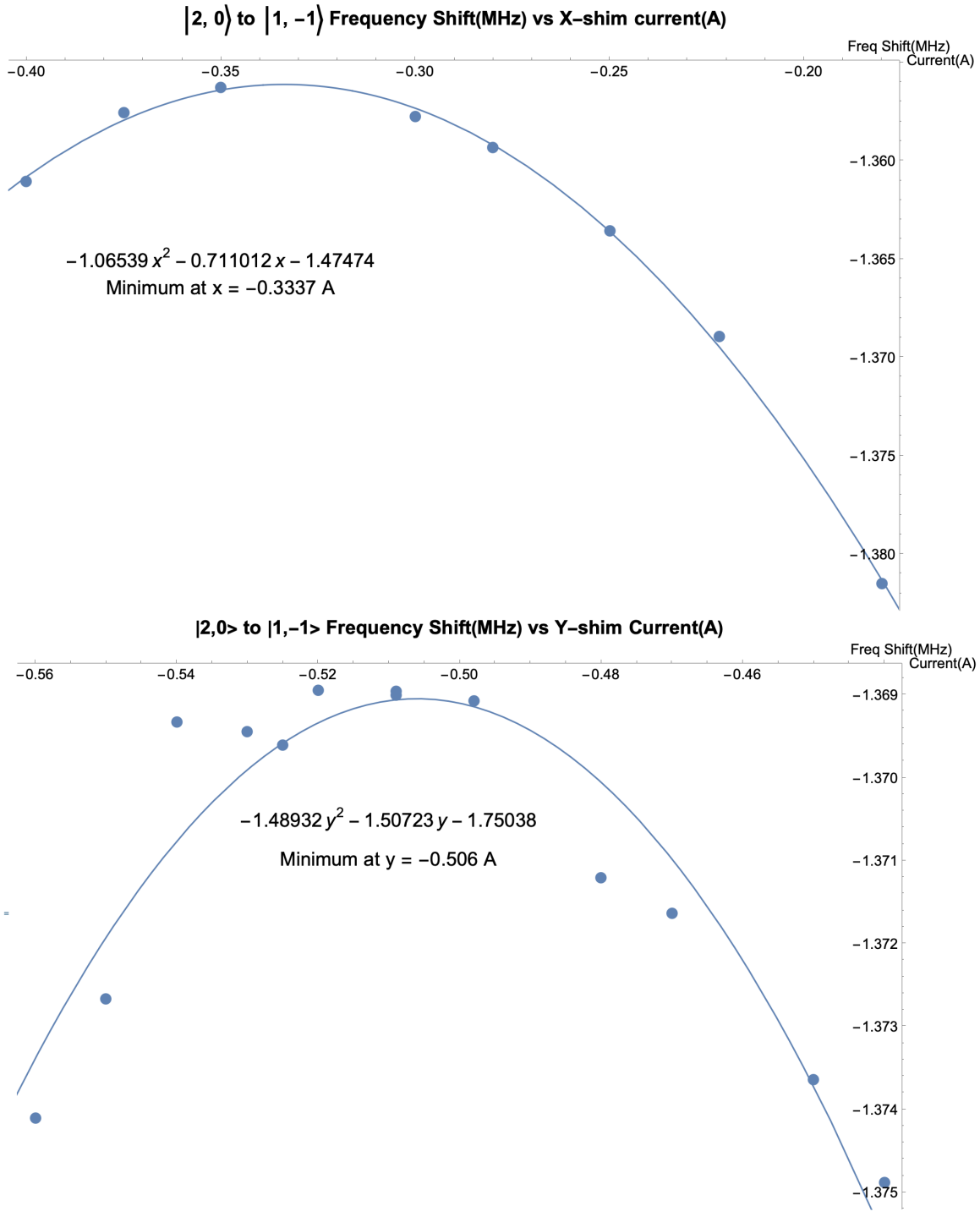

Figure 3.13: Data showing the measurement of the Zero B-field location within the hexcell. Plots show the frequency shift associated with the $|F = 2, m_f = 0\rangle \rightarrow |F = 1, m_f = -1\rangle$ transition as compared to the value of the measured $|F = 2, m_f = 0\rangle \rightarrow |F = 1, m_f = 0\rangle$transition

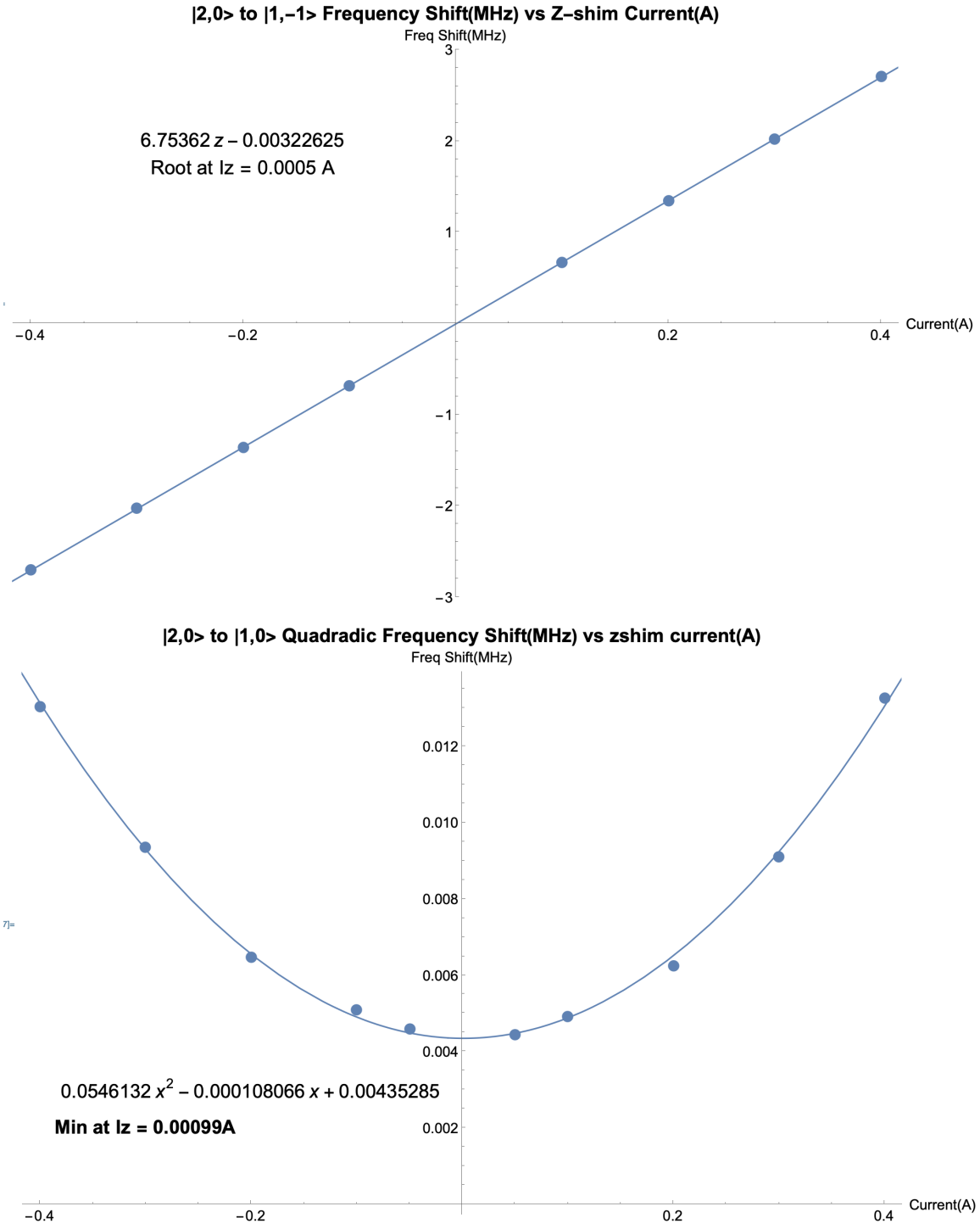

Figure 3.14: Data showing the measurement of the Zero B-field location within the hexcell. Plots show the frequency shift associated with the $|F = 2, m_f = 0\rangle \rightarrow |F = 1, m_f = -1\rangle$ transition as compared to the value of the measured $|F = 2, m_f = 0\rangle \rightarrow |F = 1, m_f = 0\rangle$ transition

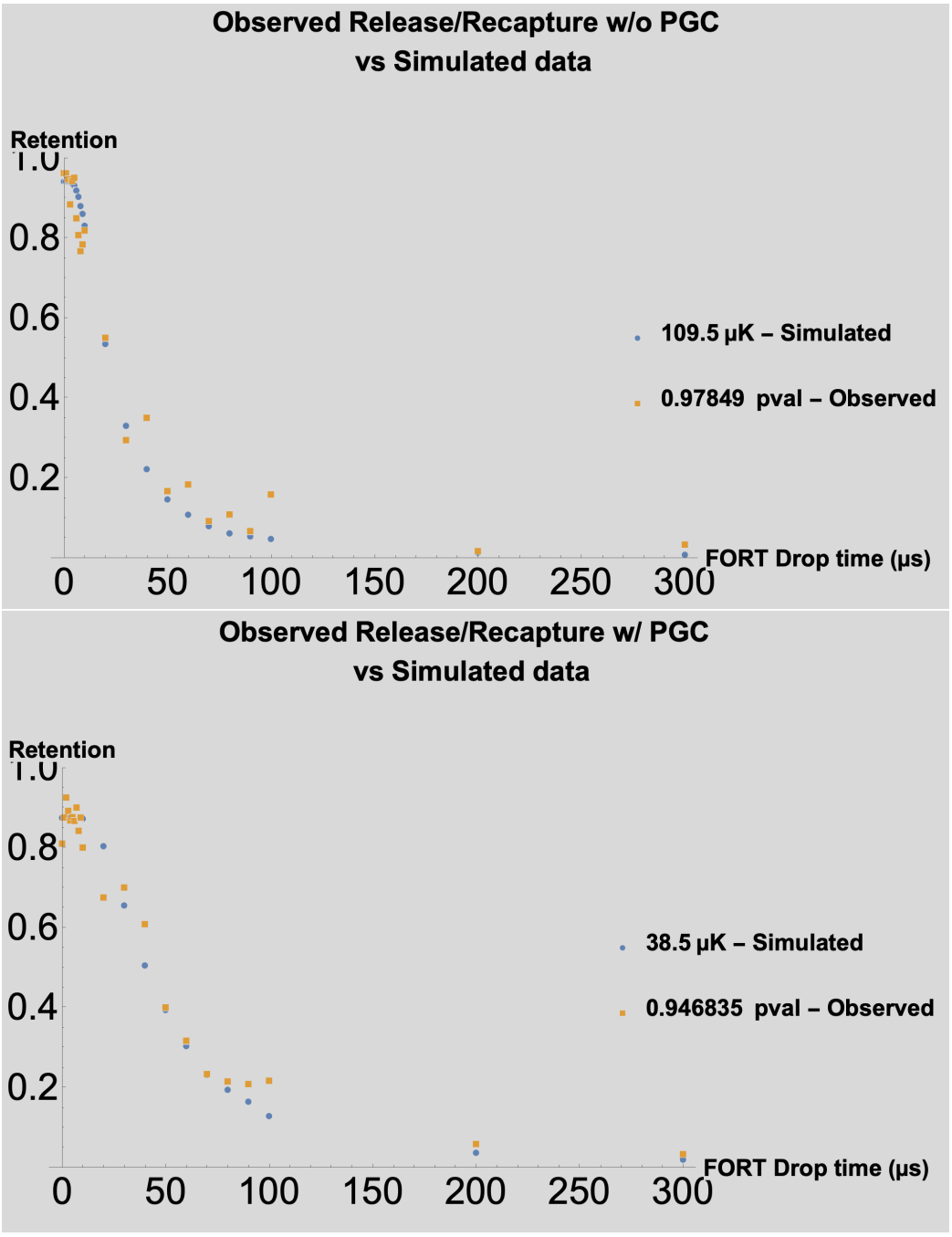

Figure 3.15: Plots showing efficacy of PGC after zeroing the B-field and tuning the parameters. Data is shown compared to a simulation of Release/Recapture experiment.

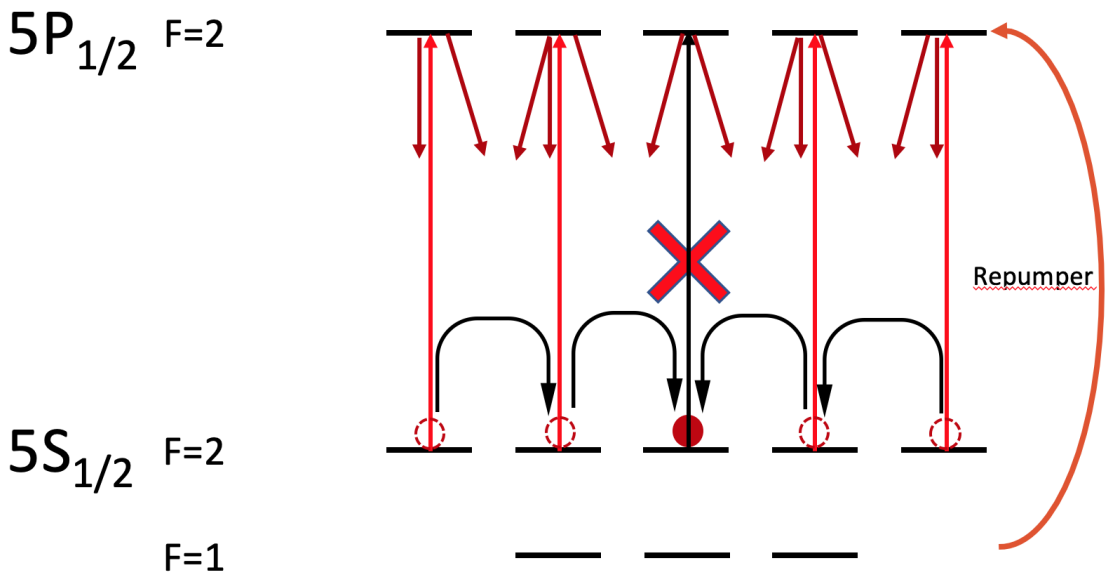

Figure 3.16: Diagram showing D1 Optical pumping of Rb87. Repumper brings atoms from the F=1 ground state back into the pumping cycle

heating due to the optical pumping ligh (assuming there is no polarization mismatch, which I will cover later). If the atom starts in the $|m_f = 1\rangle$ state, then the atom is excited to the $|m'_f = \pm 1\rangle$ state, and decays back to either the $|m_f = \pm 2\rangle$, $|m_f = \pm 1\rangle$ or $|m_f = 0\rangle$ dark state. If the atom starts in the $|m_f = \pm 2\rangle$ it will decay down to either $|m_f = \pm 2\rangle$ or $|m_f = \pm 1\rangle$. Looking at the branching ratios for these transition, and considering each step, one could attempt to calculated the heating based on how many times on average the atom must be excited and decay back down before the atom ends in the dark state. Let's calculate this for the simple case where we assume perfect polarization of the OP light, and neglect the chance that the atom can decay to the $|F = 1\rangle$ level. The probability the atom is in any given m level is equal, at 0.2. The trivial case is where the atom starts in the m=0 dark state; the number of steps is 0. Without loss of generality, we can consider just the $|m_f = 2\rangle$ and $|m_f = 1\rangle$ states, as they should be equal to the $|m_f = -2\rangle$ and $|m_f = -1\rangle$ states by symmetry.

For the case of $|m_f = 1\rangle$, the atom is excited with π polarized light, and then has the following branching ratios: $|m_f = 2\rangle = 1/3$, $|m_f = 1\rangle = 1/6$, $|m_f = 0\rangle = 1/2$. If the atom ends up in the $|m_f = 2\rangle$ state, then the probabilities when it falls back are: ($|m_f = 2\rangle$ =2/3 , $|m_f = 1\rangle$ =1/3). Therefore, if we assume an equal starting distribution the probability P_n(m=0) that the atom is in the $|m_f = 0\rangle$ state at step n is

$$P_0(m = 0) = 0.2$$

$$P_1(m = 0) = P_0(m = \pm 1) * 1/2 + P_0(m = 0) = 0.4$$

$$P_2(m = 0) = P_1(m = \pm 1) * 1/2 + P_1(m = 0) = 0.5$$

$$...$$

with the probability that P_n(m=0) 0.99 occurring at n = 25. If we go through the same process including the probabilities that the decay can go to $|F = 1\rangle$ or $|F = 2\rangle$, then the n where P_n(m=0) 0.99 occurs at n$\sim$29. This can give an intuition for how many photons we may need to scatter in order to pump our state. While the 0.99 level happens around 25 scatters, the vast majority take far less, and in fact the average number of photons that need to be scattered to end in the Dark state is about 11 if we assume the use of an un-polarized repumper (about 5 if we use a linearly polarized repumper)

3.6.2 Density Matrix Formalism

Another way that I used to quantitatively analyze how many photons needed to be scattered to pump our state is to solve the master equation for our system, and integrate over the excited state population. Using the Lindblad equation:

$$\frac{\partial \rho}{\partial t} = \frac{-I}{\hbar}[H, \rho] + \sum_j \gamma_j (L_j \rho L_j^\dagger - \frac{1}{2}\{L_j^\dagger L_j, \rho\}) \tag{3.1}$$

Where H is the Hamiltonian of our system, and ρ is the density matrix and L are the non-Hermitian operators called the Lindblad operators which encapsulate the dissipative effects of the system[68]. The form of the Lindblad operators depend on whether the sources of dissipation are energy conserving. For the purposes of this simulation, they take the form of "collapse" operators which describe the radiative decay of between two states of the system.

$$L_{ij} = \sqrt{\gamma_{ij}} \left|I\right\rangle \left\langle j\right| \tag{3.2}$$

Using these relations, we can generate a set of differential equation which when numerically solved simultaneously describe the evolution of our system.

3.6.3 Simulation Results

For the simulation of our optical pumping, I generated a Hamiltonian whose basis vectors were the 32 hyperfine m-levels of the $5S_{\frac{1}{2}}$,$5P_{\frac{1}{2}}$,$5P_{\frac{3}{2}}$ states of ^{87}Rb. I used Mathematica to generate and solve the system of equations describing the evolution of the system simulating this system with parameters reflecting the actual parameters that were used in our experimental setup ($10\frac{mW}{cm^2}$pump, $2\frac{mW}{cm^2}$ repump) gives the following results.

An interesting result that is perhaps not surprising when considering the earlier discussion of branching probabilities, is that that total number of scattered photons is quite robust against changes in laser power. The rate at which the dark state is reached depends on the laser power , but since the number of average photons scattered does not change the heating as a result of the optical pumping also is relatively constant. This is assuming, of course, that the polarization purity of the pumping light is well defined. If there is even a small deviation in the polarization angle of the pumping light, then the state will no longer be completely dark. Looking at the Wigner-d matrix values for say, a 5 degree deviation of the π-polarized light from

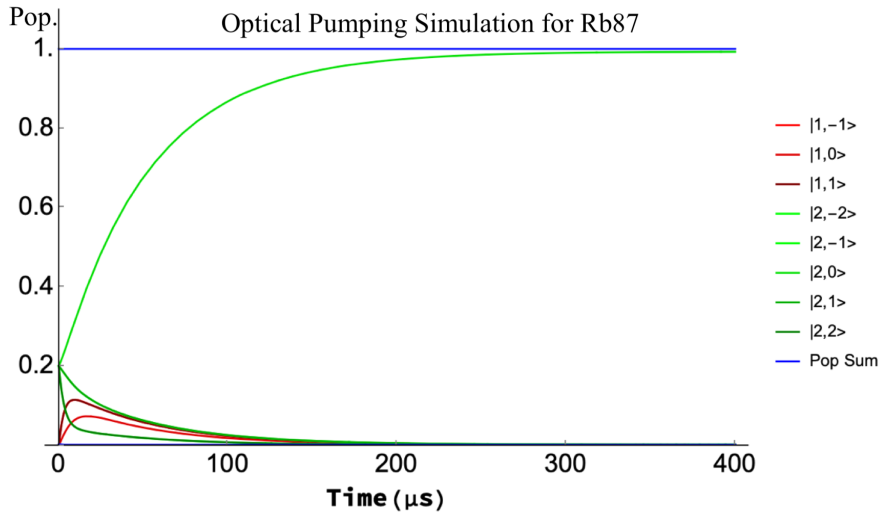

Figure 3.17: Rb87 clock state optical pumping simulation results

the quantization axis, gives only about 99 percent purity of the linear polarization. This will cause the atoms to slowly scatter more photons over time, and will limit the fidelity of the optical pumping as a whole.

The use of an unpolarized repumper vs an "optimum repumper" also has a considerable effect on the heating. Optimum in this context means that the repumper has the same polarization as the pumping light. The intuition for why this is the case is that if the repumper is unpolarized, then there is a chance that the atom can be repumped in a direction counteracting the pumping, actually taking the atom further from the dark state. An unpolarized repumper will have a chance of changing m by $\pm 1, 0$. however, a σ-polarized repumper will also move the atom towards the dark-state, effectively contributing to the pumping of the state. In the case of π-polarized pumping, the comparison is not as stark, but having a π-polarized repumper does give a small improvement over an unpolarized repumper, where some of the atoms end up having to scatter several more photons as they fight the random walk of the repumper away from the dark-state. Some of the atoms do end up scattering less

photons because they happen to be repumped towards the dark state, but since there is a minimum number of photons that theoretically need to be scattered, but there is no maximum, it turns out that on average more photons are scattered with an unpolarized repumper for this case. Additionally, the amount of time that high-fidelity pumping takes is increased for the unpolarized repumper in both cases for the same reason: Some atoms will take much longer than average to reach the dark state. Therefore the benefit of using a repumper with a polarization matching that of the pumping light is that you can get higher fidelity pumping faster, with fewer photons scattered. This means that the atoms will remain at a colder temperature. The recoil temperature for Rb87 at 780nm is

$$T_{\text{recoil}} = \frac{4\hbar^2\pi^2}{mk_b\lambda^2} \approx 362\text{nK} \tag{3.3}$$

Since the number of scattered photons is low, unless the atoms start at a very low temperature the benefit in heating compared to the stretched and clock state pumping is negligible. And the difference between repumper polarizations within those schemes is even more so. Figure 3.19 shows the difference between stretched state and clock state pumping for starting temperatures of 5μK and 50μK. For the 50μK it is clear that the difference in temperature is very small, only about 10%. For the 5μK, it is much more substantial with the clock state pumping being about twice as hot as the stretched state pumping. Likewise, you can see that the difference between using an Optimal repumper versus an unpolarized repumper is small, even at 5μK, but not negligible. Switching to using a repumper with the same polarization as the pumping light can make a significant difference in the atom temperature if you are starting at a sufficiently cold temperature.

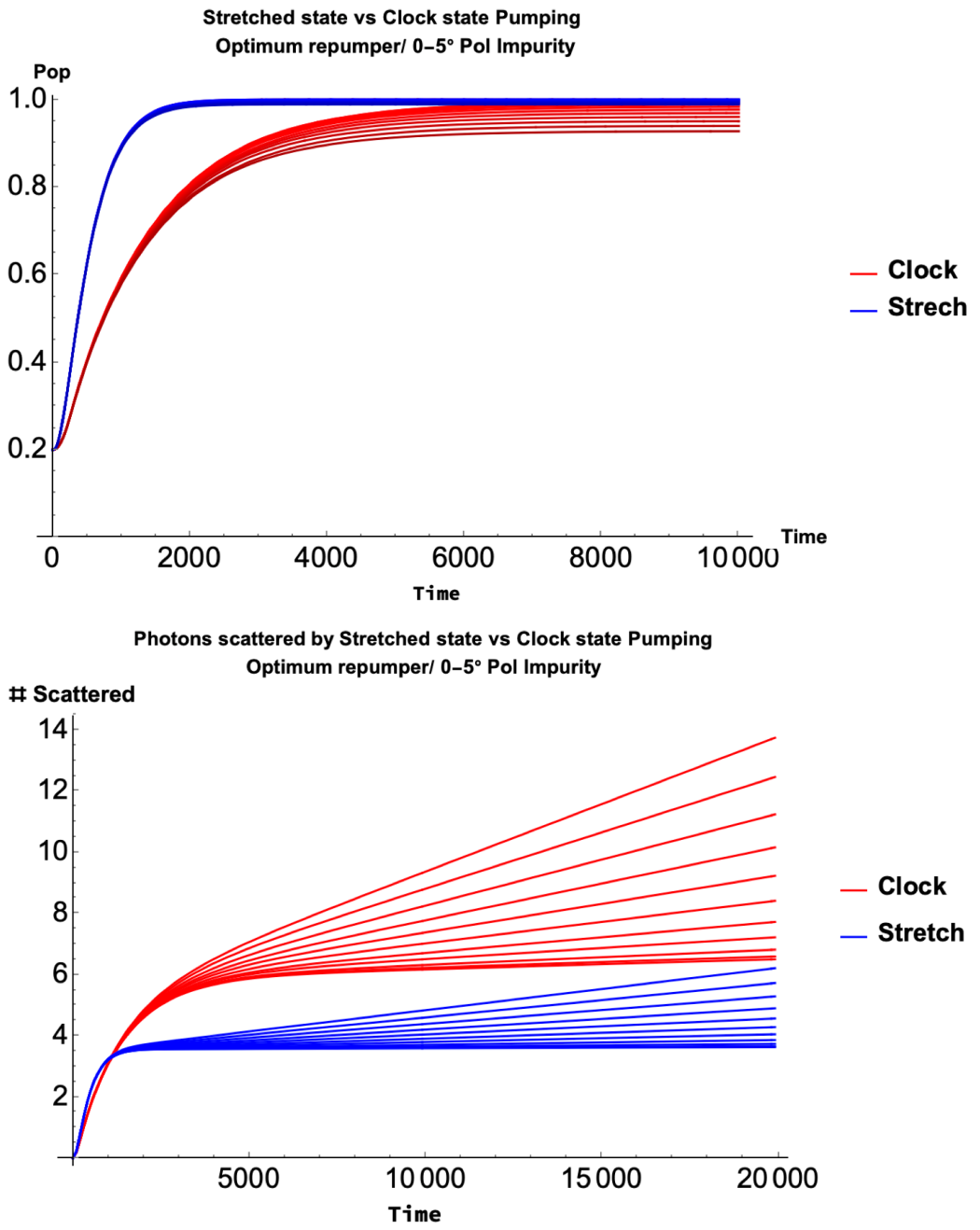

Table 3.1: Simulation results showing the effect of pumping light polarization purity on the pumping time and number of photons scattered.

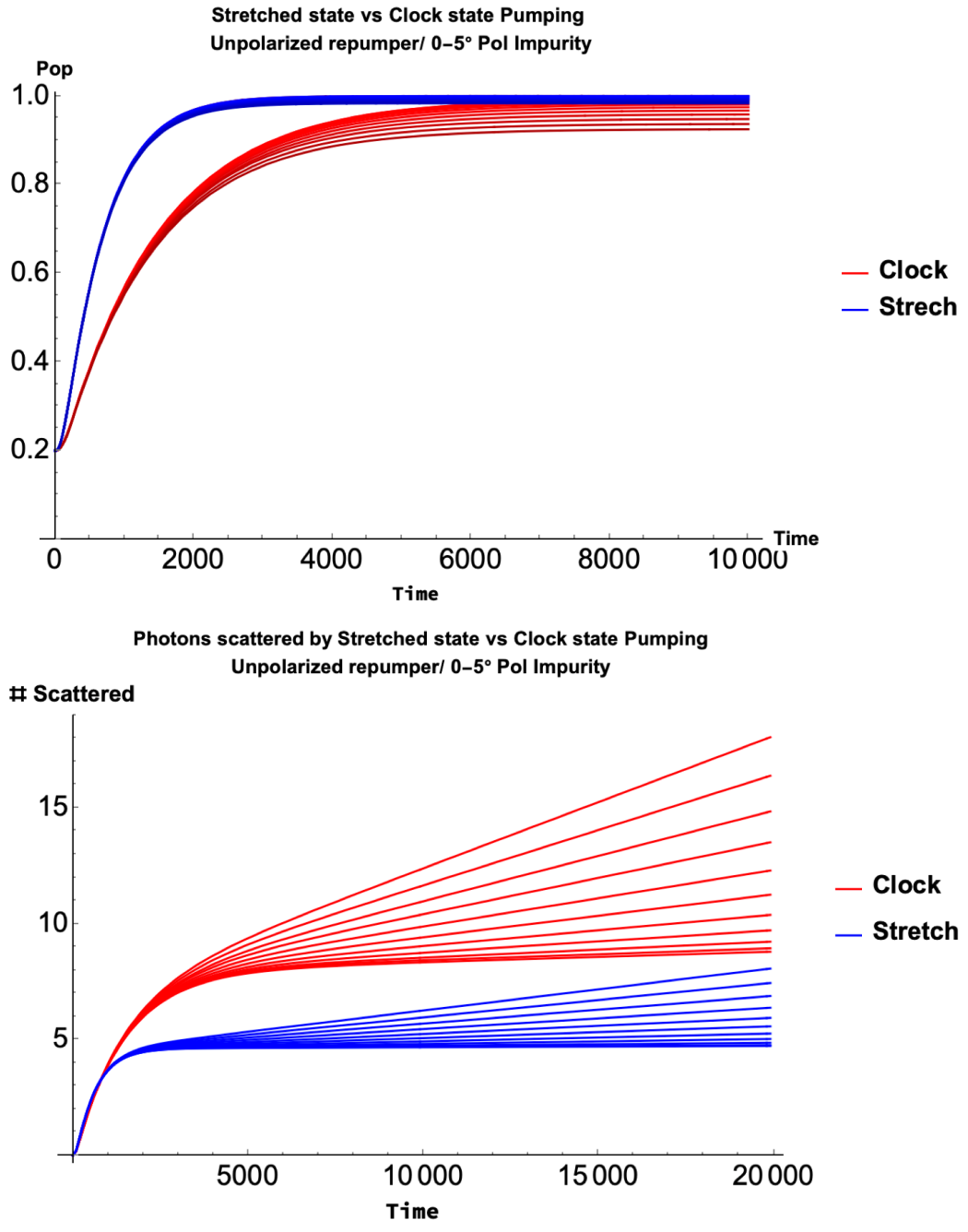

Table 3.2: Simulation results showing the effect of pumping light polarization purity on the pumping time and number of photons scattered.

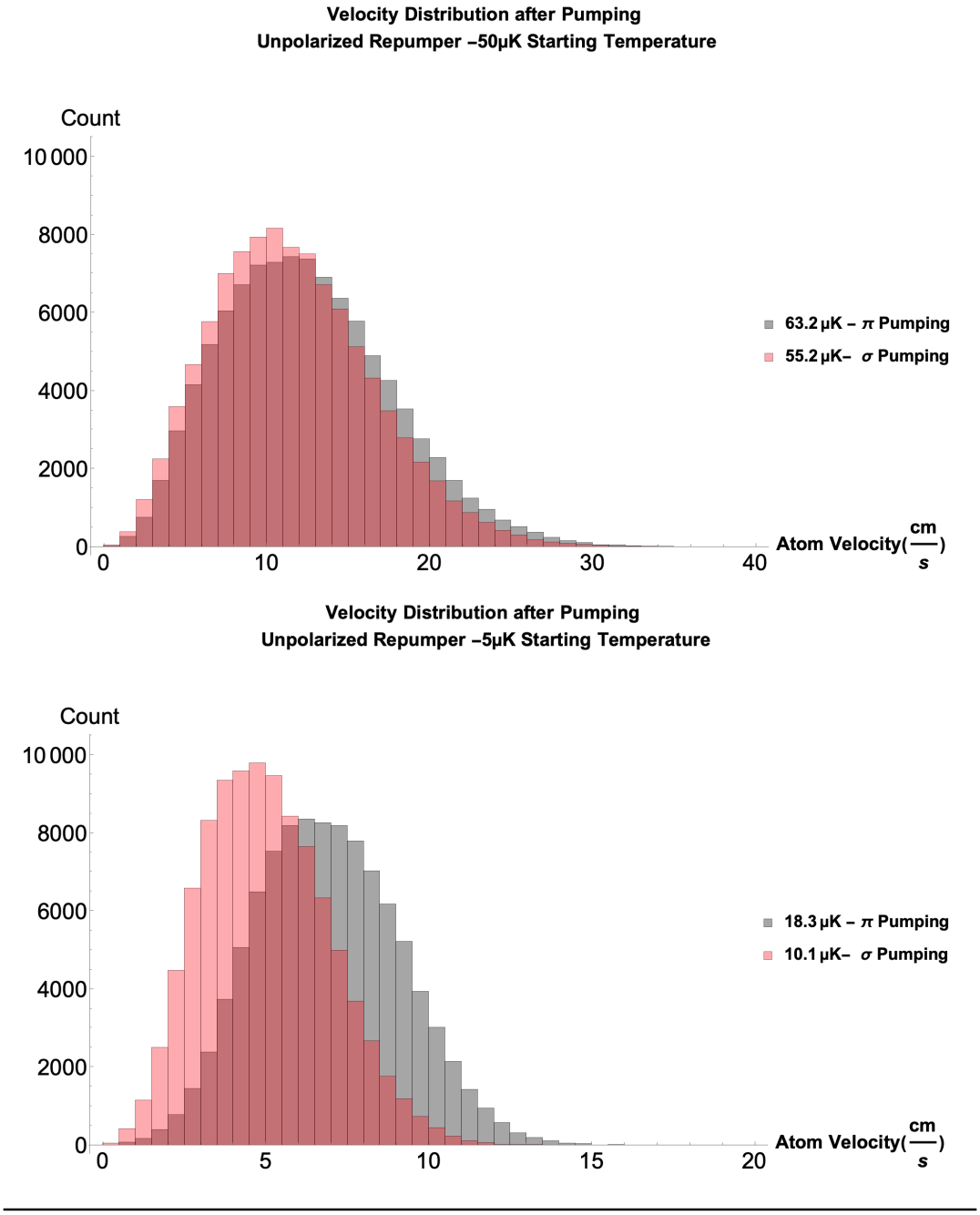

Figure 3.18: Simulation results showing the effects of using a polarized vs unpolarized repumper on the final temperature of the atoms. This is shown for two different starting temperatures, with a lower starting temperature seeing a larger benefit from using a polarized repumper.

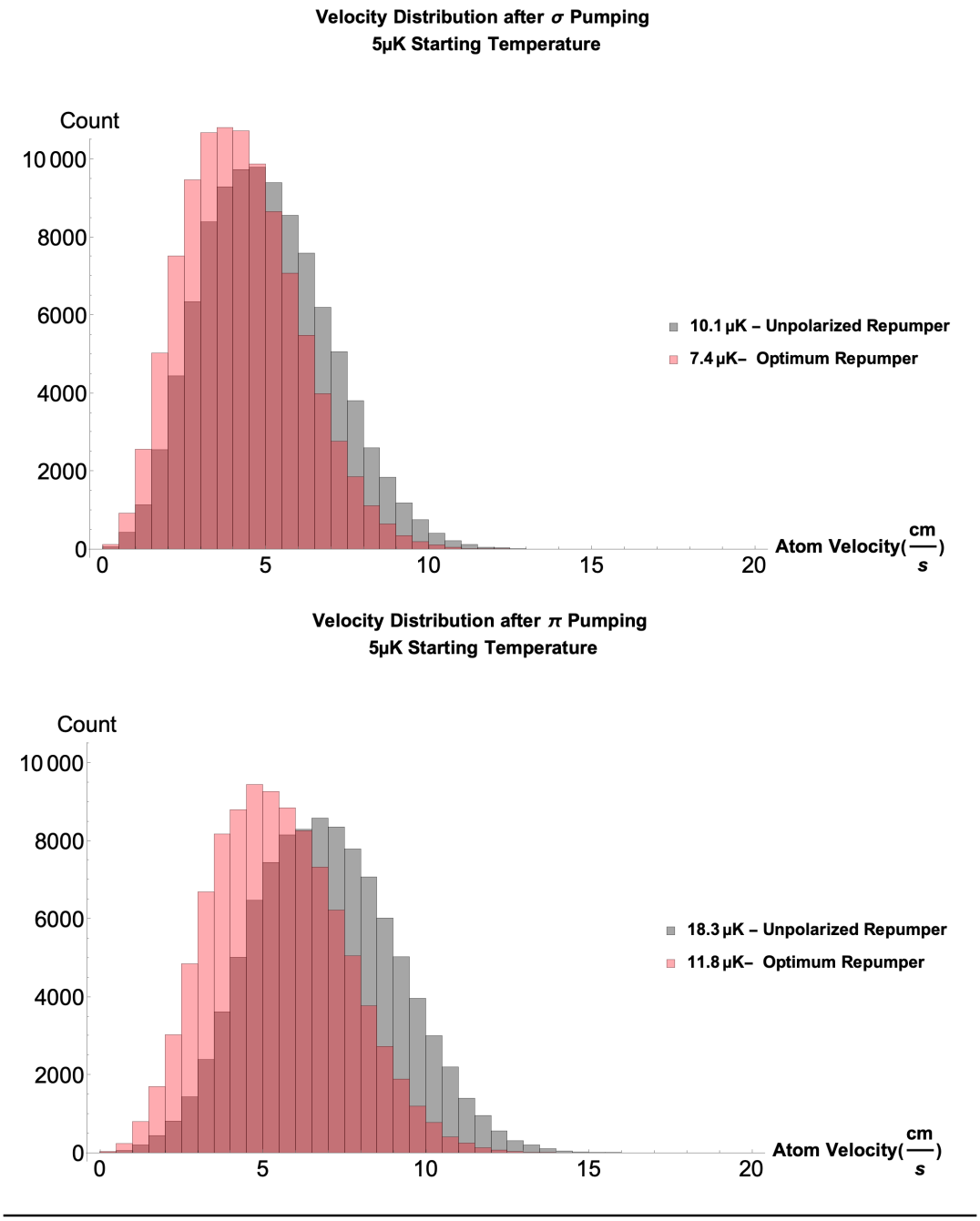

Figure 3.19: Simulation results showing the effects of using a polarized vs unpolarized repumper on the final temperature of the atoms. This is shown for two different starting temperatures, with a lower starting temperature seeing a larger benefit from using a polarized repumper.

3.7 Rydberg Simulation

During the $\sim$ 3 months of 2020 when everyone was quarantined at home, I took the opportunity to expand upon the framework that I had made to simulate optical pumping(sec3.6 in order to look at possible sources of dephasing of our Rydberg signal. As has been mentioned numerous time in this thesis and in Minho's thesis [41], we had severe dephasing of our Rydberg signal since the rebuild of the system. There were multiple things that we thought might be causing all or part of our dephasing.

Other factors that we wanted to quantify were how the atom temperature and addressing beam misalignment effected our Rydberg dephasing. If the atom temperature is too high, the localization of the atom inside of the trap is poor. When the Rydberg excitation happens, the amount of power that the atoms sees will vary shot to shot, and this will result in a dephased signal as the Rabi Frequency will have a large variance. In a very similar way, if the alignment of the Rydberg addressing beams is poor(this includes both transverse and axial alignment), then the atom will be sitting in a location where the variance in the beam power is larger, which makes the Rabi frequency more sensitive to atomic motion of the atoms.

For additional details about the simulation, see sec3.6. I simulated the atoms by classically moving them within the trap as they would during an experimental sequence in our actual experiment. I then used a density matrix approach calculate the response of the atoms to the Rydberg addressing fields as the atoms moved within those fields. Rb87 Atomic levels included in the calculation were all hyper-fine levels of $5S_{1/2}$, $5P_{3/2}$ and a singular Rydberg level representing the $84D_5/2$ state.

Results of the simulation suggest that atom temperature alone cannot explain the dephasing that we have observed in our Rydberg Rabi-Oscillations. Even for atom temperatures up to 150μK the decay rate of the oscillation is more than double what we have observed with atoms temperatures of $\sim 150\mu$K. Additionally, addressing beam

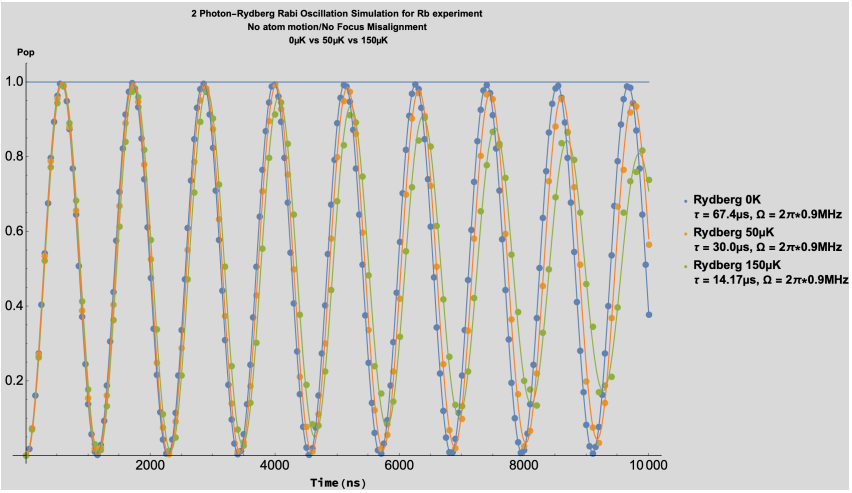

Figure 3.20: Rydberg Rabi Oscillation dephasing simulation while varying atom temperature.

misalignment required to see the observed dephasing is not able to solely account for what we observe. There is a measured[17] astigmatism of the 780 addressing beam, as can be seen in fig 3.22, which causes the atoms to sit at a location which is not precisely at the point of the beam with the flattest profile. However, the atomic motion in the dipole trap is small enough that the axial misalignment has a very minimal effect on the dephasing. The transverse misalignment can in fact realistically be large enough that it causes serious dephasing. However, to connect the level of dephasing that we observe with the simulation would require $> 1\mu$m of misalignment. As is discussed in sec 3.8.1, great care was taken to align the Rydberg beams to the atoms. This includes the axial and transverse alignments as well as the k-vectors of the beams. Additionally, errors in the k-vector can mask transverse misalignments on the camera, resulting in a larger error then is apparent. This being said, we do believe that our error was less than 1μm based on our measurements. It is of course an option that more than one of these factors contributed to our dephasing. This was never determined. However, this simulation provided support for the construction of

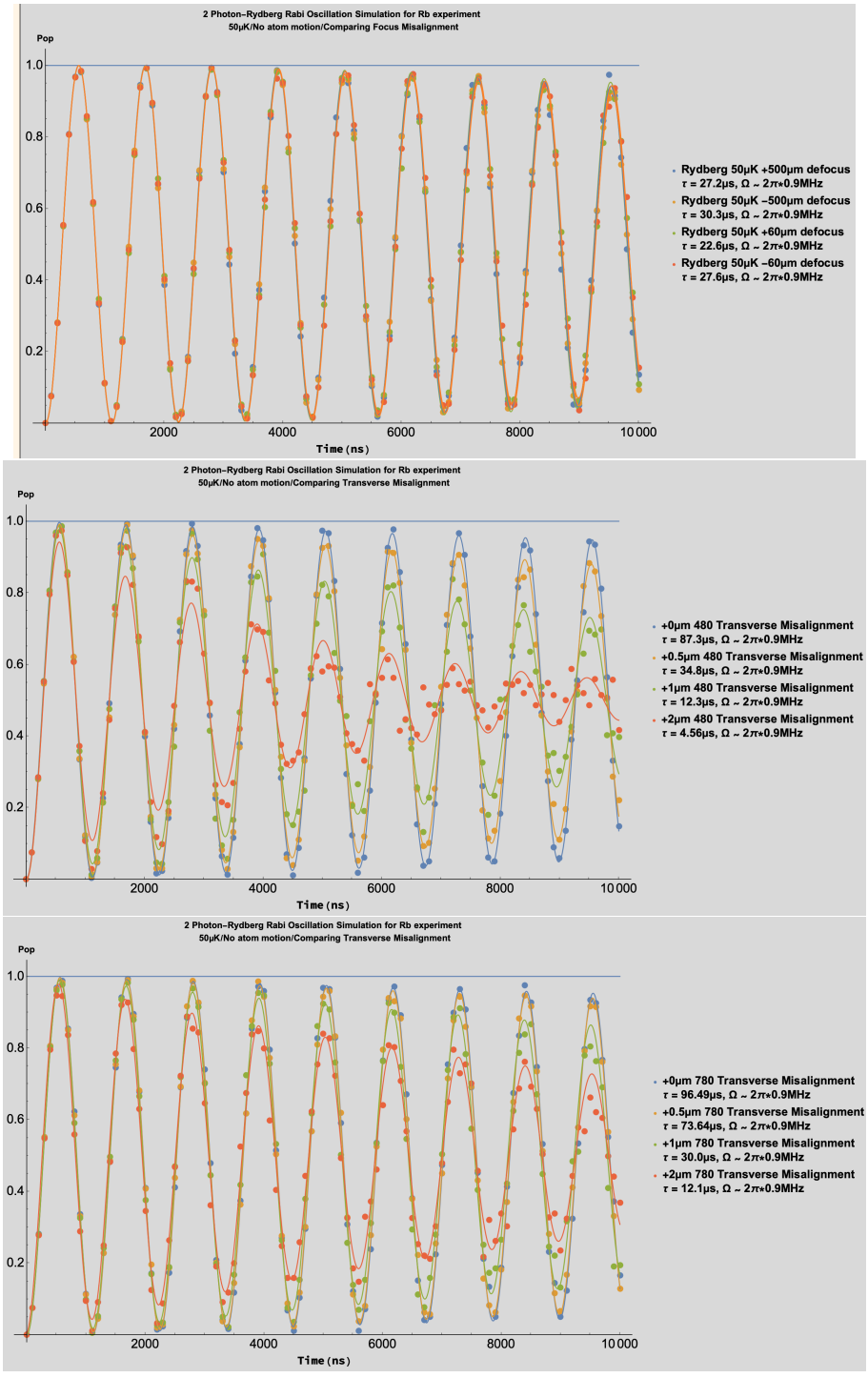

Figure 3.21: Rydberg Rabi Oscillation dephasing simulation while varying the transverse and axial misalignment of the addressing beams.

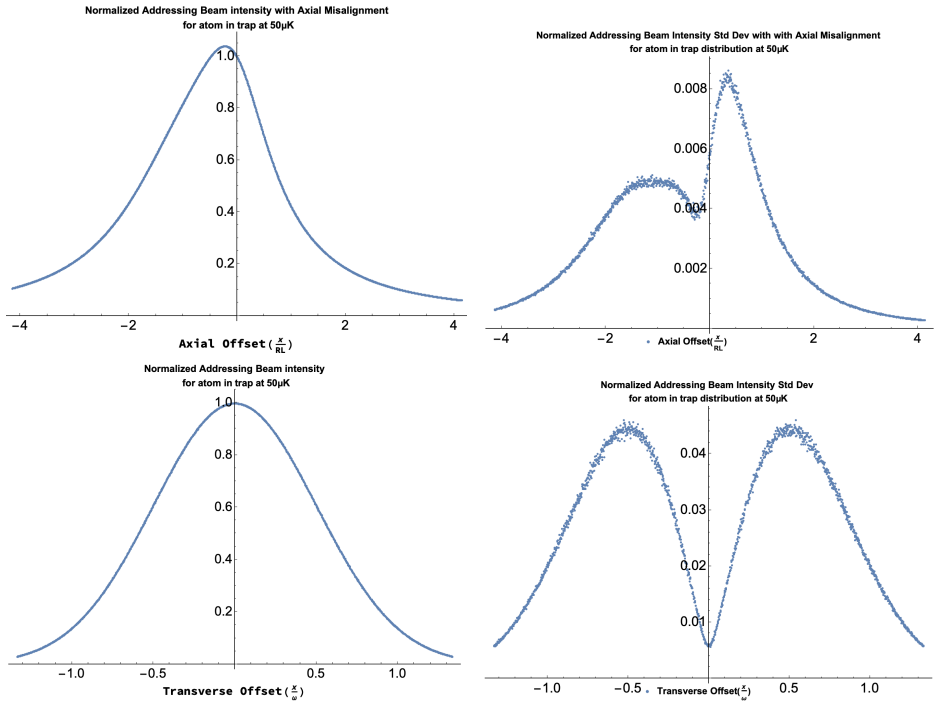

Figure 3.22: Plots showing the Intensity variation in the addressing beams for our specific setup. For transverse misalignment, plots shown reflect the high-quality Gaussian cross-section of our addressing beams (Fig.3.10) . Axial misalignment plots reflect the 250μm astigmatism between the x and y focus of our 780 addressing optics. Optics were aligned such that the atoms were coincident with the x focus of the addressing beams.

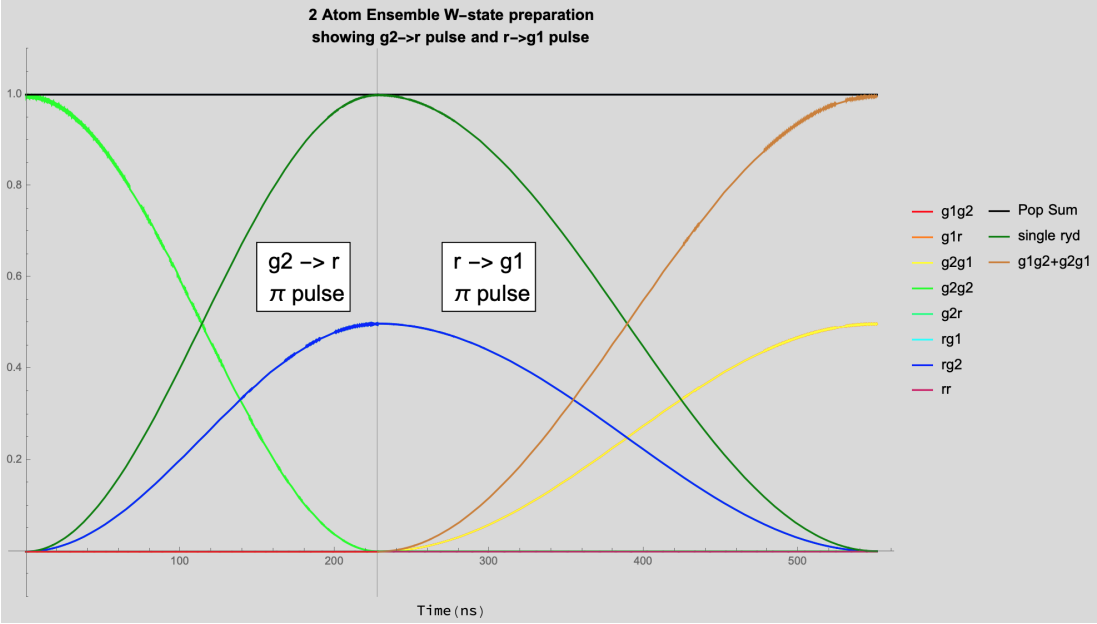

Figure 3.23: W-state simulation using realistic experimental parameters. Dark Green trace shows that the probability of a single Rydberg excitation goes to one after first π-pulse from the $|F = 2\rangle$ ground state. Final state after second π-pulse is W-state between ground qubit states. This plot merely shows that simulation of W-state generation was possible, but this project did not continue on to include sources of noise. The next step would be to simulation W-state preparation given a certain level of dephasing.

Servo-bump filtering cavities, which are discussed in detail in sec3.4.1. Laser noise is another potential caused of dephasing.

3.8 Results: Problems and Solutions

In this section I would like to step back and discuss the results we did end up getting on the rebuild of the Rb ensemble qubit experiment and why those results were not what we wanted/expected, what things might have gone wrong that caused us to get those results, and what steps were taken to address them. For additional information about this experiment, see [17] [41].

3.8.1 Results

Initial results on the rebuild showed severe dephasing. As can be seen in Fig 3.24 during coherent Rydberg oscillations between the ground state and $|97d_{5/2}, m_j = 5/2\rangle$ there was dephasing to zero population observed.

RF induced dephasing

The dephasing seen in Fig 3.24 was caused by the 5GHz Wi-Fi band which had been implemented around the time of the rebuild. Nearby Rydberg states with dipole transitions around 5.2GHz ($|95f_{5/2}, m_j = 5/2\rangle$ and $|99p_{3/2}, m_j = 3/2\rangle$) turn our effective two level system in a three level system, where atoms in the $|97d_{5/2}, m_j = 5/2\rangle$ can rapidly bleed into the nearby Rydberg states. Since these Other Rydberg states are not brought back into the ground state, when the trapping laser turns back on atoms left in a Rydberg states are lost. On our signal, this manifests as oscillations dephasing to zero population.

A previous decision to switch from the n=111 to n=97 Rydberg level had been

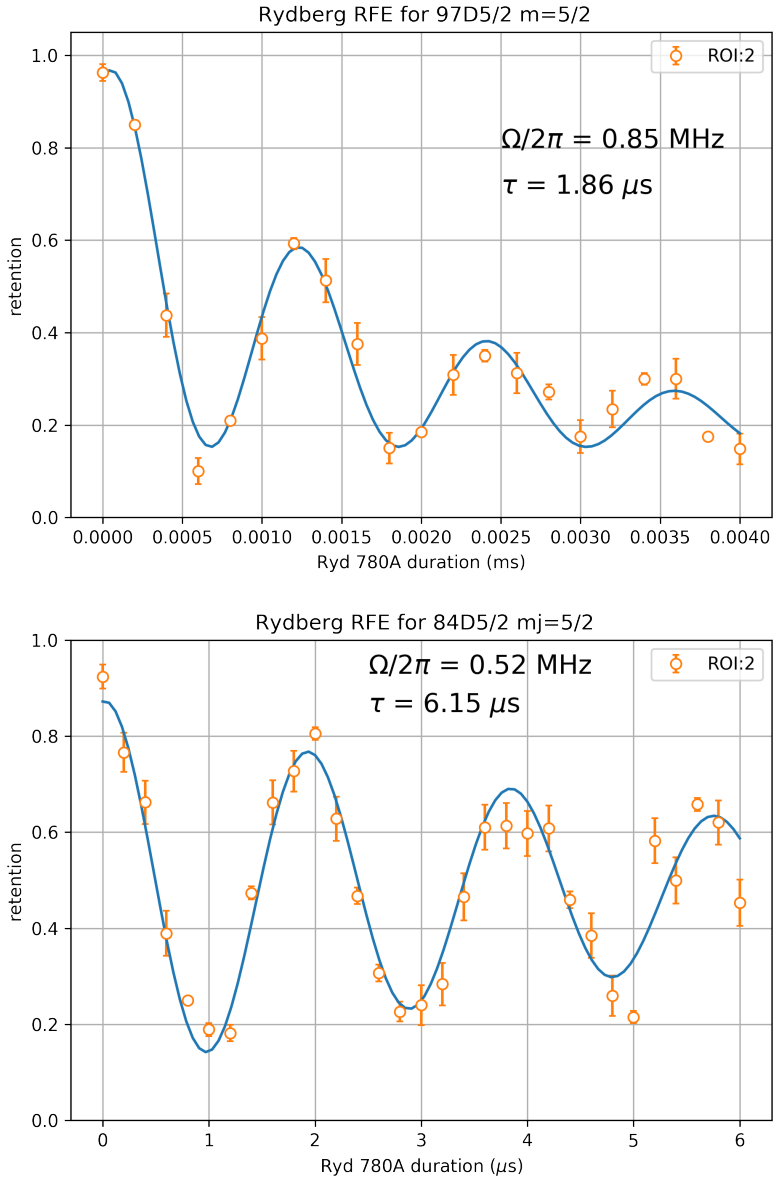

Figure 3.24: Top image is showing RF induced dephasing of Rydberg signal. This is indicative of what was seen in initial result on the rebuild of the Ensemble experiment. Bottom image shows an typical example of the higher quality single-atom Rydberg Rabi flopping we achieved post-rebuild.

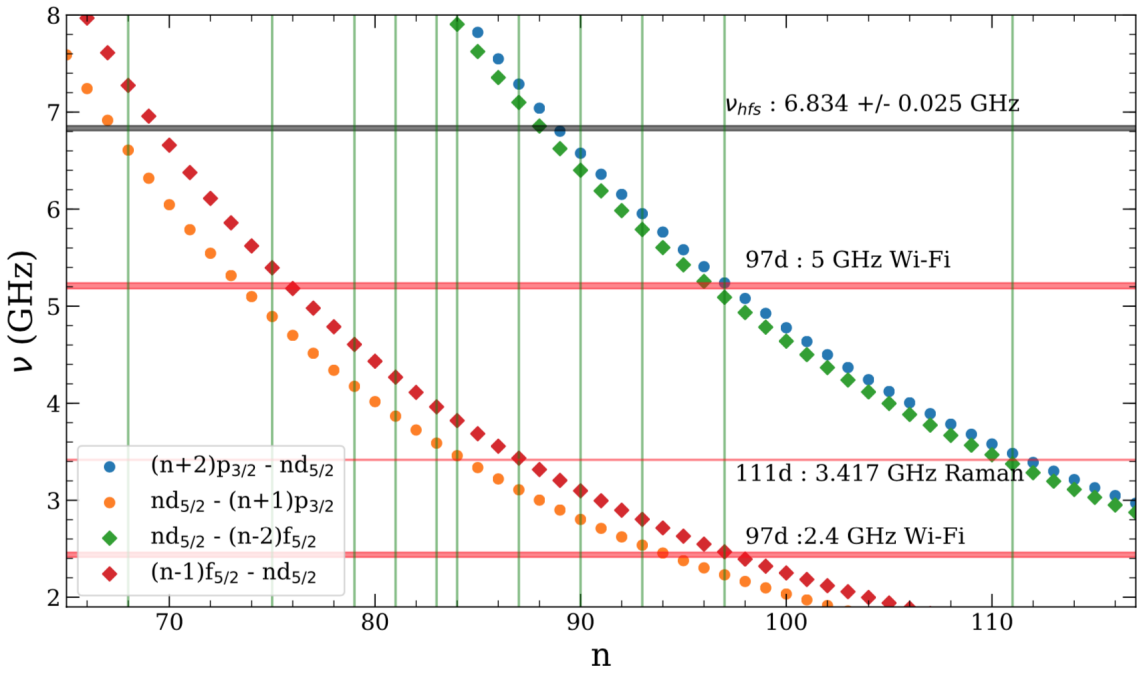

Figure 3.25: From Minho Kwon's Theses[41]. Chart shows Dipole-allowed transitions from $nD_{5/2}$ states. Vertical Green lines show the levels accessible given the ULE cavity FSR. Transition frequencies are calculated using ARC-Rydberg Calculator Python package

made due to a similar issue with the 2.4GHz Wi-Fi band. Nearby Rydberg states had dipole transitions at a MW frequency close enough to the Wi-Fi band to observe dephasing. A couple factors contributed to the resurfacing of this problem for the $|97d_{5/2}, m_j = 5/2\rangle$ state. As mentioned during the rebuild, usage of the 5GHz Wi-Fi band was ramped up during the construction of the rebuild. This means that even though using the $|97d_{5/2}, m_j = 5/2\rangle$ state had given decent results previously, which did not show dephasing to zero, it was now observed. Furthermore, this dephasing was observed despite the construction of the RF-shielding box that we constructed around the apparatus (section 3.2). This turned out to be due to the fact that RF was leaking into the connection to the 3W amplifier connected to our MW horn that we used to drive ground-state rotations. Ahead of the amplifier we use a narrow 6.834GHz band-pass filter to moderate the signal seed the amplifier. However, this filter was not directly connected to the amplifier. This allowed 5GHz to enter the system in the cables connecting the filter to the amplifier, which proceeded to pump this signal straight onto the atoms. We were able to ultimately discover this problem by driving a different, lower RF frequency, $|84d_{5/2}, m_j = 5/2\rangle$, which we would use going forward. This signal immediately showed dephasing to 0.5 population, indicating that the atoms were not leaving the 2-level system.

Part of the solution was to move the 6.834GHz band-pass filter to be directly connected to the amplifier. This should reduce the amount of noise that is able to seed the amplifier and reduce the RF noise at the atoms. We also moved the amplifier into the RF shielded box to reduce the amount of RF noise the amplifier was exposed to. Ultimately however, the n^7 scaling of the polarizability was too much and even with the adjustments we made we could not completely eliminate the problem. We ended up making a permanent change to address the $|84d_{5/2}, m_j = 5/2\rangle$ state instead (This choice was based on which frequencies we could address using our ULE cavity

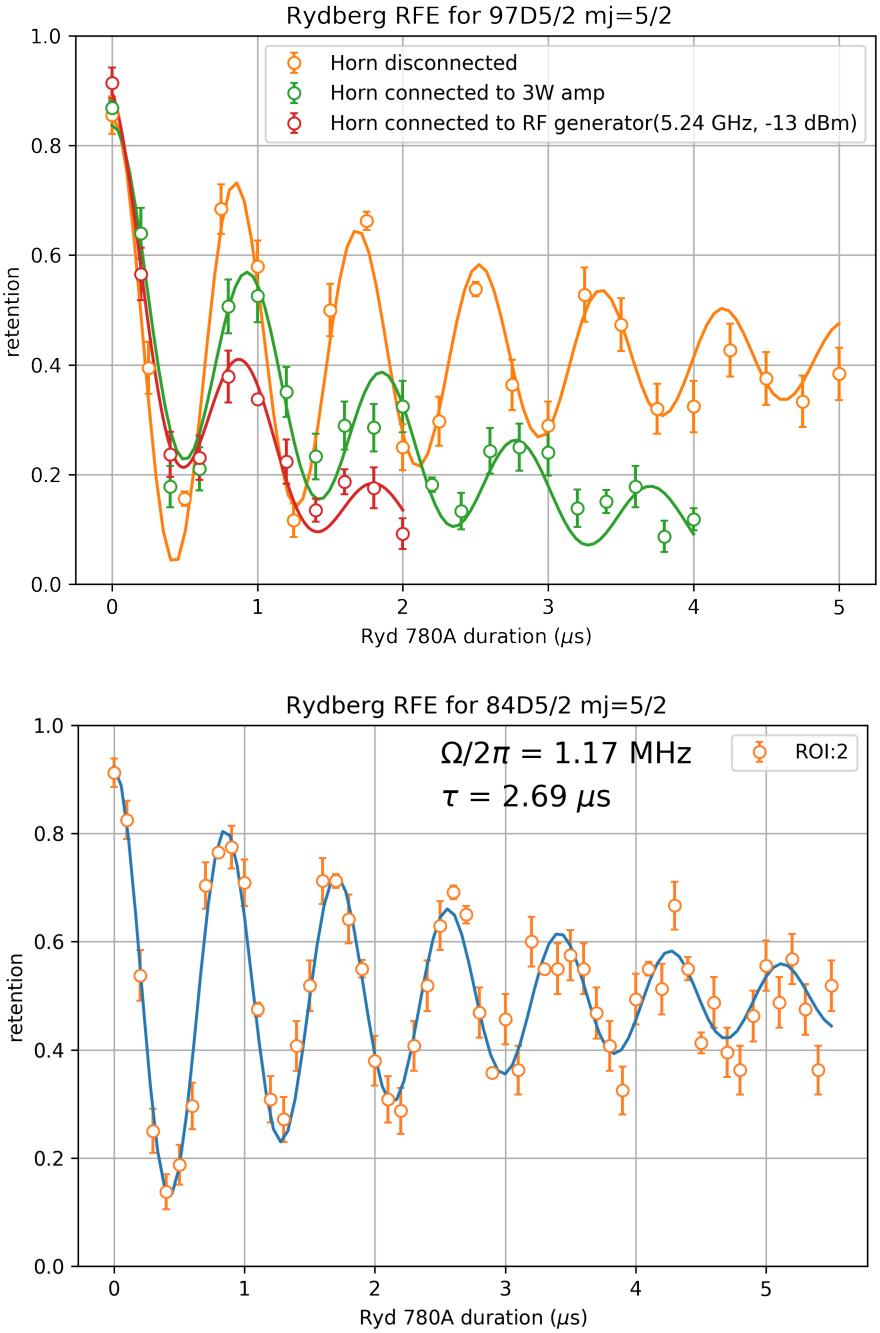

Figure 3.26: Side-by-side comparison of $|84d_{5/2}, m_j = 5/2\rangle$, and $|97d_{5/2}, m_j = 5/2\rangle$ Rydberg signals, taken within 2 days of each other. The only significant change is the Rydberg level being addressed, indicating that the source of dephasing is a background RF field driving transitions between the $|97d_{5/2}, m_j = 5/2\rangle$ state and nearby Rydberg levels, whereas the $|84d_{5/2}, m_j = 5/2\rangle$ state does not have nearby levels resonant to the same frequencies, and so the population is not lost.

lock, which has an FSR of 500MHz). There is still severe dephasing of our Rydberg oscillation at this point however.

Atom Temperature

One of the possible things that could cause dephasing in our Rydberg oscillations is atomic motion with respect to the addressing beams. As can be seen from Fig 3.22, atomic motion in the traps results in the atom sampling different intensities of the addressing beam. This has two major consequences that effect the coherence of our Rydberg signal. One is that because the atom experiences different addressing beam intensities, the atom is going to have a different Rabi frequency depending on where it is in the trap. Both radial and axial displacement in the trap (although radial displacement has a much larger effect). In section 2.1 it is shown that for a two-photon transitions, the Rabi frequency is

$$\Omega_{2p} = \frac{\Omega_1 \Omega_2}{\Delta_1 - \Delta_2}$$

Where $\Omega_i = \frac{d_i E_i}{\hbar}$ is the single photon Rabi frequency, and Δ_i is the single photon detuning. If the atom is significantly moving around inside of the trap between measurements, then the intensity of the light observed by the atom will change. The changing intensity will reduce the 2-photon Rabi frequency proportional to the square root of the intensity for a single addressing beam, and it will also change the detuning of the addressing beams because the AC-stark shift for an atomic level is $\frac{-1}{4}\alpha_i|\mathcal{E}|^2$ which is proportional to the intensity as well. At was discussed in more detail in sec 2.1.1, for a two photon transition, like the one that we have here, the condition that we want to satisfy to be insensitive to this effect is that the single photon Rabi-frequencies of our addressing beams are equal, so that the quadratic AC-stark shift that the atoms see is effectively zero. The intuition being that if one of our beams is red-detuned (like our 780nm addressing beam which is ∼2GHz red detuned from the

intermediate transition) and the other is blue-detuned (like our 480nm addressing beam is) then the AC stark shifts of those two lasers will effectively cancel if the Rabi-frequencies are the same. Effectively this means that we want to satisfy:

$$\mathcal{E}_1 d_1 \approx \mathcal{E}_2 d_2 \tag{3.4}$$

where d_i is the matrix element for the given transition. In our case, the matrix element between the $|5S_{1/2}F = 2, m_f = 0\rangle$ state and the $|5p_{3/2}F = 3, m_f = 1\rangle$ state is $\sim$ 1.26ae. The matrix element between the $|5P_{3/2}, m_j = 3/2\rangle$ state and the $|84D_{5/2}, m_j = 5/2\rangle$ state is about 250 times smaller at $\sim$ 0.005ae. What this means is that in order to have equivalent Rabi frequencies, the intensity of our second addressing laser needs to be $\sim 250^2$ or 64000 times greater than our first addressing laser. The maximum 480nm laser power that we typically could expect to deliver to the atoms was $\sim$ 20mW, with a 4μ waist. This corresponds to an intensity of $\sim$40000$\frac{\mathrm{W}}{\mathrm{cm}^2}$. If we choose our 780nm power to match this so that the Rabi frequencies are equal the 780 intensity would need to be $\sim$0.6$\frac{\mathrm{W}}{\mathrm{cm}^2}$, corresponding to a 2-photon Rabi-frequency of 100kHz. This is quite slow. In the past, we had been able to deliver more blue power to the atoms with better conversion efficiency in the SHG cavity creating the 480nm light from 960nm light.[41]. However, given the amount of 480nm light that we had, we made the decision to increase the 780nm power to $\sim 9\mu$W of power, which gave us a Rabi frequency of $\sim$ 1MHz. However, the result is that we were more sensitive to AC-stark shift changes due to atomic motion in the trap. A smaller effect that starts to become significant if the atoms get much hotter is the increased Doppler shift that the atoms sees of the addressing beam frequencies. Our to addressing beams counter-propagate(Fig A.1) which eliminates the Doppler-shift to a first approximation, but since the lasers have different frequencies there is still a non-negligible shift that occurs.

All of this is to say that if our atoms are hot, then dephasing of our Rydberg signal

can occur. In the simulation of our Rydberg Rabi flopping in our dipole trap(3.7), I tested how much dephasing of our single atom Rydberg signal we should expect to get for a given atom temperature. The conclusion there was that our atoms would have to be very hot, $\sim$100s of μK to dephase our signal this much. This makes sense because for a 2π-rotation with 2 photon Rabi frequency of 1MHz, at a temperature of 150μK the atom should only move at about 10cm/s, or about 120nm during the addressing period. This is very small compared to the waist of the addressing beams, and so the amount of dephasing is just really not enough to explain what we saw on its own. Given that with the PGC we were able to get(fig 3.15) $\sim$40μK, we believe that it is unlikely that the atom temperature is a major cause of our poor signal. (Certainly, if we had been getting 0.99 percent population transfer, getting the atoms as cold as possible would have been a major concern.) Additionally, as was shown in [1], on this exact experiment before the rebuild, they were able to get Rydberg signals with much better coherence with N=7.6 atoms at $\sim$150μK. Additionally we saw no improvement in our Rydberg signal with increased Dipole trap depth. This should more tightly confine the atoms to a single location but this had no noticeable effect on the Rydberg signal.

Addressing Laser Alignment

Another way that dephasing could be caused is due to the misalignment of the addressing beams with respect to the atoms. This is related to the discussion about the atom temperature, except that instead of the fast atomic motion causing the dephasing, the atom is sitting in a location where the beam is varying rapidly, such that its normal atomic motion at a cold temperature would cause dephasing. There are essentially 3 ways that the Rydberg beams can be misaligned, which are shown in figure 3.27 Transverse misalignment, that is alignment perpendicular to the direc-

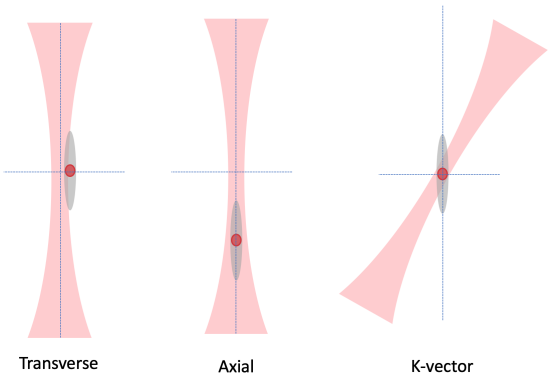

Figure 3.27: Three types of misalignment that can affect our addressing beams.

tion of the addressing laser, has the largest effect on the quality of the experiment in question. Since the goal is to address a single site, the beam must be very narrow in the transverse direction. In our case, our addressing beams have waists of a few microns. This means that a transverse misalignment of hundreds of nanometers is noticeable; microns is completely devastating. Transverse misalignment is also the easiest to measure and correct. Axial misalignment is not as much of a problems because the variation in the beam intensity along its axis is much less that the transverse variation. With Rayleigh lengths in the ∼100s of microns, the only very severe axial misalignments would be noticeable, and the variation local to the atom will still be small. K-vector misalignment, that is a misalignment of the angle of the beam, should not have a significant effect on the dephasing. The main concern with k-vector misalignment is that the polarization purity will be affected.

780 addressing laser As was mentioned in the section about the Automatic Alignment system, the way that we aligned the 780nm addressing beam was to use a Ramsey-style measurement, where we use the addressing beam to impart a differential AC-Stark shift between the $|5S_{1/2}F = 2, m_f = 0\rangle$ and $|5S_{1/2}F = 1, m_f = 0\rangle$ levels. Since the magnitude of this differential shift is proportional to the intensity of the

light, if the addressing beam is misaligned, then the Ramsey-fringe will have a smaller frequency (Fig 3.4). When the intensity of the beam is maximized, the frequency will be at its highest. This method is also discussed in the Automatic Alignment system section. Using this method, we were able to keep the beam locations stable to within ∼100nm. Measurements of the beam location with respect to the dipole trap using the AAS camera show that this method is accurate and repeatable. Additionally, transverse alignment of both addressing lasers happens before every Rydberg signal. Axial misalignment of the 780 addressing laser is known from the initial measurements made during the construction of the system[17]. Astigmatism introduced by the pointing-AOM used to control the addressing beam position separates the X and Y foci of the beam by $\sim 250\mu$m. The optics of the apparatus are setup in such a way that the X-focus occurs at the atoms, which means that the Y-focus is locate about 250μm behind the atoms. This is the cause of the asymmetrical shape in Fig 3.22. Unfortunately, adjustment of the axial alignment is not built into the optics, and therefore we never adjusted it. The beam waist measured from the alignment scans discussed earlier are consistent with the known waist of the 780 addressing beam, and we took that as confirmation that drift in the axial direction did not occur. Furthermore, based on simulation (section 3.7, Axial misalignment of any reasonable amount could not explain the observed dephasing that we saw. Additionally, we were not able to measure any significant K-vector misalignment of the 780 addressing beam.

480 addressing laser The 480 addressing beam is much more difficult to align. This is partly because it is focused to a smaller waist (4μm compared to 6μm) which makes it more misalignment sensitive, but there is also no easy way to measure the alignment using the atoms like there is for the 780 addressing beam. We have typically used the Rydberg signal itself to optimize the alignment of the 480 addressing beam. By optimizing the population transfer to the Rydberg state with a short pulse, we

can find the center of the beam. There are many reasons why this is a difficult process, but assuming that you have the correct detuning and 780 beam alignment, this process is quite straight forward. You scan the X and Y coordinates of the beam using the pointing-AOM and find where the rate of population transfer is the largest. Since the 480 addressing beam is counter propagating to the 780 addressing beam, it is not visible on the camera used for the automatic alignment system. It is however visible on the EMCCD used to collect fluorescence from the atoms.

The location of the 480 laser on the EMCCD does not overlap exactly with the atoms, but it is accurate in the sense that locating the image in that spot specifically could reproducibley align the 480 addressing laser to the extent that a Rydberg signal was detected. From there a normal alignment scan using the Rydberg signal could be done. Axial alignment of the 480nm laser was also confirmed using the Rydberg signal. The focusing triplet (Fig A.1 was on a Newport 9081 5-Axis stage, which allowed for the adjustment of the lens along the axial direction. We were able to determine in 2019 that there was a k-vector misalignment of the 480nm addressing laser. Before this point, the 480nm showed up on the EMCCD well below the atoms, which was later determined to be due to a k-vector misalignment (Fig 3.30. The way that we corrected this was by coupling the 780nm addressing beam into a fiber located at the location of the AAS camera. We then removed the breadboard associated with the blue optics, and re-imaged the 480nm and 780nm (now being launched from that same fiber launcher) onto a camera mounted on a 3-axis stage. This setup allows us to use the light launched from the fiber as an analog to the light counter-propagating the to 480nm beam through the cell, since they should follow the same path. Adjustment of this camera along the axial direction showed the 780nm addressing beam did not move with respect to the camera, indicating that the k-vector of this beam was well aligned to the axis. However, the blue beam did move significantly, showing an off

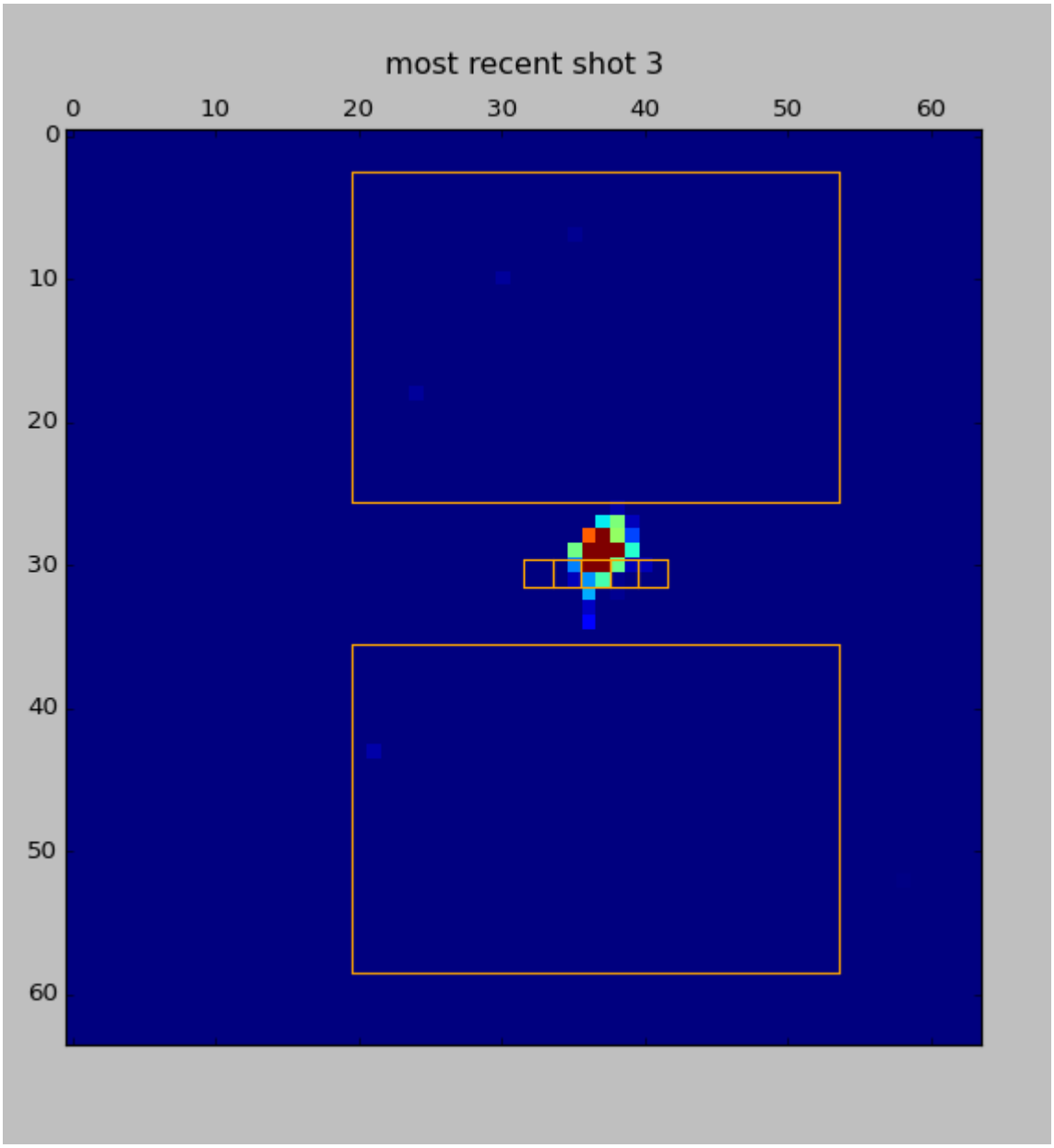

Figure 3.28: Image of Blue addressing laser on the EMCCD camera after k-vector realignment. 5 boxes in the center indicate the 5 atomic sites.

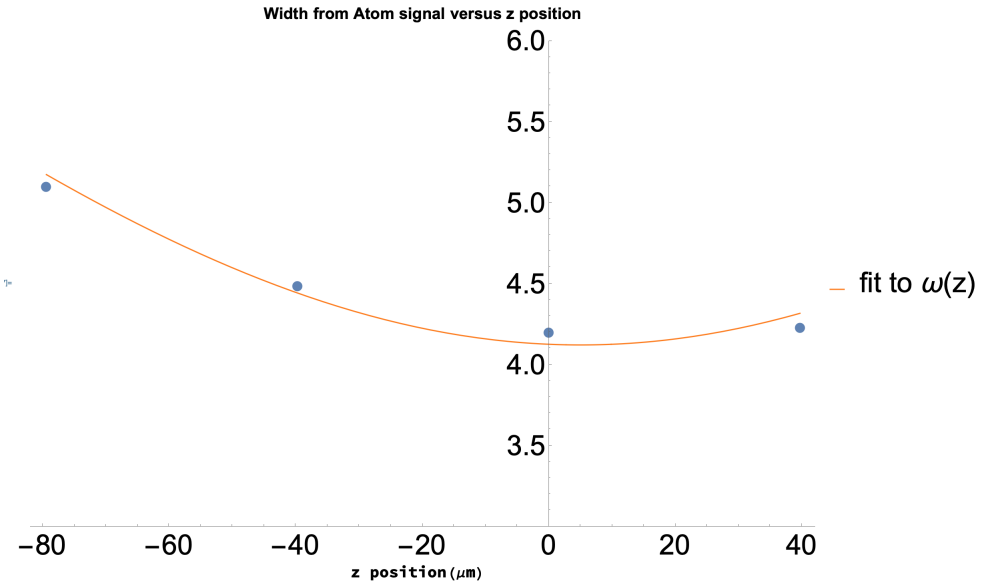

Figure 3.29: Axial alignment scan of the 480nm addressing laser. Locating the focus of the beam was done by doing a transverse scan of the 480nm laser in the X-direction, and measuring the waist of the Rydberg signal. This was done for multiple axial locations, and the minimum waist was determined. This confirmed that the focus of the laser was, in fact, correctly located at the atoms. Final fit to $\omega[z] = \omega_0\sqrt{\frac{(z-z0)^2}{(\mathrm{L_R})^2}}$ gives $\omega_0 = 4.12\mu$m, and $\mathrm{z}_0 = 5\mu$m.

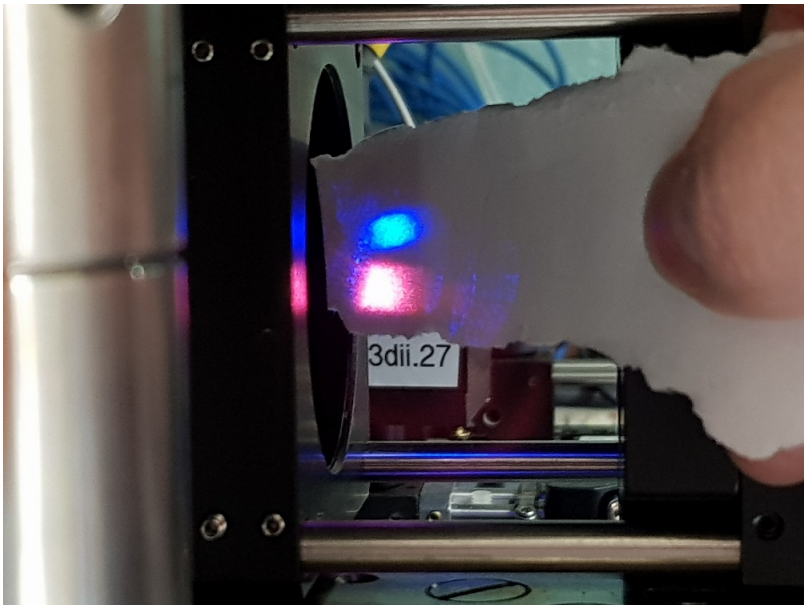

Figure 3.30: 480/780 k-vector misalignment. Image here is showing the displacement in the Fourier plane. 770nm light is shown through 780nm optics for a brighter spot.

axis k-vector. By adjusting the optics of the 480nm addressing beam, we were able to have the 780 and 480 both insensitive to axial movement on the camera while also being focused at the same location. We also confirmed the σ_+ polarization of the 480nm addressing beam at this time as well. Reinstalling the optics into the system, we found that the 480nm beam showed up much closer to the atoms on the EMCCD camera, indicated that the k-vector had been substantially improved. (anecdotally, we actually detected a Rydberg signal right after this without having to search at all.) However, this change did not show a detectable improvement to the dephasing of our Rydberg signal.

Rydberg Laser Noise

One of the main challenges of doing high precision Rydberg experiments is having very clean, narrow lasers with which to address the atoms. In our case we PDH lock

our lasers to a ULE cavity, attaining linewidths in the ∼kHz range. We split off a portion of the laser to go to the lock, and the remaining portion is either used to seed an SHG cavity, as is the case with the 960/480nm laser, or it goes directly to the atoms as is the case with the 780nm laser. In either case, the PDH lock narrows the natural linewidth of the laser substantially, to a level which is suitable for doing Rydberg experiments, and high-fidelity quantum gates. There are a few factors that have to be accounted for however. Firstly, any time that you lock a laser, you introduce side-bands, or servo-bumps to the laser. This effectively means that you introduce frequency components to your laser that derive from the correction being made to the laser frequency to keep it resonant with the cavity. These additional frequency components can cause dephasing, especially when the frequency of the servo-bumps is near the Rabi frequency of the transition you are driving. One way to deal with the servo-bumps is to tune the parameters of the lock such that the amplitude of the servo-bumps is low enough that they will not meaningfully effect you (∼30dB below the carrier). This is not difficult to do, and it typically is sufficient to reduce the overall gain of the lock until the servo-bump amplitude is low enough. This also reduces the stability of the lock however. In practice, reducing the gain may not be an option because higher gain will make the lock more stable (up to the point where it starts to oscillate). As an alternative solution, we implemented filtering cavities to clip off the servo-bumps. These cavities are talked about in more detail in Section 3.4.1 but they are near-confocal Fabry-Perot cavities with linewidths in the 100s kHz range. This is broad enough that the carrier of the locked Rydberg laser can easily transmit through the cavity, but the servo bumps around ∼ 1MHz will not transmit through the cavity. This allows us to use higher gain on our ULE cavity locks, improving their stability, while also removing the 1MHz servo bumps from our signal. Evidence of the servo-bump cavities working for the 780nm addressing cavity is given

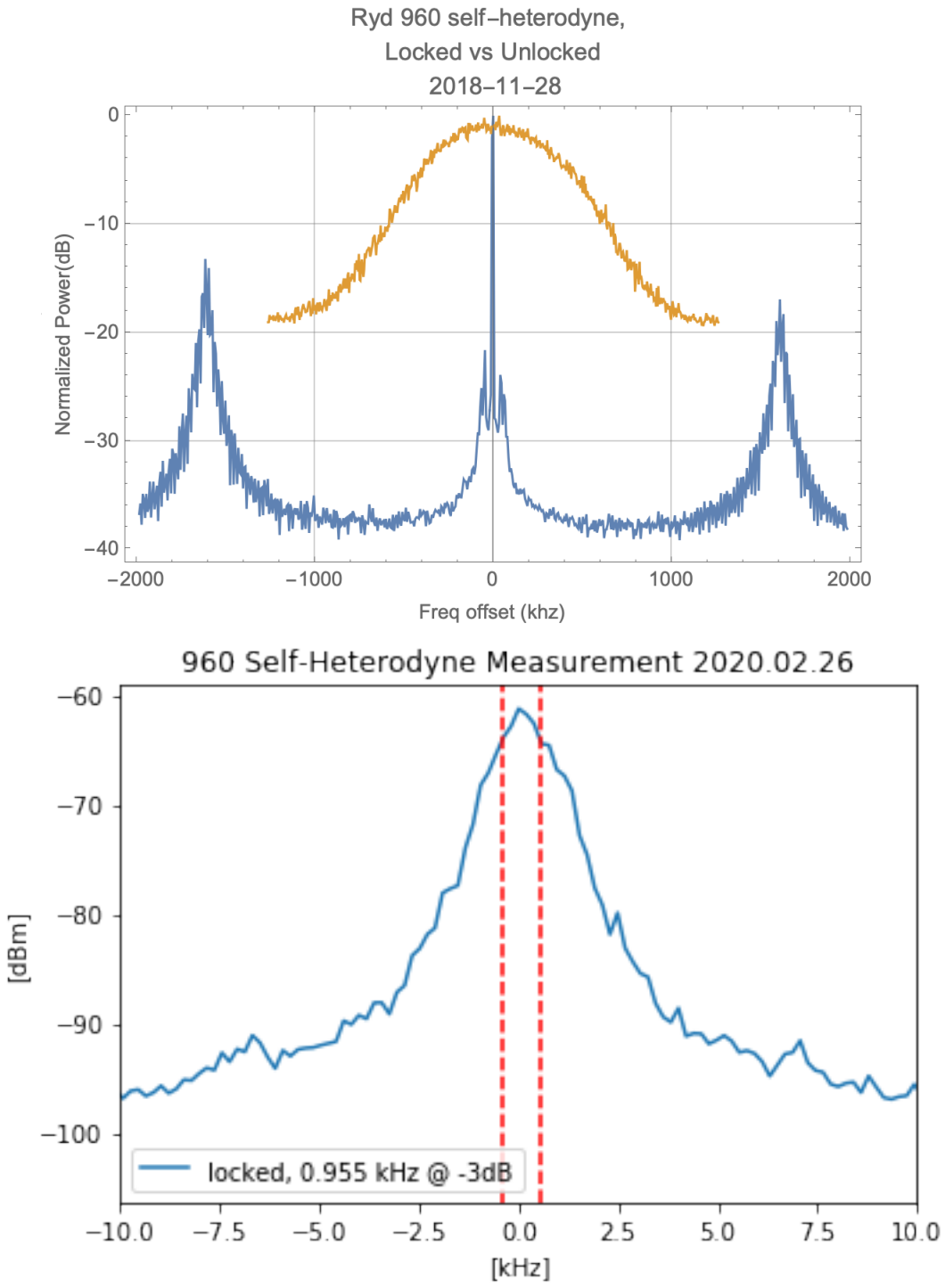

Figure 3.31: Self-heterodyne measurements showing the narrowing of the spectrum of the 960nm Rydberg laser and the addition of side-bands caused by the PDH lock.

in sect 3.4.1, however we have not yet installed the 960 filter cavity, and we were not able to fully explore how this effected our Rydberg dephasing before the experiment ended. Around the same time that had implemented the 780 filter cavity, we also discovered that sometimes the lock for the 480nm SHG cavity would be in a state that would cause large amplitude fluctuations on the 480nm light going to the atoms. These fluctuations were not visible on the photo-diodes that we were using to monitor the 480nm power. We measured the noise using a RIN measurement, the results of which are in figure 3.32. It was possible to tune the lock parameters such that the oscillations went away, however when tested against the Rydberg signal, the results showed that the 480 amplitude noise had no noticeable effect on the dephasing. This is shown in Fig 3.33. Ultimately, the conclusion of the laser noise issues is that we actually did end up addressing a lot of them, many of which may have been present throughout the lifetime of the rebuild, in particular the servo-bumps. We were not able to fully explore the effect that removing this noise had on the dephasing of our signal, nor were we able to confirm how much of our dephasing was due to laser noise. It is important to note though that at this point, shortly after we had filtered the servo bumps and fixed the amplitude noise on the 480nm laser, we were able to get the Rydberg signals shown in Fig. 3.34. These signals showed very promising results, with a lower rate of dephasing then we had ever seen previously.

Electric and Magnetic Field Noise

One of the final major sources of potential dephasing that will be discussed is stray electric and magnetic field noise. Since the polarizability of Rydberg atoms scales like $\sim n^7$, Rydberg atoms are exceedingly sensitive to electromagnetic fields. There has been extensive work done on using Rydberg atoms as RF antennas and sensors for weak electric and magnetic fields [31, 13, 3]. This also means that Rydberg

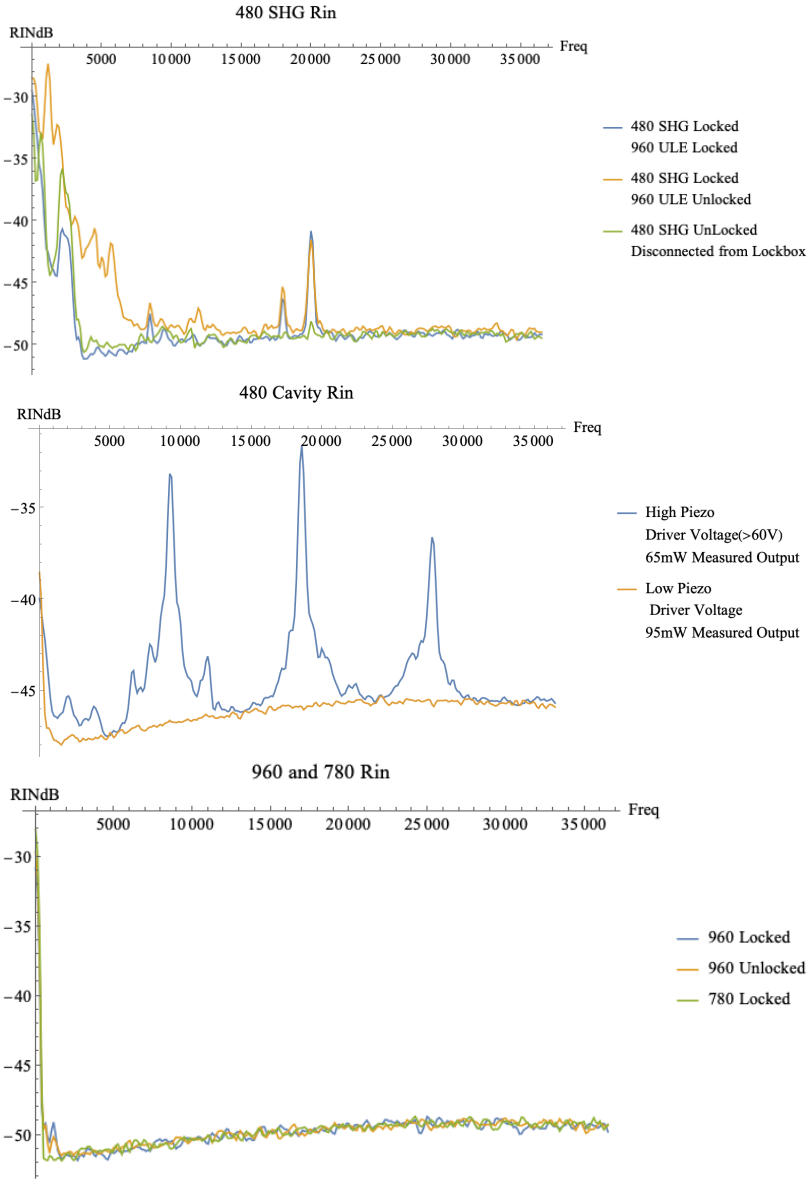

Figure 3.32: RIN Measurements showing the intensity noise introduced onto the 480nm light due to an unstable lock on the SHG cavity producing the 480nm Light from 960nm light locked to a ULE cavity.

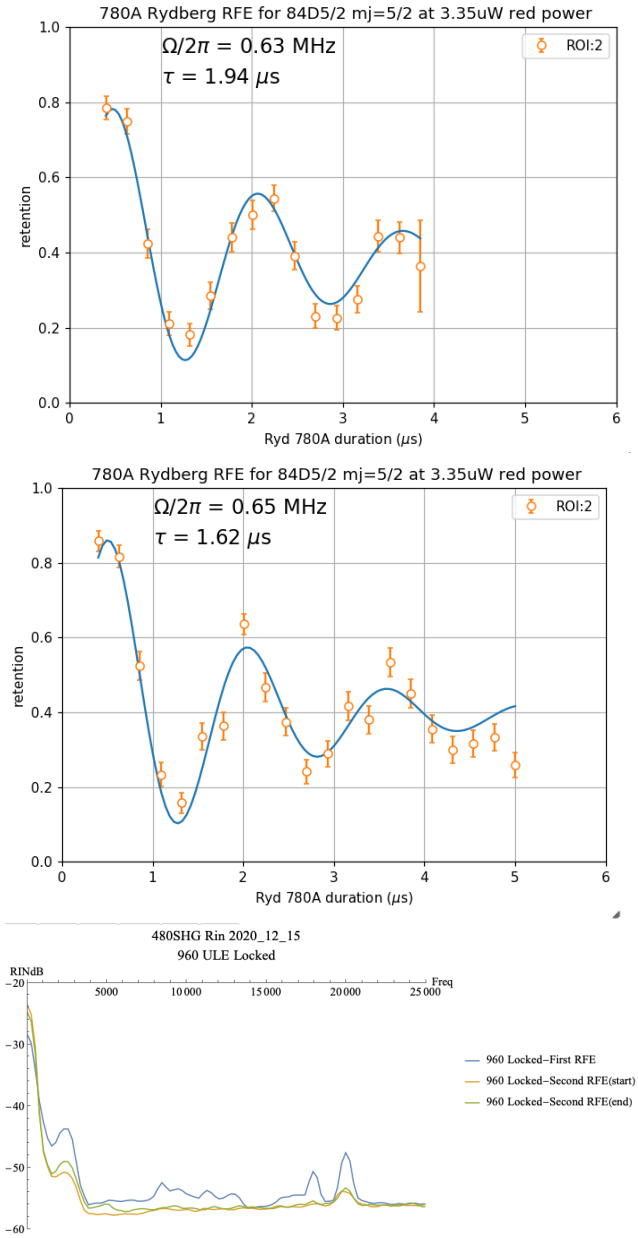

Figure 3.33: Two severely dephased Rydberg signals taken at different times. First signal was taken with deliberate intensity noise introduced onto the 480nm addressing beam through the SHG cavity lock. RIN is shown in the bottom plot. Second Rydberg Oscillation has low intensity noise. There was no discernible difference in the dephasing of the two signals.

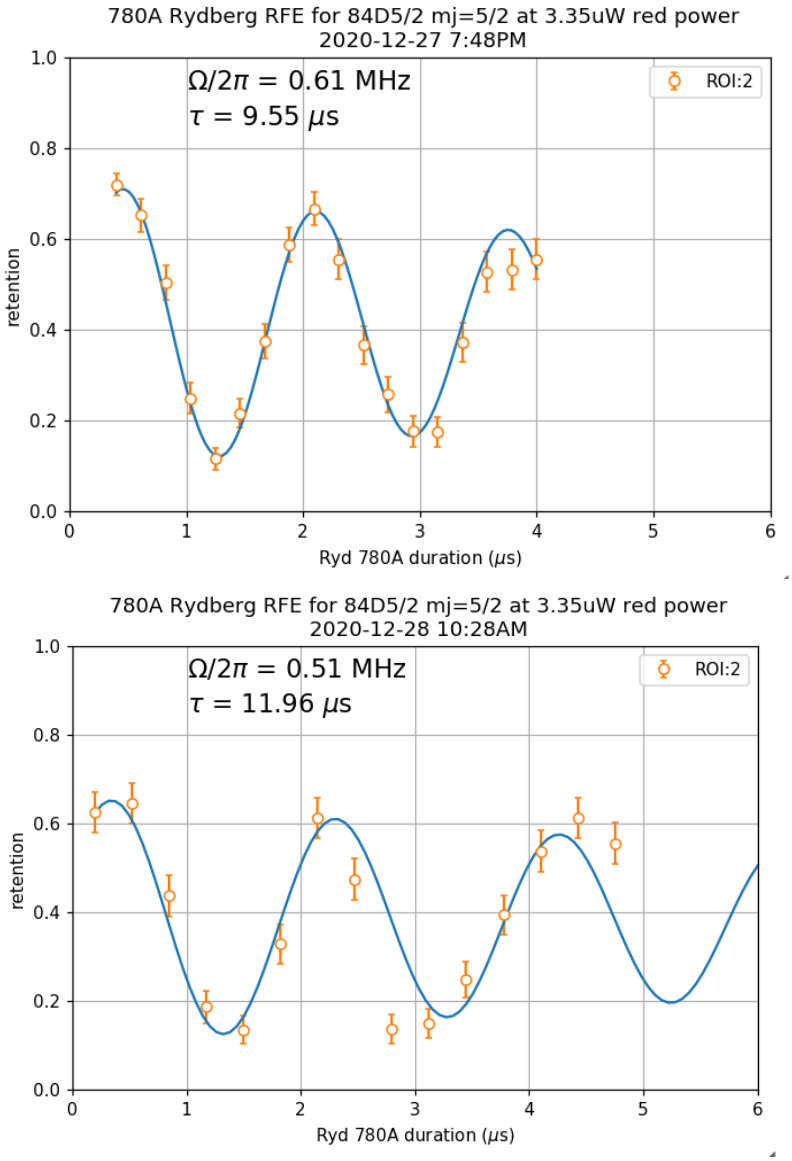

Figure 3.34: Rydberg signals showing the lowest rate of dephasing that we were able to achieve with our experimental setup. It's unclear what the cause of the low retention in this was.

atoms are very sensitive to unwanted background field. On several occasions, we had attempted to lower the Rydberg level down to $60D_{5/2}$ in an attempt to diagnose the extent to which laser noise or back-ground field noise was causing our dephasing. The idea being that if we lower the principle quantum number from n=84 to n=60, the polarizability should be $\sim$10 times less. If external field noise was a dominant cause of our dephasing, then we should see an improvement going to this lower level. If laser noise was the dominant cause of dephasing, that should stay constant between different Rydberg levels. However, these attempts were not successful due to a myriad of technical issues that have plagued the lab. Ultimately, we were never able to directly test this hypothesis. However, in December of 2020 we observed a new problem. We had been having a lot of other systemic issues with atom loading, retention and temperature that did not seems related our Rydberg issues, although they did make it harder to get the experiment in a state where we could successfully do Rydberg. However, we found that the detuning of our Rydberg lasers was changing rapidly. Fig 3.35 shows several TPS scans of our $84D_{5/2}$ Rydberg signal that all occurred within several hours of each other. From these results, it seemed as though either our laser frequencies were drifting or the magnetic fields was drifting. Given that the lasers were remaining locked and in healthy condition, we concluded that we must be observing fluctuations in the magnetic field at the atoms. We determined that we had a failure of our electronics controlling our magnetic field coils.

Conclusion

After the failure of the magnetic field coils, we were unable to reestablish a MOT in our upper chamber. This was determined to be due to lack of Rb87 atoms in the cell. Depletion of the atoms required us to open the cell up to replace the dispensers. I think that given the state of the experiment up to this point, we were very close

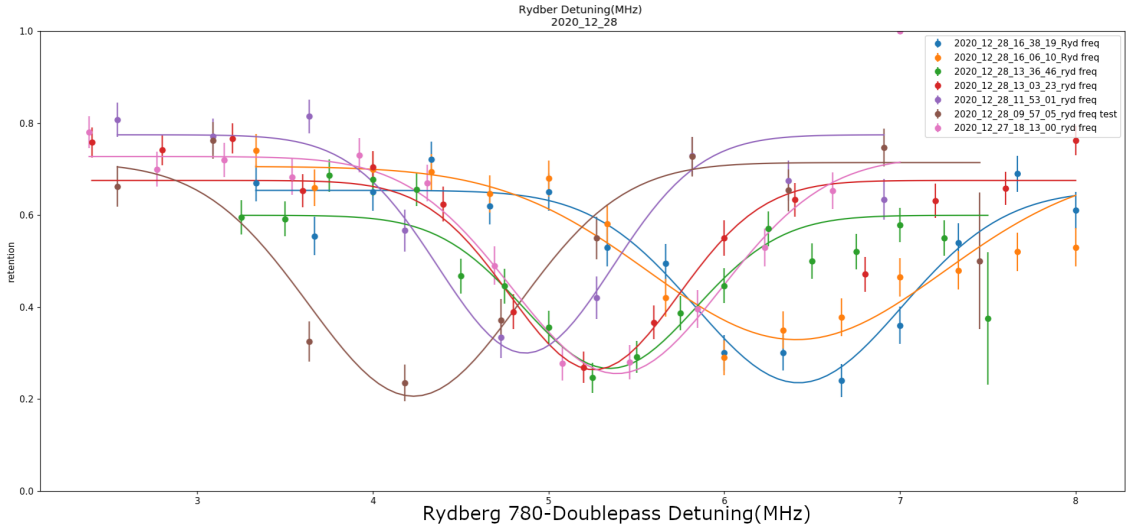

Figure 3.35: Plot showing the drift in the 780nm Rydberg frequency over the course of a single day (2020.12.28, The same day as the bottom signal in Fig.3.34!). Rapid drift of the Rydberg level detuning made progress prohibitively difficult. The cause is believed to be failure of the magnetic field coil drivers.

to regaining the performance that the apparatus originally had. We had identified and fixed multiple sources of noise that were plaguing the system, and we had seen a demonstrable improvement in the stability and dephasing when compared to the initial results immediately after the rebuild (Fig. 3.26. Had we had more time, I think it is likely that we would have been able to continue on to ensemble and W-state preparation experiments. Ultimately, however, we decided that we wanted to pursue a different project focusing on quantum communication networks and quantum nodes, which is the subject of the second section of this thesis.

Chapter 4

Quantum Network Node - Theory and Proposed Design

4.1 Introduction

An outstanding challenge in the field of quantum information is the ability to connect multiple quantum processors or sensors in a quantum network. This capability will enable distributed quantum computation and sensing, as well as secure long distance communication based on networked quantum repeater. Moreover, at any stage of the development of quantum computers, there may be a practical limitation on the achievable number of qubits in a single processing unit. Therefore, quantum networks will enable a route towards building a large scale quantum processor based on a modular architecture[48]. This chapter will analyze a quantum network architecture based on interconnected functional nodes, each containing memory and processing, as well as an interface between matter qubits and photons that mediate entanglement distribution. High rates of entanglement generation require high efficiency photon collection. This can be done by high numerical aperture (NA) lenses or by using

a resonant cavity. High NA lenses have less moving parts but are less efficient. Furthermore, the highest NA lenses[58] involve bulky custom optics with the atoms placed close to material surfaces. This is problematic when Rydberg states are used for quantum logic since these states are strongly perturbed by electric fields arising from surface charges. This renders nanophotonic devices for strong atom-photon coupling[5, 12, 45, 15] challenging to incorporate in node architectures that utilize Rydberg state operations. Two primary designs are discussed: free space collection of emitted photons with a high NA lens or mirror, and atom-photon coupling in a linear resonator. In order to achieve strong coupling without requiring a very short resonator a near-concentric geometry design is the most practical [50, 40, 34].

For our proposed scheme, we will be using the $5S_{1/2}$ and $5P_{3/2}$ levels of Rb87. Fig 4.1 shows how we intend to generate atom-photon entangled pairs. For a photon emitted by our excited atom, which occupies the $|F' = 0, m' = 0\rangle$ state, the probability that the emitted photon is circularly polarized is 2/3. This is because the m'=0 hyperfine level has no angular preference with respect to the quantization axis set by the B-field. This means that decay from that state is equally likely to be angular projection of (-1,0,1). Circularly polarized emission leaves the photon in a superposition state with equal amplitudes in σ_+ and σ_-. However, since each of the polarization states maps to exactly one hyper-fine Zeeman level in the ground state, emission of a circularly polarized photon creates a maximally entangled state between the emitted photon and the electron. Ultimately, we can use the entangled atom-photon pair to create and entangled atom-atom pair with another spatially separated quantum node. A ^{87}Rb atom is trapped inside the resonator and prepared in the state $5s_{1/2}\,|f = 1, m = 0\rangle$ by optical pumping. An excitation pulse of Rabi frequency Ω_{exc} with π polarized light transfers the atom to $5p_{3/2}\,|0, 0\rangle$ from which the atom decays back to the $5s_{1/2}$, $f = 1$ level. By angling the π polarized light at 57° with respect

to the quantization axis, we can equalize the Rabi rate for excitation of any of the three ground states m-levels. Decay into $|1,0\rangle$ results in emission of a π polarized photon that does not propagate along the resonator axis, and is not coupled through the fiber end mirror into the optical fiber. Decay into $m = \pm 1$ is accompanied by emission of a $\sigma_{\mp}$ photon which can couple into the optical fiber. Thus the observed coherent superposition is the entangled state

$$|\phi\rangle = \frac{|1,-\rangle + |-1,+\rangle}{\sqrt{2}}. \tag{4.1}$$

The relative phase of the kets follows from the Clebsch-Gordan coefficients for the transitions. The emission rates are the same into all three Zeeman sublevels, so with probability 2/3 a circularly polarized photon is emitted. The probability of the photon being coupled into the fiber is much smaller since the emission occurs into the full 4π solid angle.

Atom-photon entanglement with this choice of atomic states was demonstrated in [77] in a free space geometry, and later extended to atom-atom entanglement[29] and a loophole free Bell test[60]. Using a resonant cavity with a large cooperativity the Purcell effect[55] causes a large fraction of the photon emission to go into the cavity mode, leading to a significant increase in the useful rate of entangled photons.

A simplistic way to calculate the angular distribution of photon polarizations emitted by our atom is to assume the emitted photon is σ_+ polarized and choose our quantization axis to be the along to the k-vector of the emitted photon. Then by assuming a rotation of the initial quantization axis to match the quantization axis of our detection setup, we can use Wigner-d matrices to find the probability of that photon being σ_+ polarized for a given angle.

$$d^1_{1,1} = \sin\tfrac{\theta}{2}^2 \tag{4.2}$$

$$d^1_{1,0} = \sqrt{2}\cos[\tfrac{\theta}{2}]\sin\tfrac{\theta}{2} \tag{4.3}$$

$$d^1_{1,-1} = \cos[\tfrac{\theta}{2}]^2 \tag{4.4}$$

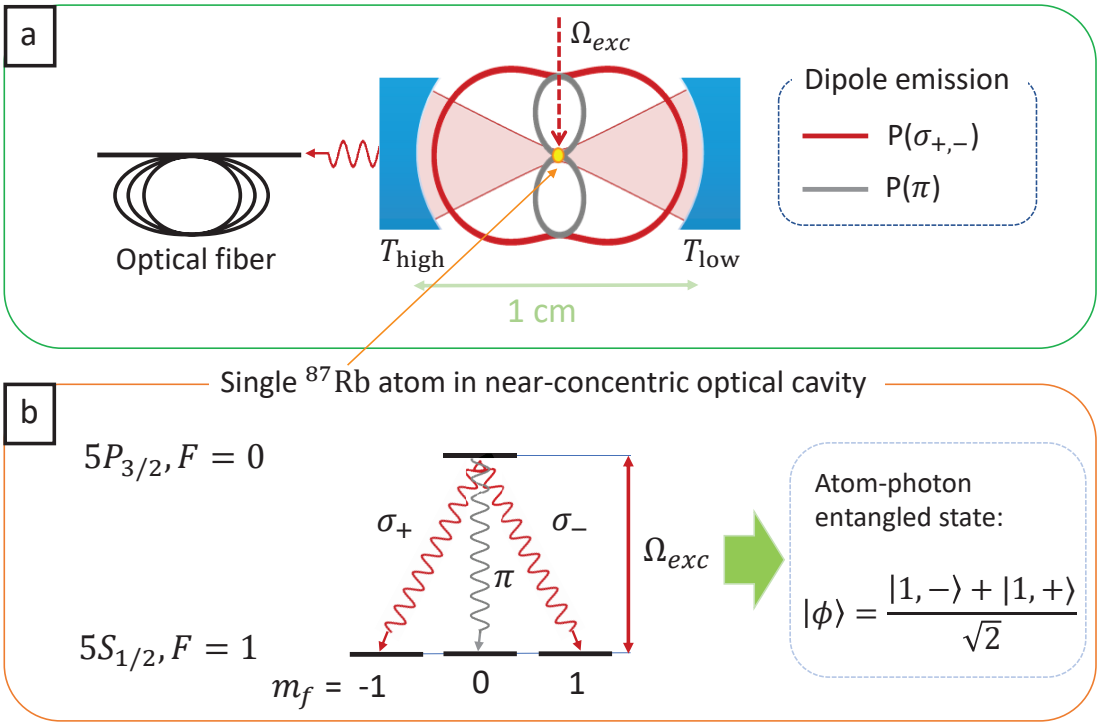

Figure 4.1: a) Geometry for atom excitation and photon retrieval using a near-concentric optical cavity with higher mirror transmission on the fiber side. b) Relevant ^{87}Rb energy levels, decay and excitation scheme, and resulting atom-photon entangled state.

This implies that for a given angle theta, the probabilities of measure either a π photon or a $\sigma_{\pm}$ photon are those given in Fig.4.2.

4.2 High Numerical Aperture Lens Case

Perhaps the simplest way to collect the photon is to use a lens. Fig 4.3 shows a basic model of this setup. If the dipole is placed at the focus of a lens, then some fraction

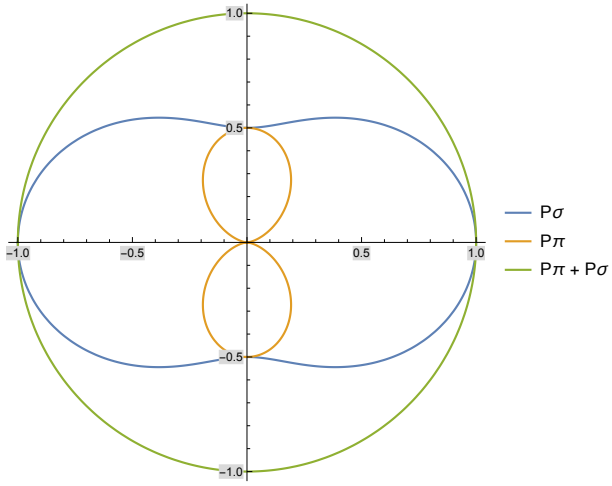

Figure 4.2: Angle dependency of dipole emission based on polarization.

of the emitted photons can be collected and subsequently coupled into a fiber to be used elsewhere. Since we would like to be able to generate entanglement as quickly as possible, the lens should collect as many of the photons as possible. The metric to describe how many photons the lens can collect is the Numerical Aperture. Numerical Aperture, or NA, is defined as

$$\mathrm{NA} = \mathrm{n} \sin \theta \tag{4.5}$$

where n is the index of refraction of the medium and θ is the maximal half-angle of the cone of light that can enter or exit the lens in the case of air/vacuum we can assume that it is 1. As an example, for a lens with an NA of 0.6 the angle of light cone captured by the lens is

$$\theta \sim \arcsin\left(\mathrm{NA}\right) \sim 37^{\circ}$$

This means that the fractional solid angle collected by a lens with a given NA is

$$\frac{\Omega}{4\pi} = \frac{\int_0^{2\pi}\int_0^{\arcsin NA}\sin\theta d\theta d\phi}{\int_0^{2\pi}\int_0^{\pi}\sin\theta d\theta d\phi} \tag{4.6}$$

For an NA of 0.6, the fractional solid angle is 0.1, or 10% of total emission angle. This means that of all the photons emitted by our atom, 10% will be collected by the lens. However depending on the NA and the placement of the lens with respect to the emission pattern of the dipole, some proportion of the photons will have an unwanted polarization. It can be seen from fig 4.3 that when the photon is emitted directly along the axis of the photon collection optics ($\theta = 0$), the probability of detecting a π polarized photon is zero. Additionally, we can see that the σ photons are slightly biased towards the collection axis. If we normalize our probabilities, we can integrate over the solid angle of our lens to find the probability that we collect a $\sigma_\pm$ photon.

$$\int_0^{2\pi}\int_0^{\arcsin NA} P_{\sigma_\pm}^2 \sin\theta d\theta d\phi \times \frac{2}{3} =\sim 0.0907 \tag{4.7}$$

$$\int_0^{2\pi}\int_0^{\arcsin NA} P_{\pi}^2 \sin\theta d\theta d\phi \times \frac{1}{3} =\sim 0.0093 \tag{4.8}$$

Where we have weighted the integrals over the collection solid angle by the proportion of each polarization that is emitted. The sum of these two probabilities adds to 0.1, which is the same as our fractional solid angle assuming an isotropic emission. Importantly, we see that of the photons collected by the lens, 90% of them are $\sigma_\pm$. As the Numerical Aperture of the collection lens increases, the proportion of photons with π-polarization increases up to an NA of 1.0, which corresponds to collecting over a half-sphere of the dipole emission. At that point, since 50% of all photons are collected, the photons have a typical polarization distribution of $\frac{1}{3}\pi$, $\frac{2}{3}\sigma$. This corresponds to a reduction in the fidelity of Bell-state measurement since a third of the collected photons will have the wrong polarization, and will not correspond to an

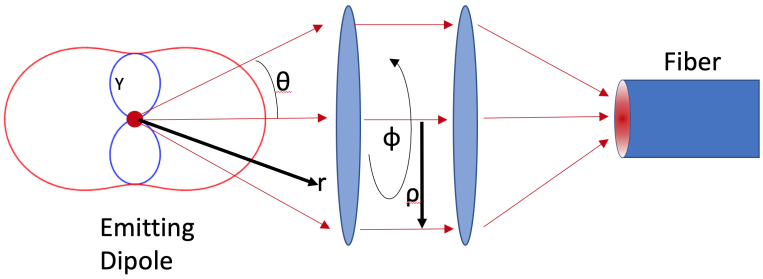

Figure 4.3: Geometry of Free-space photon collection. Light from dipole is collimated by the collection lens and subsequently coupled into the fiber. Coupling efficiency depends on the overlap of the dipole emission pattern and the Gaussian mode of the fiber.

entangled atom-photon pair. Instead of measuring the photons directly after the lens ("free-space") an alternative is to couple the light into a fiber before measurement. To do this, we need to calculate the overlap integral of the dipole emission with the Gaussian fiber mode we are trying to couple into. Again, see fig4.3 for a basic diagram. To do this, we must now consider the full description of the dipole emission, as is given in Jackson[37]. The electric field emitted by the dipole is

$$E_{D,\sigma_\pm} = A_{\sigma\pm}\frac{ie^{ikr\pm i\phi}}{r}\left(Cos[\theta]\hat{\theta} \pm i\hat{\phi}\right) \tag{4.9}$$

$$E_{\pi} = A_{\pi}\frac{ie^{ikr}}{r}\left(\sin\theta\hat{\theta}\right) \tag{4.10}$$

With normalization constants $A_{\sigma\pm}$ and A_π. The field of the fiber mode at the atoms can be assumed to be Gaussian. Additionally we can assume that the field of the fiber can be represented in a basis containing a vertical and horizontal polarization mode. In the region before the collimating lens the field can be written as:

$$E_G = A_G e^{\frac{-\rho^2}{\omega^2}}\left(\frac{\hat{x} \pm i\hat{y}}{\sqrt{2}}\right) \tag{4.11}$$

After the radiation from the dipole passes through the lens, the coordinate unit vectors are transformed into cylindrical coordinates in the following way:

$$\begin{aligned} \hat{\theta} &\rightarrow \hat{\rho} \\ \hat{r} &\rightarrow \hat{z} \\ \hat{\phi} &\rightarrow \hat{\phi} \end{aligned} \tag{4.12}$$

Based on the diagram in fig4.4 we can see that for some power emitted by the dipole in an angle $\delta\theta$, that power will be spread out over an area of $\mathrm{Cos}[\theta]\delta\rho$. Since the total power emitted over the solid angle collected by the lens must be preserved, the following must be true.

$$P_D = \int_0^{2\pi}\int_0^{\pi} E_D E_D^* \sin\theta d\theta d\phi = \int_0^{2\pi}\int_0^{\infty} E_D E_D^* \rho d\rho d\phi$$

$$E_{D,\sigma\pm}[\theta,\phi] = Eq4.9$$

$$E_{D,\sigma\pm}[\rho,\phi] = A_{\sigma\pm}\sqrt{\frac{f}{\sqrt{f^2+\rho^2}}}\frac{ie^{\pm i\phi}}{\sqrt{f^2+\rho^2}}\left(\frac{f}{\sqrt{f^2+\rho^2}}\hat{\rho} \pm i\hat{\phi}\right)$$

We can then write the overlap integral of the dipole emission and the fiber mode as:

$$Overlap = \frac{1}{2}\times\left(\int_0^{2\pi}\int_0^{\infty} E_G^* E_D \sin\theta d\rho d\phi\right)^2$$

$$E_G^* E_D = A_g A_{\sigma\pm} e^{\frac{-\rho^2}{\omega^2}}\sqrt{\frac{f}{\sqrt{f^2+\rho^2}}}\frac{-ie^{\pm i\phi}}{\sqrt{f^2+\rho^2}}\left(\frac{\frac{f}{\sqrt{f^2+\rho^2}}Cos[\phi]+i\sin\phi}{\sqrt{2}} \pm \frac{i\left(\frac{f}{\sqrt{f^2+\rho^2}}\sin\phi\right]-iCos[\phi]\right)}{\sqrt{2}}\right) \tag{4.13}$$

Figure 4.5 shows how the fiber coupling efficiency for σ photons changes as a function of the NA of the collection lens. At very high NA, despite having a larger solid-angle for collection, there are diminishing returns due to the overlap of the dipole emission and the fiber mode getting smaller. The hypothetical limit for the collection efficiency of 0.5 for a lens with an NA of 1.0 cannot practically be reached due to the fiber coupling efficiency. Additionally, at very high NA, there can be significant

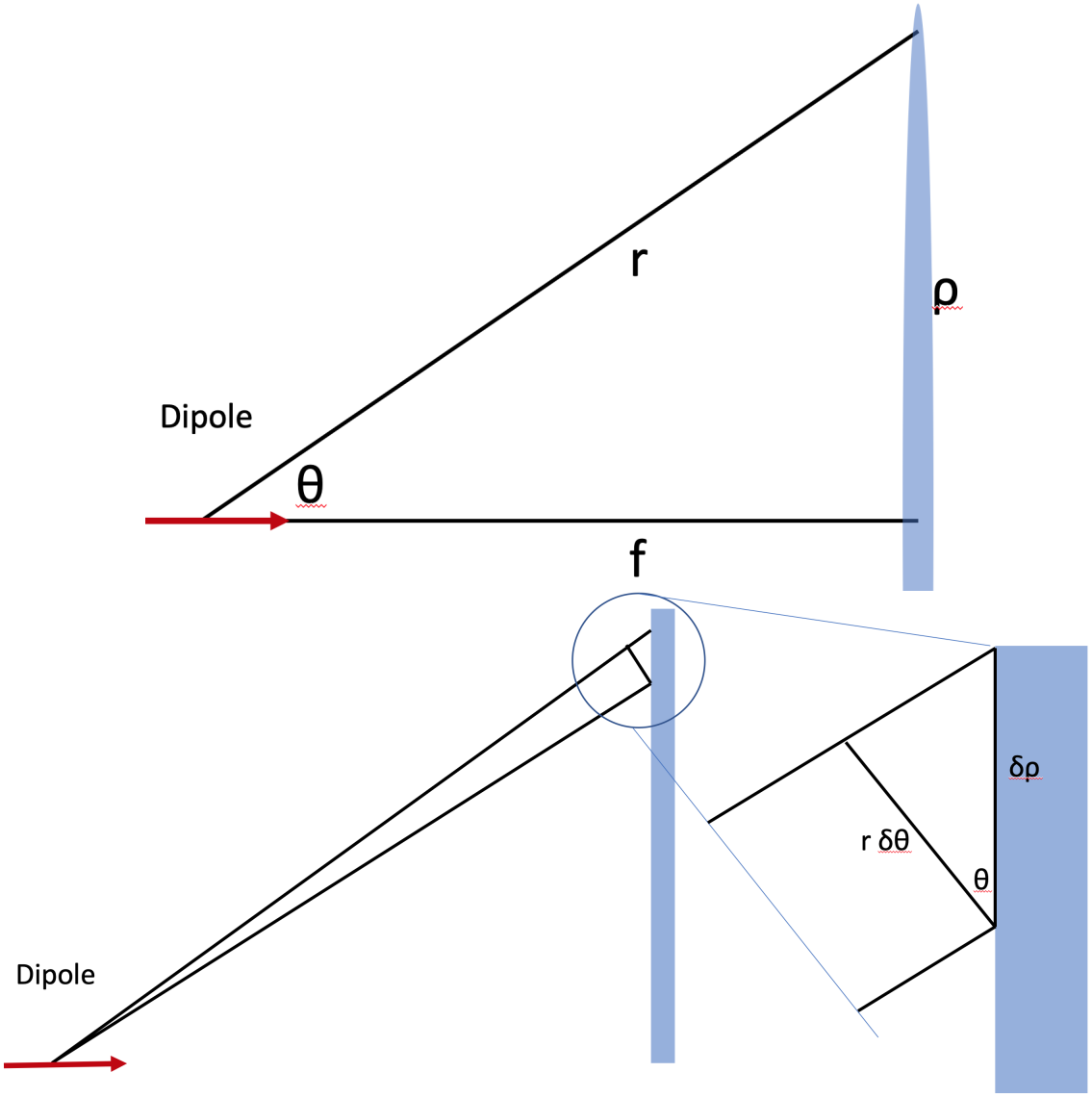

Figure 4.4: Diagram showing coordinates in the transformation of the dipole emission through the collimating lens.

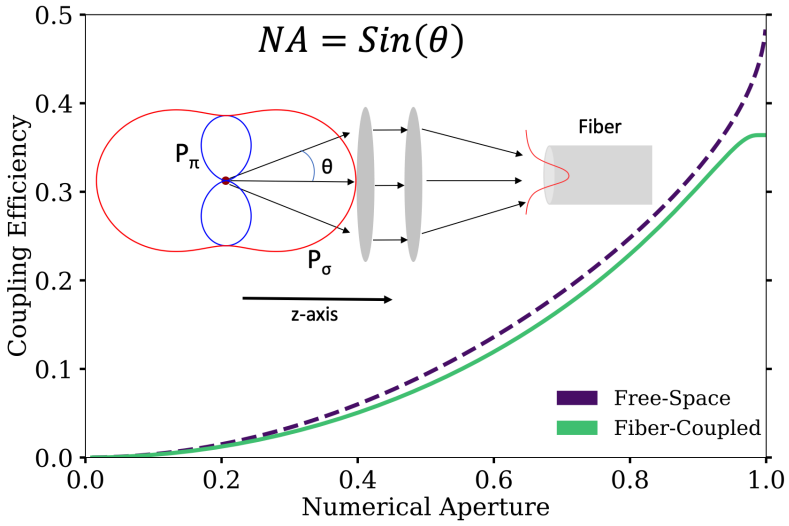

Figure 4.5: Lens coupling efficiency for $\sigma\pm$ light emitted from atom and the coupling efficiency into a fiber assuming a minimal waist size for the given NA. Purple shows the fractional collection weighted by σ light emission from the dipole. Green shows the collection efficiency into the fiber, using the integral in Eq. 4.13.

distortions of the light passing through the lens, and correcting for those spherical aberrations and chromatic shifts can be costly. This analysis also applies to the use of a parabolic mirror in place of a collection lens. The details may change, but the overall result is virtually the same.

The remaining π photons do not couple into fiber. This can be seen by calculating the overlap integral of the π polarization mode with the fiber mode through the high NA lens, but the intuition for why this is the case is that by considering the symmetry of the system. The E-Field of the π polarized light is odd with respect to ϕ so opposing parts of the π radiation must be out of phase with each other. That is to say that if we assume a boundary condition where the field at the atom is not changing in time,

then the atom must occupy a node of the outgoing EM wave. This means that when the light from the two lobes couples into the lens and goes to couple into the fiber, the opposite amplitudes cancel out, and the amplitude of the π polarized light in the fiber is zero.

Coupling of single atoms to single photons enables preparation of entangled states that can be used to establish quantum channels and networks[56]. Photon collection in free space can be done using high-NA lenses/mirrors or resonant optical cavities. Lenses with NA up to 0.92[59] have been used, however the bulk of these lenses, along with the very short working distances make then difficult to work with and perform Rydberg-mediated quantum gates.

4.3 Resonant Cavity Case

The use of a resonant optical cavity, however, can enhance the atom-photon coupling by orders of magnitude, and can result in quantum efficiencies well above 0.5 with a more compact apparatus. The key parameter that captures the ratio of coherent to dissipative interactions is the cooperativity C.

$$C = \frac{2g^2}{\kappa\gamma} \tag{4.14}$$

Where g is the vacuum Rabi freq, κ is the cavity decay rate, and γ is the atomic transition linewidth. The vacuum Rabi frequency is defined as:

$$g = d\mathcal{E}/\hbar \tag{4.15}$$

where d is the transition matrix element, and $\mathcal{E}$ is the vacuum field strength corresponding to half a photon in the cavity mode. This is written as:

$$\mathcal{E} = \left(\frac{\hbar\omega/2}{\epsilon_0 V}\right)^{1/2}. \tag{4.16}$$

Here ω is the optical transition frequency and V is the effective mode volume. For a TEM_{00} resonator mode,

$$\int_0^{2\pi}\int_0^{L}\int_0^{\infty}(e^{\frac{r^2}{\omega_0^2}}\sin(kz))^2 dr dz d\phi = \frac{\pi w_0^2 L}{4} \tag{4.17}$$

and

$$g = \frac{d}{(\pi\epsilon_0\hbar)^{1/2}}\left(\frac{2\omega}{w_0^2 L}\right)^{1/2}. \tag{4.18}$$

The cavity decay rate κ can be written as

$$\kappa = 2\pi\nu_{FWHM} = \frac{\pi c}{L\mathcal{F}}. \tag{4.19}$$

Where L is the length of the cavity and F is the cavity finesse. The atomic transition linewidth γ can be written as

$$\gamma = \frac{d^2\omega^3}{3\pi\epsilon_0\hbar c^3} \tag{4.20}$$

Combining these three definitions we get that

$$C = \frac{F\lambda^2}{\pi^3\omega_0^2} \tag{4.21}$$

This can be written in the following way to better understand the meaning of this equation

$$C = \frac{6}{\pi}\times f \times \frac{\pi\lambda^2}{\pi\omega_0^2}\times\frac{\mathcal{F}}{2\pi} \tag{4.22}$$

This can then be read as:

$$C = \text{Numerical factor}\times\text{Oscillator strength}\times\frac{\text{Scattering cross section}}{\text{Cavity mode area}}\times\text{photon round-trips} \tag{4.23}$$

Since the cooperativity is a measure of the interaction strength between an atom-cavity system, this makes it clear that what the cooperativity describes is how likely it is that an atom sitting at the center of the cavity mode will interact with a resonant photon bouncing between the mirrors of the cavity. If the mode waist is large

compared to the scattering cross section, then the photon will not be likely to hit the atom. Likewise if the photon does not make many round-trips in the cavity before it is lost, the chance of interaction is also small. We also have a factor of f from the oscillator strength, which comes from the geometrical factors associated with the specific transition we are driving. If the atom in our cavity was unpolarized, then the oscillator strength would be $\frac{1}{3}$ since only one out of the three polarization modes can interact with the atom in the $|F = 1\rangle$ state to excite the atom to the $|F' = 0\rangle$ state. However, since we are using a polarized atom in the cavity with the same polarization as the light in the cavity, the effective oscillator strength is 1, since it is effectively a two-level system.

For an atomic transition of linewidth γ being driven weakly at Rabi frequency Ω, we can write the rate of photon emission into the cavity mode and free space[21]:

$$R_{fs} = \frac{\Omega^2}{\gamma} \frac{1}{(1+2C)^2} \tag{4.24}$$

$$R_c = \frac{\Omega^2}{\gamma} \frac{2C}{(1+2C)^2} \tag{4.25}$$

However, since the total emission rate is given by:

$$R_{fs} + R_c = \frac{\Omega^2}{\gamma} \frac{1}{(1+2C)}$$

the ratio of photons emitted into the cavity mode to the total emitted photons is given by

$$\frac{R_c}{R_{fs} + R_c} = \frac{2C}{1+2C} \tag{4.26}$$

Which goes to 1 as the cooperativity increases.

Eq. 4.25 implies that the rate of emission into the cavity scales like C^{-1}. To be clear however, what this is specifically describing is the following: For each photon absorbed by the atom, it has to release a photon, which either escapes the cavity or enters the cavity mode. If it enters the cavity mode, it will eventually leave either by recoupling to the atom and being emitted out of the cavity or by transmitting through the cavity. If you count the rate of photons leaving the system, that will decrease as the cooperativity increases. In the limit that C goes to infinity, the atom will always emit into the cavity and the photon will never escape. Therefore the rate of photons leaving the system will be zero. What it is not saying is that the atom itself decays from the excited state to the ground state more slowly. In fact the opposite is true. Looking at Fig.4.6, you can see that when the cooperativity is higher, the atom decays more quickly into the cavity then it would into free space.

Additionally, we must account for the fact that as the cooperativity of the cavity increases, decay into modes which couple into the cavity are enhanced. π-polarized light from our dipole does not couple into the cavity, but both σ_+ and σ_- do. The effect of the cavity is two-fold: increasing the collection efficiency, as explained in section above, and changing the branching ratio when multiple decay channels are available. For a transition coupled to the cavity mode, the overall decay rate is enhanced by a factor of $(1 + 2C)$ due to the Purcell effect [55]. Since two of the three possible transitions couple into the cavity, $\sigma^{\pm}$ and π transitions occur with probabilities given by

$$P^+ = P^- = \frac{1+2C}{3+4C} \equiv P^\sigma, \tag{4.27}$$

$$P^\pi = \frac{1}{3+4C}. \tag{4.28}$$

Note that the total probability is normalized: $P^+ + P^- + P^\pi = 1$. In the limit that the cooperativy C is zero, each transition occurs with 1/3 probability, as expected

for transitions in free-space.

The parameter which describes the efficiency with which we can collect photons from our atom/cavity system is η_{ext}, the quantum efficiency

$$\eta_{ext} = \frac{2C}{1+2C} \times \frac{\kappa}{\kappa+\gamma} \times \frac{T1}{T1+T2+L_{RT}} \tag{4.29}$$

The first term in the quantum efficiency, $\frac{2C}{1+2C}$, is the fraction of photons emitted from the excited atoms that go into the cavity mode. As the cooperativity of the cavity increases, the probability that the photon is emitted into the cavity goes to 1. The second term, $\frac{\kappa}{\kappa+\gamma}$, which depends on the cavity and atom linewidth, is the fraction of photons in the cavity mode which escape the cavity in a well-defined traveling wave-packet. When the photon is emitted into the cavity mode by the atom, it will spend time resonating inside the cavity proportional to the inverse of the cavity decay rate. The final term takes into account loss from the cavity mirrors. T_{high} and T_{low} are the mirror transmission probabilities, with T_{high} being the mirror which the photons are collected from. L_{RT} is the round trip loss of the cavity, and can be from scattering, diffraction, absorption, etc. When the mirrors are "perfect", i.e. T_{low} and L_{RT} are 0, this term is 1. (Perfect in this context does not imply that T_{high} is also zero since that would make the coupling efficiency zero as the photon would never leave the cavity). Therefore, the quantum efficiency is a quantity which describes the fraction of atomic excitations that result in a photon emitted from the cavity such that we can couple it to a fiber and detect it. For a cavity with "perfect" mirrors, it is not difficult to show that the maximum quantum efficiency occurs when $\kappa = 2g$. For the case of a continuously addressed system, where we are exciting the atom in the cavity without pause there is a finite time associated with the photon leaving the cavity after it is emitted from the atom. In the "Fast-Cavity Regime", where $\kappa \gg \gamma$, then the efficiency with which the photon leaves the cavity is 100%, as

the photon is emitted from the cavity before it has a chance to re-couple to the atom. In this limit, each atomic excitation is associated with a photon leaving the cavity at a well-defined point in time, or that is to say there is little chance of there being 2 photons in the cavity at the same time. Fig 4.6 shows the different possible cases for an atom-cavity system.

In the "Strong-Coupling Regime" where $\gamma \gg \kappa$, the photon emitted from the atom stays in the cavity a long time, and will therefore have opportunities to re-couple to the atom and potentially be emitted outside of the cavity mode. Additionally if the cooperativity is very high, the photon will remain the cavity for a long time before being transmitted. This may increase the probability of losing the photon due to mirror losses, or in the extreme case the photon may not be emitted before a second photon enters the cavity. However, we are not exciting the atom continuously, and furthermore we are specifically exciting the atom such that only a single photon is absorbed by the atom. This way, we can guarantee that there is no chance to have two photons in the cavity at the same time, and we know that the information carried by the photon emitted from the cavity reflects the state of the atom as it is inside of the cavity. Because of this, we are effectively reducing the linewidth of the atom as it pertains to the time for the cavity to decay. γ is still virtually the same but we are forcing our system to be in the regime where the cavity decay time is much shorter than the time it takes for a second photon to decay into the cavity. In fact, the best course of action is to wait until we either detect a photon leaving the cavity, in which case we know that there is no longer a photon inside the cavity, or wait an amount of time that such that we can be almost certain that the photon has been lost and there is no significant chance that it is still in the cavity. By forcing ourselves to be in this regime, then we can exclusively look at the quantum efficiency as a metric for the performance of our cavity. This is because as long as our cavity decay rate is

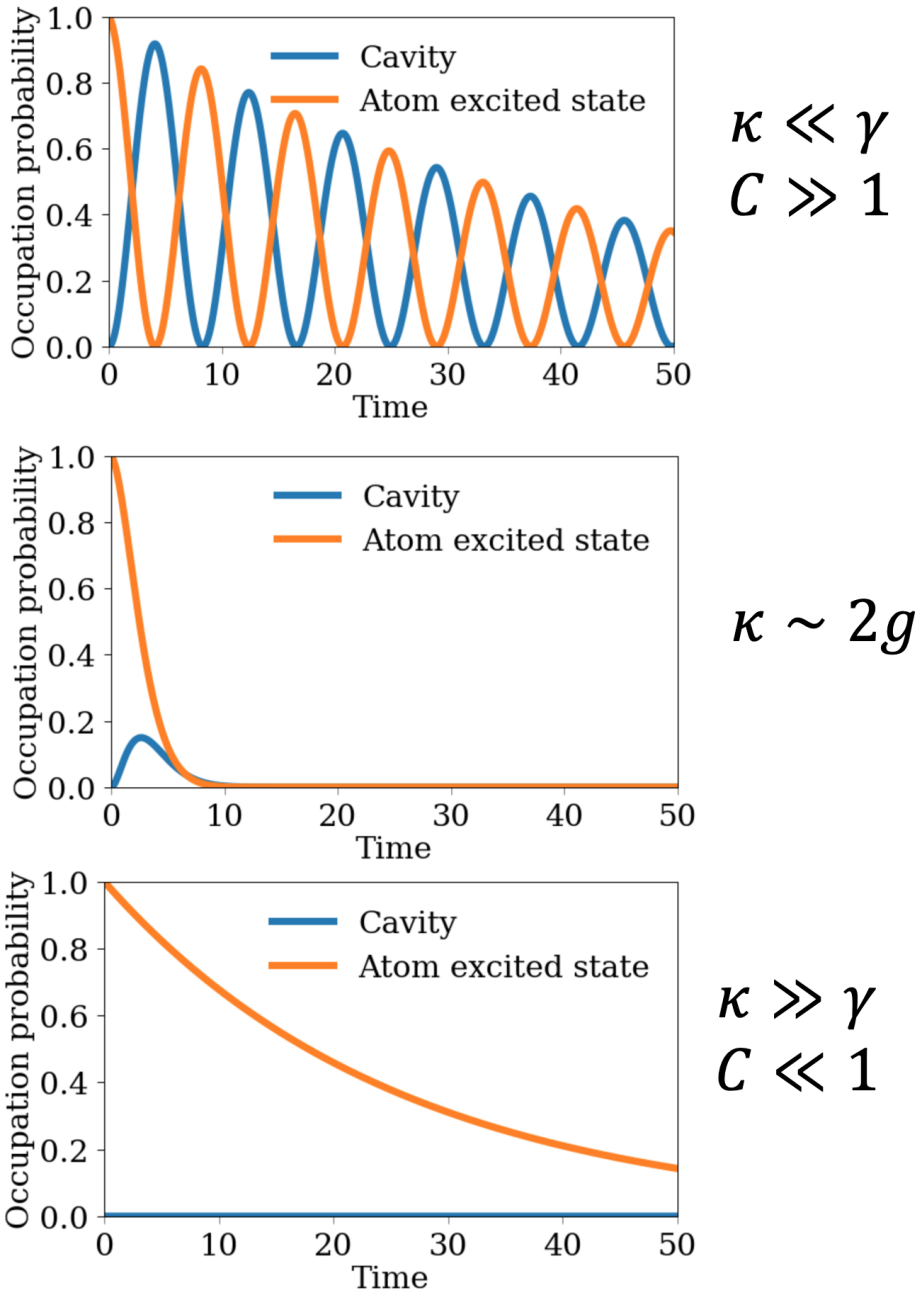

Figure 4.6: Results of solving the master equation for the Jaynes-Cummings model of an atom in a resonant cavity. Top image ("Strong-Coupling Regime") is for $\kappa \ll \gamma$ and C $\gg$ 1, middle image is $\kappa \sim 2g$, in the "optimal" case, bottom image("Weak-Coupling Regime") is $\kappa \gg \gamma$ and C $\ll$ 1. Decay rate of the atom is just the natural decay rate γ and it does not couple into the cavity.

fast compared to this maximal addressing rate, then we don't have to worry about readdressing our atom before the photon leaves the cavity.

4.3.1 Perfect Cavity Mirrors

Let's first consider the case of a two level atom in a confocal cavity where the final term in Eq. 4.29 is 1. For a confocal cavity, the waist of the cavity can be defined as:

$$\omega_{cf} = \sqrt{\frac{\lambda L}{2\pi}} \tag{4.30}$$

The maximum value of the quantum efficiency in this case is independent of the length of the cavity (Fig 4.3.1). This is because κ and g have the same scaling with the cavity length, and since the optimal quantum efficiency happens when $\kappa = 2g$, there is a single finesse which optimizes the quantum efficiency for a cavity with perfect mirrors and a given wavelength.

$$\frac{\pi c}{L F_{opt}^{CF}} = 2d\sqrt{\frac{2\pi f_{780}}{\pi \epsilon_0 \omega_0^2 L}}$$
$$\frac{\pi c}{L F_{opt}^{CF}} = \frac{4df_{780}}{L}\sqrt{\frac{\pi}{c\epsilon_0 \hbar}}$$
$$F_{opt}^{CF} = \frac{\sqrt{\pi c^3 \epsilon_0 \hbar}}{4df_{780}} \approx 12450$$

For the case of the D2 line of Rb, that finesse is ~ 12450. The maximum quantum efficiency achievable for a confocal cavity with perfect mirrors is given by the figure 4.8.

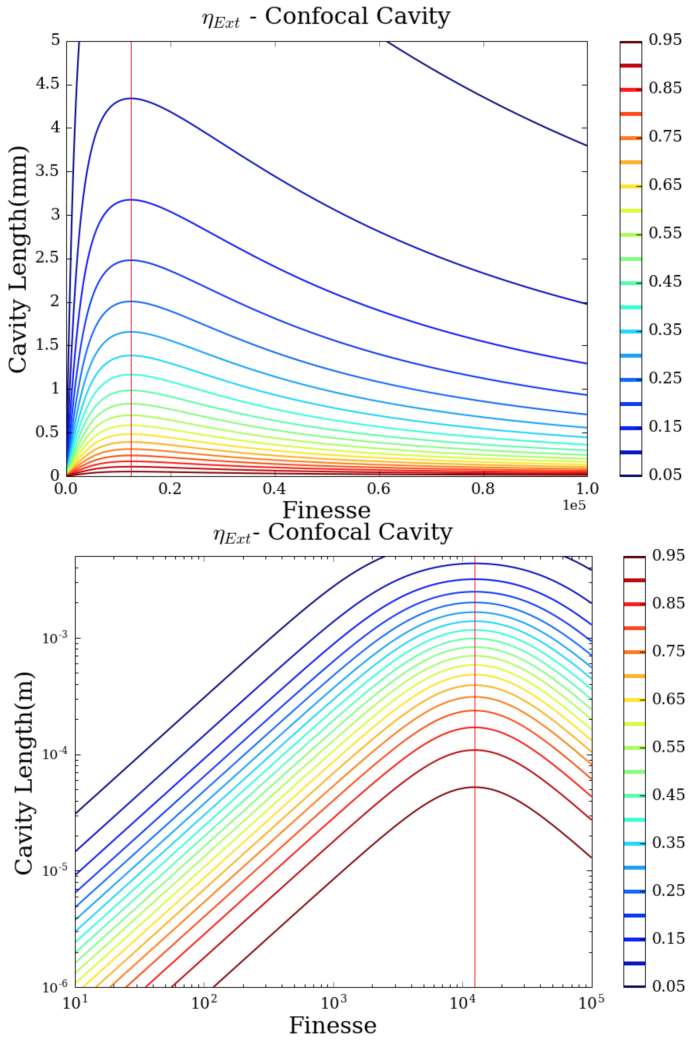

Figure 4.7: Contour plot of η_{ext} for a confocal cavity with no loss.

Using a confocal mirror configuration, where the length of the cavity is close to, but slightly less that 2 × ROC has the advantage of giving a much smaller mode waist2.9, given by:

$$\omega_{cc} = \omega_{cf} \times \left(\frac{R_m - \frac{L}{2}}{\frac{L}{2}}\right)^{\frac{1}{4}} \quad (4.31)$$

However, a truly confocal cavity is unstable (Fig.2.2), which is why the mirrors must be precisely positioned just short of the confocal configuration.

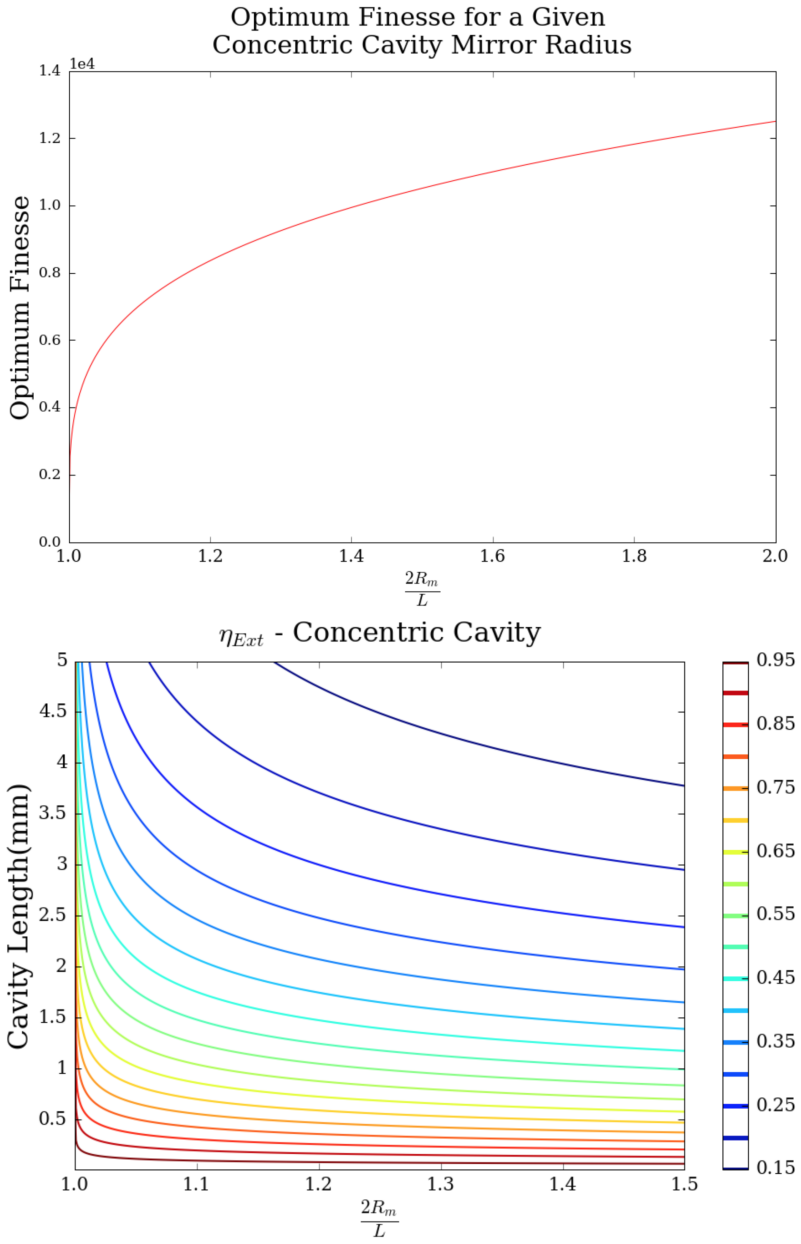

Figure 4.8: Contour plot of η_{ext} showing improvement for a mirror radius in a concentric mirror arrangement. Plot is shown assuming an optimal finesse is chosen, as shown on left, giving the maximum achievable η_{ext} for a given set of parameters.

4.3.2 Imperfect Cavity Mirrors

Imperfect mirrors reduce the finesse of the cavity. Consider a cavity of the following form shown in fig 4.1. Let's assume that a photon in the cavity has a lifetime of τ. Then we can write the probability of finding the photon in the cavity as a function of time:

$$P(t) = e^{\frac{-t}{\tau}} \tag{4.32}$$

Where at t=0, P(t) = 1, and at t=τ, P(τ) = $\frac{1}{e}$. Every time that a photon in the cavity makes a round-trip through the cavity however, it has a chance of transmitting through each mirror, given by T1 and T2, and it has a probability of being lost, given by L_{RT}. We can express this in the following way:

$$(1 - T1)(1 - T2)(1 - L_{RT}) = e^{\frac{-t_{rt}}{\tau}} \tag{4.33}$$

where t_{rt} is the time for a single round trip of the cavity. However, we can rewrite this formula in the following useful way:

$$\mathcal{F}_L = \frac{2\pi}{-\ln[g]} \tag{4.34}$$

where $g = (1 - T1)(1 - T2)(1 - L_{RT})$.

This is known as the Lorentzian finesse[36] and for cavities with high reflectivity, it converges with the Airy finesse[71].

$$\mathcal{F}_{Airy} \equiv \frac{\pi \sqrt[4]{g}}{1 - \sqrt{g}} \approx \frac{\Delta\omega_{\text{ax}}}{\Delta\omega_{\text{cav}}} = \frac{\pi}{2}\left(\arcsin\left(\frac{1 - \sqrt{g}}{2\sqrt[4]{g}}\right)\right)^{-1} \tag{4.35}$$

Where $\Delta\omega_{\text{ax}}$ is the cavity FSR and $\Delta\omega_{\text{ax}}$ is the FWHM bandwidth of the cavity. The Airy finesse is the correct formula for high finesse cavities and it will be used for further analysis, but the Loretzian Finesse gives an intuitive justification for how the finesse is defined and relates to the mirror reflectivities. For values similar to those considered in this thesis, the error is $< 0.0001\%$.

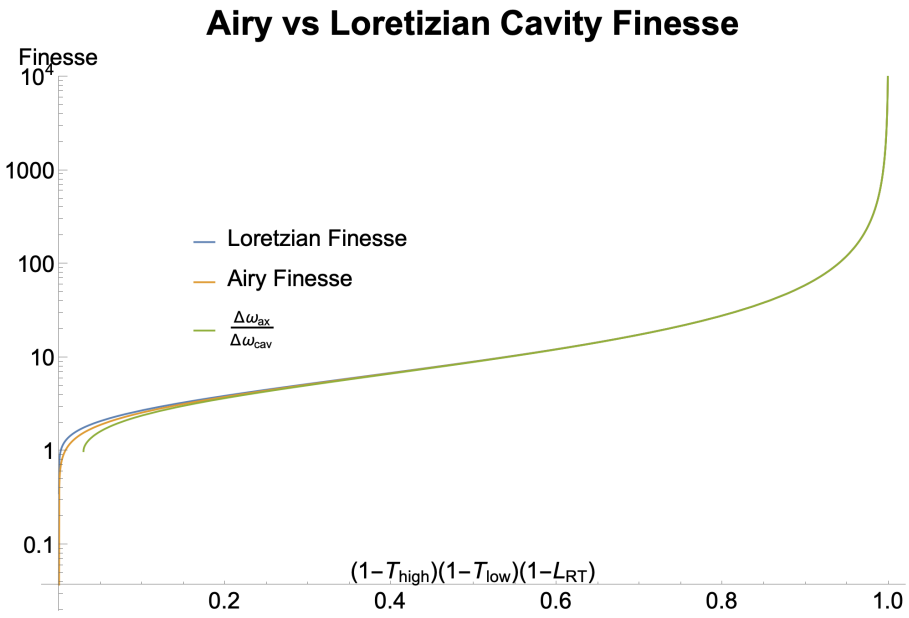

Figure 4.9: Comparison between the Airy finesse and the Lorentzian finesse.

Considering Eq 4.29, all three terms depend on the mirror losses and transmissions either through the finesse or directly. This gives a complicated dependence for η_{ext} on T_{high},T_{low} and $\mathcal{L}_{\text{high}}$. Fig4.10 shows how the different parameters depend on each other.

Eq 4.29 with a given value of η_{ext} can be solved for T_{high} giving the following lovely form:

$$T_{\text{high}} = \frac{1}{c^2\gamma\eta_{\text{ext}}}\left(4cgL(1-\eta_{\text{ext}}) - \eta_{\text{ext}}c\gamma(c\mathcal{L}_{\text{RT}} + c\mathrm{T}_{\text{low}} + \mathrm{L}\gamma)\right.$$
$$\left.\pm\sqrt{c^2L\left((2g)^4L(1-\eta_{\text{ext}})^{-}8g^2\gamma\eta_{\text{ext}}(c(\mathcal{L}_{\text{RT}} + T_{\text{low}}) + L\gamma(1+\eta_{\text{ext}}) + L\gamma^4\eta_{\text{ext}}^2\right)}\right)$$

Solving for where the radical is 0 gives the optimal value of η_{ext} for a given set of

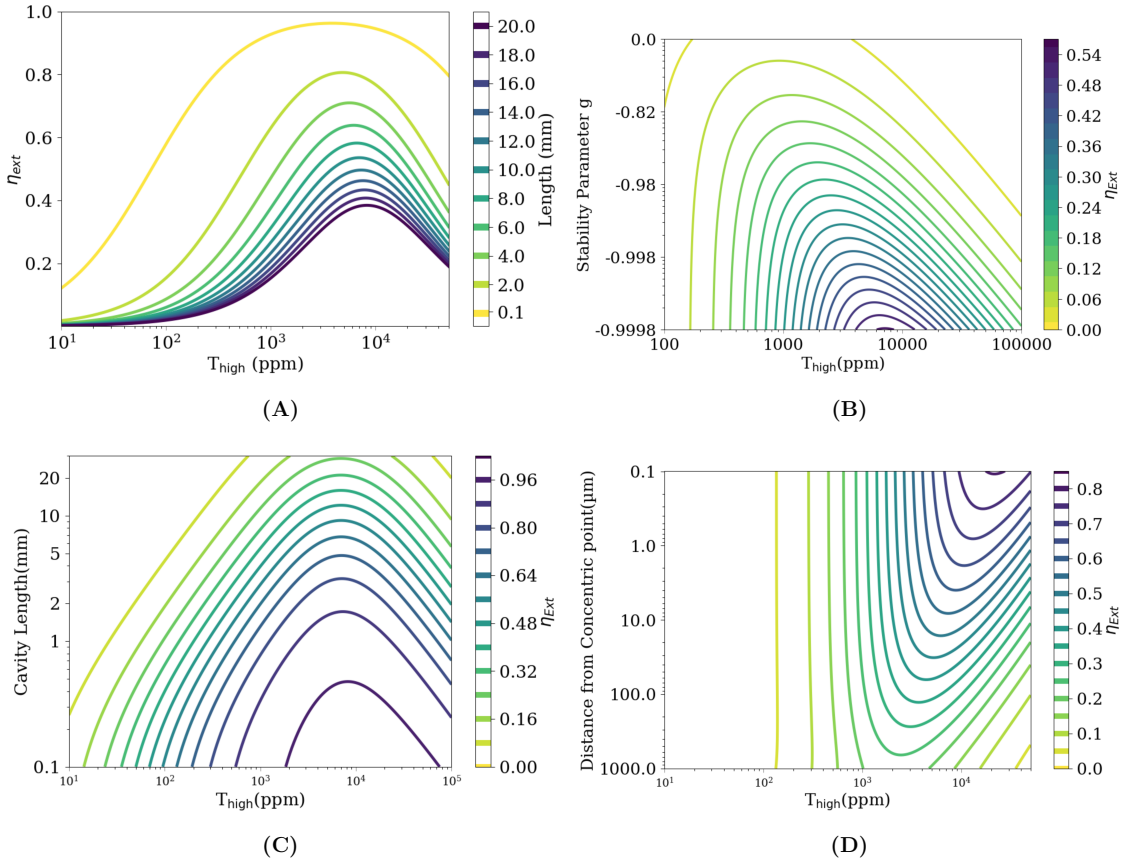

Figure 4.10: **T**hese plots assume that the high-reflectivity mirror in our asymmetric cavity has a transmission of 10ppm, and that the round trip loss L_{RT} is 40ppm.A)Cavity length required for a given η_{ext} and Mirror Quality. Critical Distance is assumed to be 10μm. **B)**η_{ext} for a given stability parameter g and Mirror Quality. Cavity length is 10mm **C)**η_{ext} for a given Cavity length L and Mirror Quality. Stability parameter is assumed to be -0.998. **D)**η_{ext} for a given distance from the confocal point and Mirror Quality. Mirror radius of curvature (ROC) is assumed to be 5mm.

cavity parameters

$$\eta_{\text{opt}} = \frac{4}{L(\gamma - 4g^2)^2}\left(4g^4 L + g^2\gamma(c(\mathcal{L}_{\text{RT}} + \text{T}_{\text{low}}) + \text{L}\gamma)\right.$$
$$\left. -\sqrt{g^4\gamma(c(\mathcal{L}_{\text{RT}} + \text{T}_{\text{low}}) + 2\text{L}\gamma)(8\text{g}^2\text{L} + \text{c}\gamma(\mathcal{L}_{\text{RT}} + \text{T}_{\text{low}}))}\right)$$

4.4 Numerical Examples using Resonant Cavities

Let's now consider some representative examples of cavities and calculate their performance when optimized to Rb87. When considering the photon generation scheme outlined in Fig. 4.1, equation 4.29 is modified to include P^σ.

$$\begin{aligned}\eta_{\text{ext}}^{(\text{Rb})} &= 2P^\sigma\eta_{\text{ext}} \\ &= \frac{4C}{3+4C}\frac{\kappa}{\kappa+\gamma}\frac{T_{\text{high}}}{T_{\text{low}} + T_{\text{high}} + \mathcal{L}_{\text{RT}}}.\end{aligned} \tag{4.36}$$

This is the equation that will be optimized with respect to the cavity parameters. First, let's consider a confocal Fiber cavity with a very short length of 150μm.

$$\begin{aligned}L &= R_m = 150\ \mu\text{m} \\ w_0 &= 4.3\ \mu\text{m}, \quad w_{\text{mirror}} = 6.1\ \mu\text{m} \\ \mathcal{F} &= 3950, T1 = 10ppm, T2 = 1540ppm, L_{RT} = 40ppm\end{aligned}$$

These parameters result in

$$\begin{aligned}(g,\kappa,\gamma)/2\pi &= 98, 253, 6.07\ \text{MHz} \\ C_{\text{confocal}} &= 12.7, \eta_{\text{ext}}^{(\text{Rb})} = 0.89.\end{aligned} \tag{4.37}$$

A short resonator length makes laser cooling inside the cavity directly from a thermal background impractical so transport from a cold atom source at least a few

mm away is required[20, 22, 27]. To allow for cooling inside the cavity we consider a longer near-concentric geometry with the following parameters

$$\begin{aligned} L &= 3.99 \text{ mm}, \quad R_m = 2 \text{ mm} \\ w_0 &= 4.0\ \mu\text{m}, \quad w_{\text{mirror}} = 125\ \mu\text{m} \\ \mathcal{F} &= 1346, T1 = 10ppm, T2 = 4620ppm, L_{RT} = 40ppm \end{aligned}$$

These parameters result in

$$\begin{aligned} (g, \kappa, \gamma)/2\pi &= 16.5, 27.9, 6.07 \text{ MHz} \\ C_{\text{near-conc}} &= 3.22, \eta_{\text{ext}} = 0.66. \end{aligned}$$

Although the cooperativity is significantly lower than for the short resonator, and this resonator is not in the strong coupling regime of $g > \kappa, \gamma$ the emission rate, and fraction of emission into the cavity mode are comparable with the short resonator case. On the other hand the quantum efficiency is much lower which will reduce the rate of entanglement production.

The mode size at the mirror in the long resonator is much larger than that of a single mode fiber. We are therefore exploring the possibility of ablating the end of a GRIN lens to form a larger concave mirror as a means of mode matching the resonator to the fiber. Cavity mirrors with a ROC less than 5mm are difficult to manufacture due to the fact that the process for making larger mirrors is distinctly different from the process for making very small mirrors. These two methods do not overlap into the range of mirrors that we feel would be ideal for the cavity that we want to build. An alternative is to buy commercially available mirrors at the smallest size we can find, and to adjust our parameters to maximize the quantum efficiency.

As an alternative, we have decided to pursue building the cavity outlined below.

$$\begin{aligned} L &= 9.99 \text{ mm}, \quad R_m = 5 \text{ mm} \\ w_0 &= 6.3\ \mu\text{m}, \quad w_{\text{mirror}} = 198.\ \mu\text{m} \\ \mathcal{F} &= 1080, T1 = 10ppm, T2 = 5730ppm, L_{RT} = 40ppm \end{aligned}$$

These parameters result in

$$\begin{aligned} (g, \kappa, \gamma)/2\pi &= 8.3, 13.8, 6.07 \text{ MHz} \\ C_{\text{near-conc}} &= 1.67, \eta_{\text{ext}} = 0.48. \end{aligned}$$

A 10mm cavity is large enough that we can fit a MOT inside the cavity, but not so small that making or purchasing mirrors is prohibitive. Furthermore we have are going to try to space the cavity 10 μm from the concentric point in order to give us a small mode volume that conveys a large advantage in photon collection efficiency. It is important to not however that as you approach the concentric point, the stability of the cavity diminishes(Fig.2.2). This means that we must consider the difficulty in maintaining a cavity so close to the concentric point. It has been demonstrated that cavities with stability parameters of -0.9996 can be operated [51], but this requires active control of the mirrors with either 3 or 5-axis piezos. An analysis of the amount of mirror tilt that can be tolerated for the above mirror design can be done in the following way [71].

$$\begin{aligned} \Delta x1 &= \frac{g_2}{1 - g_1 g_2} L\theta_1 + \frac{1}{1 - g_1 g_2} L\theta_2 \\ \Delta x2 &= \frac{1}{1 - g_1 g_2} L\theta_1 + \frac{g1}{1 - g_1 g_2} L\theta_2 \end{aligned}$$

Using this analysis you can see that for the configuration that we have suggested, we can only tolerate a tilt of a few hundred nano-meters. It is therefor likely that to

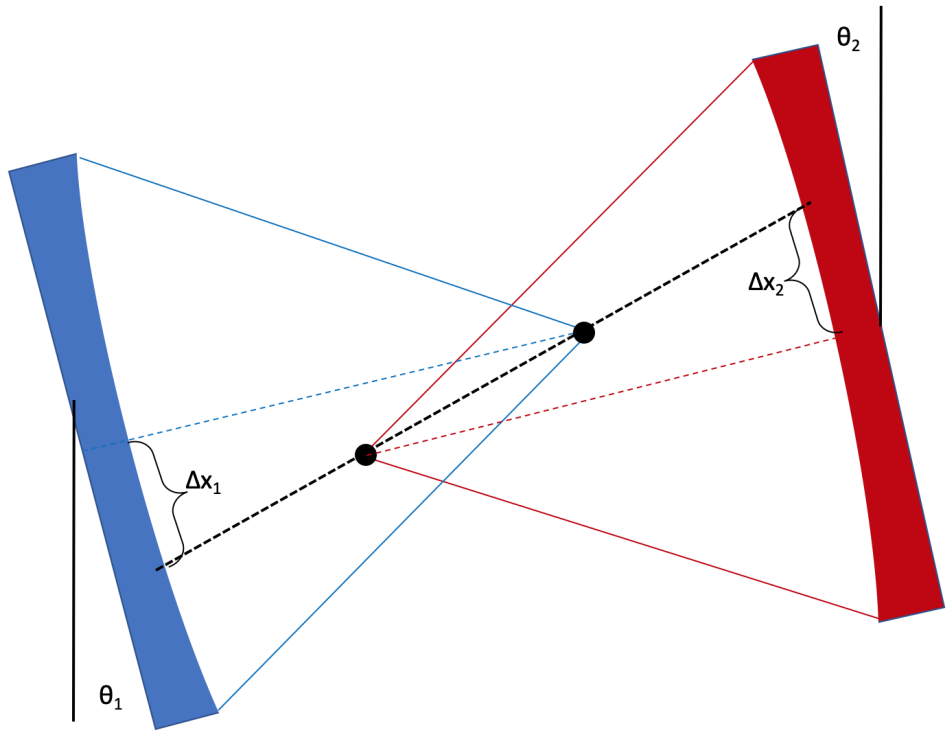

Figure 4.11: Diagram showing misalignment of an optical resonator. For small tilts the cavity axis will shift the mode in the cavity in such a way that the position of the mode on the mirrors will also change. As the cavity approaches the concentric or planar point, the sensitivity to tilt blows up. This is what is meant by these cavity configurations being less stable than a confocal configuration.

achieve a cavity of this type, we will either need to use piezos to control and align the cavity mirrors, or we will need to move further from the concentric point to a more stable mirror configuration. Comparing the collection efficiency between resonant cavities and high-NA collection optics, it is easy to see that for near-concentric cavities, the collection efficiency is far better. Fig 4.12 shows how the collection efficiency of our 10mm and 4mm cavities compare with free-space collection optics. In both the two-level case, and for our Rb87, near concentric resonant cavities outperform free-space collection optics. Since the effect of the cavity is to both increase the proportion of σ-polarized photon beyond the 2/3 fraction in free-space and also to increase the fraction σ-polarized photon emitted that couple into the cavity mode, near the concentric point where the cooperativity is high, the resonant cavities have about 3 times better collection efficiency.

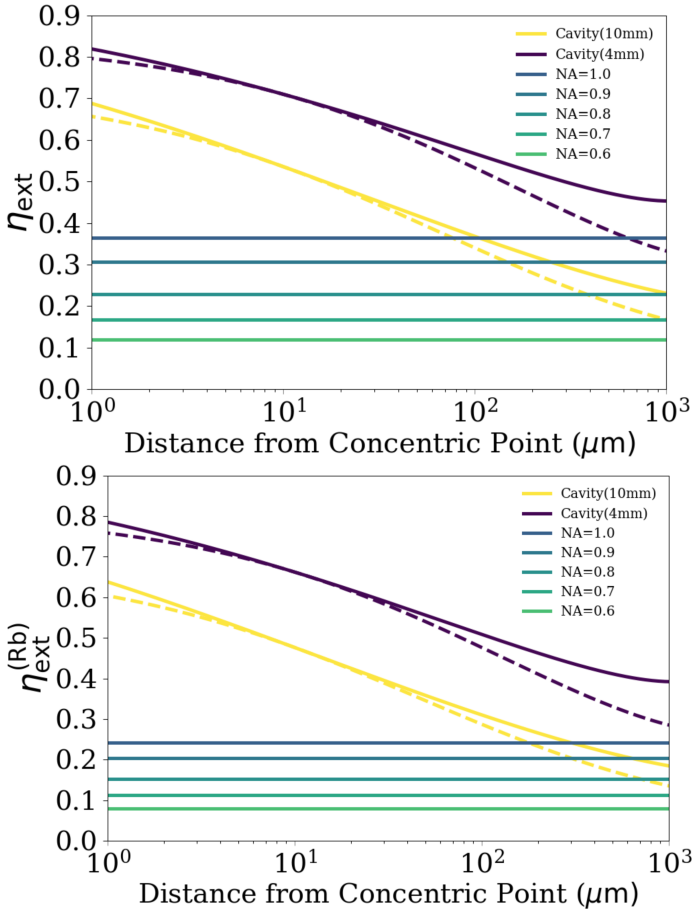

Figure 4.12: Photon collection efficiency comparison between resonant cavities with different mirror spacings and high-NA lenses. Top image is assuming a two level atom, bottom is assuming our specific excitation scheme using Rb87. The values of η_{ext} ($\eta_{\text{ext}}^{(\text{Rb})}$) for the lenses take into account both the fractional solid angle and the mode matching to the fiber. The collection efficiency of the cavities is calculated as a function of the distance from the concentric point (critical distance). The purple and yellow lines representing η_{ext} ($(\eta_{\text{ext}}^{(\text{Rb})})$) for the cavities are calculated using $T_{\text{low}} = 10\,\text{ppm}$, $\mathcal{L}_{\text{RT}} = 40\,\text{ppm}$. The solid lines are calculated with T_{high} having a value which maximizes the collection efficiency at each cavity spacing. The dashed lines show the value of η_{ext} ($\eta_{\text{ext}}^{(\text{Rb})}$) with T_{high} optimized for a cavity with a critical distance of $10\,\mu$m. We have assumed that the fiber coupling from the TEM_{00} cavity mode is unity.

4.5 Mechanisms of atom loss

4.5.1 Heating due to Addressing

A major factor that influences the rate of entanglement generation in our setup is the heating of the atoms in the trap due to addressing. If the atoms heat up enough that they can no longer be reliably addressed or that they leave the trap all together, then they must either be cooled back down, or they must be reloaded from the MOT. Because reloading from the MOT take orders of magnitude longer than the addressing of the atoms, frequent reloading will fundamentally reduce the rate of entanglement generation. Furthermore, Raman scattering in the fiber necessitates the chopping of the trap light such that the trapping light is off during the photon collection.[23, 22] On way to analyze the heating of the atoms is simulate the atom in the trap. The equation that describes the intensity of our dipole trap is:

$$I_{trap} = \frac{2P}{\pi\omega_x\omega_y} \frac{e^{\frac{2x^2}{\omega_x^2(1+\frac{z^2}{\pi\frac{\omega_x^2}{\lambda}})}} e^{\frac{2y^2}{\omega_y^2(1+\frac{z^2}{\pi\frac{\omega_y^2}{\lambda}})}}}{(1+\frac{z^2}{\pi\frac{\omega_x\omega_y}{\lambda}})} \tag{4.38}$$

For a given temperature, the distribution of atom velocities in the trapping potential can be described using a Maxwell-Boltzmann Distribution.

$$f(v_3) = (\frac{m}{2\pi k_b T})^{\frac{3}{2}} e^{-\frac{mv^2}{2k_b t}} \tag{4.39}$$

To describe the positions of atoms in the trap, we can approximate our potential as a Harmonic Oscillator potential by Taylor expanding it about the center of the trap. We can then find the natural frequencies of the trap in three dimensions and describe the positions using a normal distribution about the center of the trap with the following equation:

$$f(x_i) = \sqrt{\frac{m\omega_{x_i}^2}{2\pi k_b T}} e^{-\frac{m\omega_{x_i}^2 x_i^2}{2k_b t}} \tag{4.40}$$

Using these two distributions, we can generate an atom which has been captured by our trap. The position of the atom in the trap at that temperature is accurately described by a normal distribution because near the bottom of the trap the SHO approximation is valid. We can them simulate its dynamics classically by taking the gradient of the potential and using it to calculate the force that the atom experiences as it moves around the trap. By picking a small enough time step, we can simulate the motion of the atom in the trap by updating its position based on its current velocity, and then updating its velocity based on its current position in the trap. Doing this results in an atom that rolls around inside the trap exactly as you would expect it to in this classical context. It is assumed that the trap is conservative. This is accurate as is shown in Sec 4.5.3 The point of interest here though is to scatter photons off of the atom and observe how the energy of the atom changes over time. The simulated atom absorbs a photon subsequently re-emitted in a random direction after 27ns. By doing this many times, the total momentum of the atom will increase until the total energy of atom exceeds the trapping potential and the atom "escapes" the trap. This is the basic setup that I have simulated. Atoms are generated in the a trap with a Gaussian distribution, and a velocity given by the Maxwell-Boltzmann Velocity distribution. The motion of each atom in the trap is simulated discreetly every timestep t_s. Using a small enough timestep is important because if the accuracy of the results depends on having a small enough time step. If t_s is too large, then the errors will build up and the motion of the atoms will be un-physical. If t_s is too small, the computation time becomes long and impractical. Typically, I would simulate an atom in a trap with no addressing beam for 1 sec, and if the energy of the atom changed by more than 0.01% in that time, I would lower the time steps. For the following simulations the time step was 2ns. updating the position and velocity at each time step ts in the

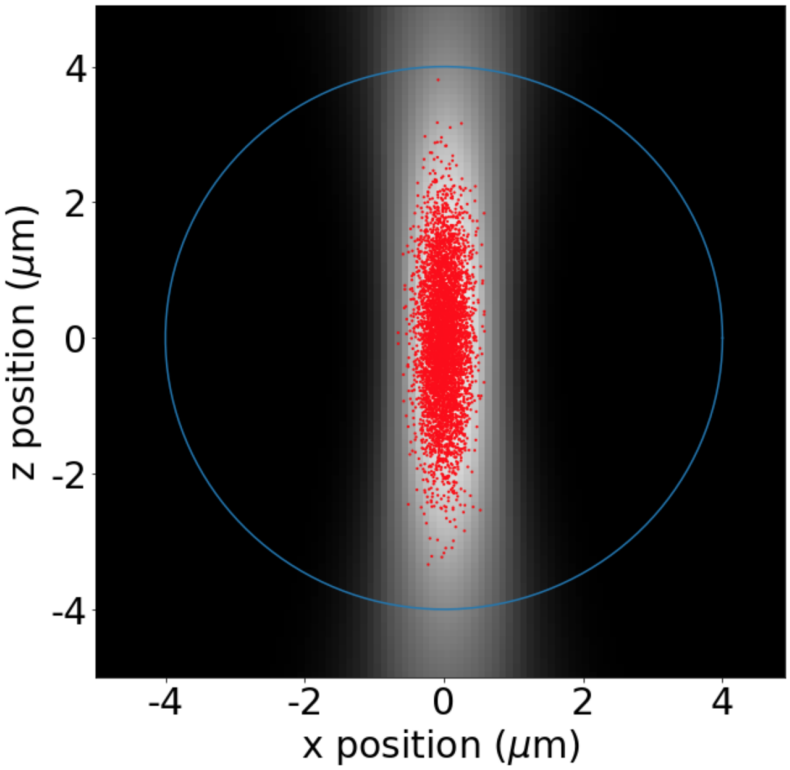

Figure 4.13: Atom distribution in a dipole trap. Red dots represent atom positions. Trap is 852nm with a depth 1mk and a waist of 1μm. Atom temperature distribution is 100μK

following way

$$x(t+ts) = x(t) + V_{\mathrm{x}}(t)t_s$$

$$y(t+ts) = y(t) + V_{\mathrm{y}}(t)t_s$$

$$z(t+ts) = z(t) + V_{\mathrm{z}}(t)t_s$$

$$V_{\mathrm{x}}(t+ts) = V_{\mathrm{x}}(t) - \frac{\nabla U(x(t+ts), y(t+ts), z(t+ts))}{m}t_s$$

$$V_{\mathrm{y}}(t+ts) = V_{\mathrm{y}}(t) - \frac{\nabla U(x(t+ts), y(t+ts), z(t+ts))}{m}t_s - a_{/rmgravity}t_s$$

$$V_{\mathrm{z}}(t+ts) = V_{\mathrm{z}}(t) - \frac{\nabla U(x(t+ts), y(t+ts), z(t+ts))}{m}t_s$$

where U(x,y,z) is the trapping potential in Joules calculated from the AC stark shift induced by the Trapping laser intensity given by Eq.4.38.

$$U(x,y,z) = \frac{-2\pi}{c}\alpha_{\mathrm{cgs}}10^{-6}I(x,y,z) \tag{4.41}$$

Every N time steps, the atom will absorb a photon, and gain momentum $\mathrm{p_{absorb}} = \frac{2\pi\hbar}{\lambda}$. This momentum will be added to the atoms momentum and changed its velocity. The photon is assumed to coming from the $\pm$x direction to simulated addressing the atom with two counter-propagating beams.

$$V_{\mathrm{x}}(t+ts) = V_{\mathrm{x}}(t) \pm \frac{p_{\mathrm{absorb}}}{m}$$

27ns later, the atom will emit a photon with the same momentum in a random direction. This emitted photon,p_{emit} therefore will in general have a component in each spacial direction. Over time the energy of the atom will increase. When the sum of the kinetic energy and potential energy is greater than 0, the atom is counted as "lost". An example atom is shown in figure 4.14. The main purpose of this simulation is to find a number of scattering events such that the chance of losing the atom is

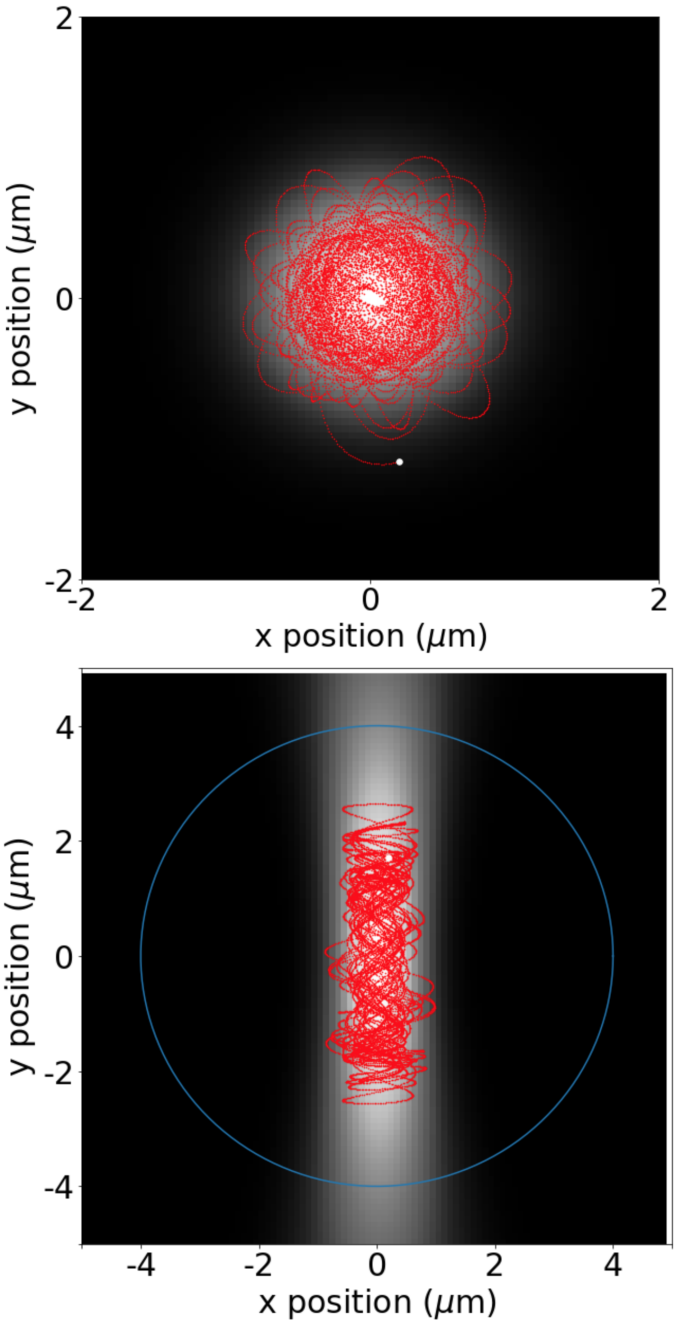

Figure 4.14: Example simulation of a single atom being addressing in a dipole trap. The number of photons scattered before loss was ∼1800. Red dots show the position of the atom over time, with the white dot showing the location of the atom when it was lost from the trap. Top image is a transverse cross section of the trap, with the contour showing the trap intensity, bottom plot is an axial cross section. Blue circle in the bottom plot represents the cavity mode of our 10mm near-concentric cavity at $\sim 4\mu m$. Trap is 852nm with a depth 1mk and a waist of 1μm. Starting temperature is 100μK.

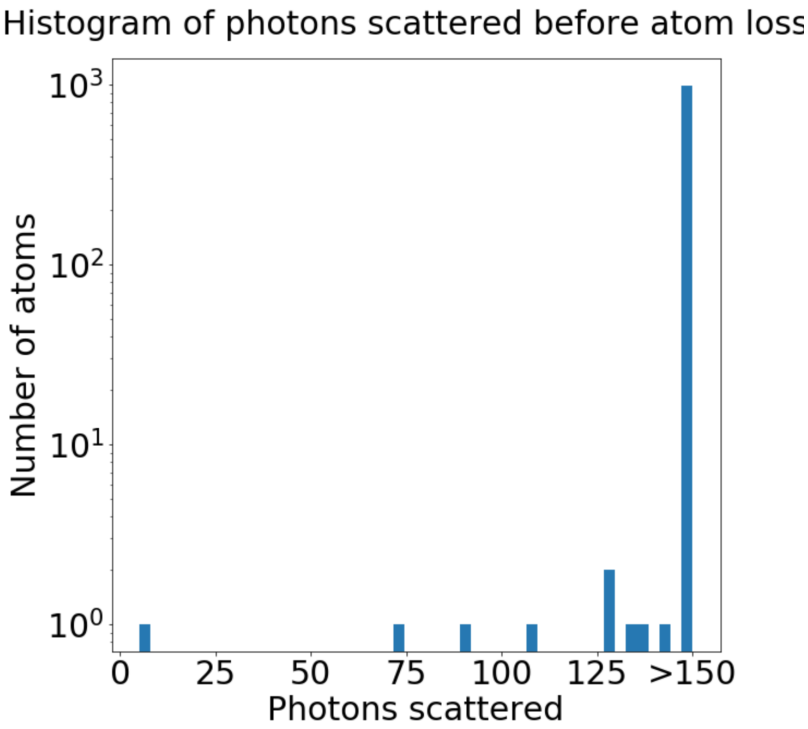

Figure 4.15: Histogram of photons scattered for 100 simulated atoms in a 1mk trap at a starting temperature of 100μk. Rb87 Atoms were addressed with 2 counter propagating 780nm beams every 3.2μs such that 150 photons were scattered. For 1000 atoms, only a single atom was lost within 50 events.

small. I did this by just simulating the atoms only for 150 scattering events, and seeing at what number of scattering events the probability of atom loss was below $\sim 0.1\%$. For a 1mK trap depth and 100μk starting temperature this was about 50 events, as shown in Fig4.15.

4.5.2 Background Collisions

Consider a stationary Rb atom (Atom A) in an empty box, along with another Rb atom (Atom B) which is flying around the box at some velocity v_B. Let us also assume that Atom B does not change velocity as it collides with the sides of the box. As the

Atom B moves around the box, each unit of time it is passing through a volume of space defined by its collisional cross-sectional area σ_{AB}, and its velocity v_B. It follows, without loss of generality, that on average the probability of a collision is proportional to the volume sampled by the atom each time step, $\sigma_{AB} \times v_B$, divided by the volume of the box, V_{Box}. This is because Atom A sits within one of these volumes, and if we assume that a random volume within the box is sampled each time step, the ratio of these areas is equal to the probability.

$$P_{collison} = \frac{\sigma_{AB} v_B}{V_{Box}} \times t$$

If we now assume that there are many atoms flying around the box, say N atoms, then the probability simply becomes $N \times P_{collison}$. For atoms as a given temperature T with a Maxwell-Boltzmann distribution, the mean magnitude of the velocity is given by:

$$\bar{v} = \sqrt{\frac{8k_bT}{\pi m}}$$

Thus, the probability of a collision occurring is:

$$P_{collison} = \sigma_{AB}\sqrt{\frac{8k_bT}{\pi m}} n_b \times t$$

where n_b is the density of atoms flying around the box. Using the Ideal Gas law, the density becomes: $n_b = \frac{P}{k_bT}$ Thus the rate of collisions is:

$$\gamma_{collison} = \frac{P_{collison}}{t} = \sigma_{AB}\sqrt{\frac{8k_bT}{\pi m}} \frac{P}{k_bT}$$
$$\gamma_{collison} = \sigma_{AB} P \sqrt{\frac{8}{\pi m k_bT}}$$

For a pressure of 10^{-9}Torr, and a temperature of 300K (room temperature), and a collisions cross-section of 2500 Angstroms^2, this gives a rate of collisions of about 24 per minute, or 0.385Hz. We expect to have a background limited lifetime of at least several seconds, ultimately we will have to measure the collision rate to know what it is.

4.5.3 Scattering from the dipole trap

Another aspect to consider for the lifetime of our atoms is the rate of scattering due to the dipole trap light. Far-off resonance traps, or FORTs, take advantage of the fact that the while the AC stark shift associated with the light scales like $\frac{1}{\Delta}$, where Δ is the detuning from resonance, the scattering rate of the light scales like $\frac{1}{\Delta^2}$. This means that if you detune the trap light enough and use enough power, you can get what is essentially a conservative potential. That is, a potential for which the path that the atom takes through the trap has no effect on its total energy. This is because the atom scatters photons from the trap light so infrequently that the atom does not heat appreciably over relatively long timescales. However, the atom does still scatter those photons, and there are other practical aspects of the trapping light that have to be considered when deciding how to configure the dipole trap.

The rate at which light will scatter from an atom is given by[46]

$$\gamma_{sc} = \frac{\frac{I}{I_s}\frac{\gamma}{2}}{1+\frac{I}{I_s}+(\frac{2\Delta}{\gamma})^2}$$

Where Δ is the detuning from resonance, γ is the decay rate, and I_s is the saturation Intensity. Additionally, the depth of the trap, caused by the AC Stark energy shift of the atomic levels in the light of the trap looks like the following:

$$\Delta E = \frac{\hbar\Omega^2}{4\Delta}$$

Where Ω is defined as $\frac{d*E}{\hbar}$ as in section 2.1.1.

Since the scaling is such that the scattering rate dies off much more quickly than the energy shift induced by the light, we can create a virtually conservative atomic trap. However, the scattering rate is not zero. The scattering rate due to the D1 line for Rb87 from an 852nm trapping potential with a depth of 1mK, we see that:

$$\gamma_{sc} = \frac{\frac{I}{I_s}\frac{\gamma}{2}}{1+\frac{I}{I_s}+(\frac{2\Delta}{\gamma})^2}$$

$$\gamma = \frac{1}{27.7ns} \quad Is = 4.484\frac{mw}{cm^2} \quad I = \frac{2c\epsilon_0 TK_b}{a_0}$$

$$\gamma_{sc} \sim 12Hz$$

Likewise for the D2 line:

$$\gamma_{sc} = \frac{\frac{I}{I_s}\frac{\gamma}{2}}{1+\frac{I}{I_s}+(\frac{2\Delta}{\gamma})^2}$$

$$\gamma = \frac{1}{26.24ns} \quad Is = 2.503\frac{mw}{cm^2} \quad I = \frac{2c\epsilon_0 TK_b}{a_0}$$

$$\gamma_{sc} \sim 15Hz$$

Other transitions also contribute, but a negligible amount. From this we can see that for our proposed trap configuration, we would be scattering $\sim$ 27 photons per second. While this may contribute to the heating, the number of photons scattered is exceedingly small compared to the thousands per second that we will be scattering during operation. If we planned on lowering the trap depth to 10mK, to combat atom loss, the scattering rate due to the trap light would increase by the same factor to $\sim$ 270/s. This is still very small compared to the number of photons scattered due to normal operation, and will likely not contribute meaningfully to the heating of the atoms between cooling cycles.

Table 4.1: Sequence of operations for acquiring atom-atom entanglement data. P_{aa} is the probability of atom-atom entanglement and P_{ap} is the probability of atom-photon entanglement

Operation	Label	Duration,t_i	Success Probability
1) Prepare MOT, load into dipole trap, shelve into $5s_{1/2}, \|1, m\rangle$	t_{load}	100 ms	1.0
2) π pulse to $5p_{3/2}, \|0, 0\rangle$	t_{π}	0.2 μs	> 0.99
3) atomic decay, record and process photon clicks	t_{det}	3 μs	$P_{aa} = \frac{1}{2}P_{ap}^2$
3.5) Cool atom to maintain localization in trap	t_{cool}	100 μs	> 0.99
4) if valid photon Bell state,μwave π pulse $\|1, 1\rangle \rightarrow \|2, 1\rangle$	t_{mw}	50 μs	> 0.99
5) atomic rotation operation, μwave + rf $\pi/2$ pulse	t_{rot}	500 μs	> 0.99
6) atomic state measurement, nondestructive	t_m	3 ms	> 0.98
7) shelve to $f = 1$	t_{reload}	1 μs	> 0.99

4.6 Rate Estimation

Using the previous analyses, we can start to construct an accurate estimate of the rate we can expect to get out of our system, and construct an experimental procedure. It has been demonstrated that excitation of the atom in the cavity can executed in $\sim$ 25ns [30]. The decay of the atom happens in similar time, and the escape of the photon from the cavity will likely happen within at most 100ns. The photon needs to travel $\sim$ 3m to the detector which takes about 10ns. This puts the total time for photon excitation and detection far below the time required to process the detection, which using arctic hardware should take $\sim$ 1-3μs. I will assume 3μs conservatively going forward.

By far the longest process we have to accommodate for our setup is loading the atoms from background into the trap. This involves preparing a MOT, loading that atom into the trap, and optically pumping the atoms into the $|\mathrm{F} = 1\rangle$ ground state. This preparation process takes upwards of $\sim$100 ms. Compared to the time it takes to address the atom, the loading/pumping process takes $\sim$ 32000 times longer. Thus

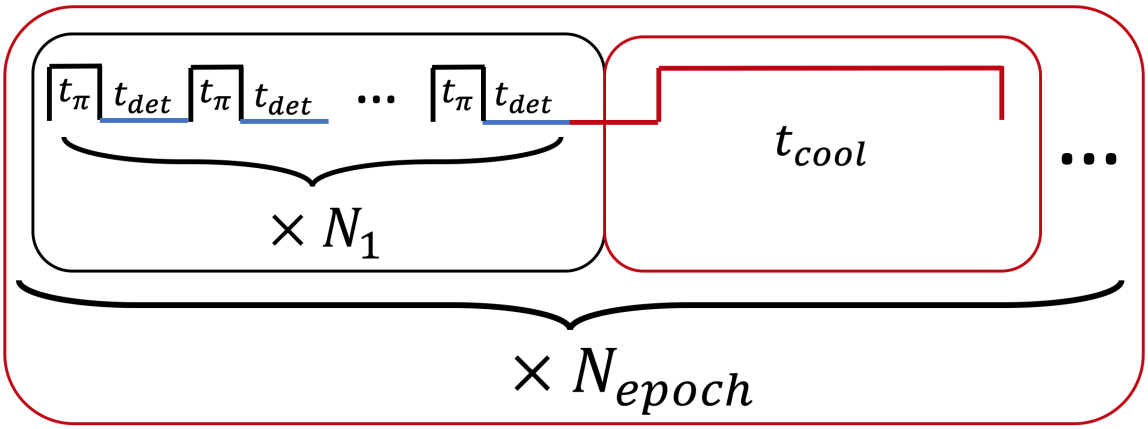

Figure 4.16: Proposed addressing sequence from Eq.4.42

it is absolutely critical that the probability of atom loss while addressing is small enough that we can minimize the number of times that we need to load the atom. As was shown in section 4.5.2, the background collision rate that we expect for our system is $\geq$0.5Hz. So we know that at least that frequently we will have to reload the atom. We would like to design our addressing sequence so that the lifetime of the atom is still background-collision limited. This will allow us to achieve the fastest possible rate. Additionally, since the success probability per cycle of entanglement generation will be small it is important to operate the experiment with as high a cycle rate as possible. The sequence of operations for acquiring a two-atom entangled state is presented in Table 4.1. Referring to the numbered steps in the table, the time to generate an entangled atom-atom pair once a trapped atom has been prepared is

$$t \simeq N_{epoch}(N_1(t_\pi + t_{det}) + t_{cool}) \tag{4.42}$$

where N_1 is the number of times that we addressing the atom between cooling cycles and N_{epoch} is the number of cycles expected to generate atom-atom entanglement. In order to satisfy the goal above, it must be true that for a given probability of loss during an addressing cycle that cumulative probability of loss across of the addressing

cycles in a given unit of time is low enough that background collisions are still the dominant mechanism of loss. The easiest way to do this is to simulate it, as the rate of loss does not scale linearly with the number of times addressed. (This is described in more detail in sec 4.5.1). For a 1mK trap depth and 1μm waist, the best strategy turns out to be to only Doppler cool the atoms each cycle. The atom temperature will only get down to about the Doppler temperature $\mathrm{T}_D = \frac{\hbar\gamma}{2k_B} \approx 146\mu K$. However it takes less than 100μs to cool the atoms to this level. We can then address the atoms $\sim$50 times each cycle while keeping the probability of loss low enough that we are still background-collision dominated. This sequence allows for $\approx N_{epoch}N_1$ entanglement attempts per second, where $N_{epoch} = \frac{1}{(N_1 Paa}$). We want to choose a value for N_1 such that the probability of loss between cooling cycles is low enough that the expected lifetime of the trapped atom is background collision limited. Assuming a background limited lifetime for the atom in the trap of $\approx$ 10s, a reasonable value for N_1 is $\sim$50, giving a probability of loss during the period of $N_1(t_\pi + t_{det})$ of $<$0.01%. Assuming a cooling time of 100μs and a trap depth 1 mK, this would give an expected lifetime of $>$2s while continuously addressing and cooling the atom. Since the overall probability of establishing entanglement follows a binomial distribution, if we make N attempts at entanglement generation, the expected number of successful events is NP_{aa} and the variance is $NP_{aa}(1-P_{aa})$ where P_{aa} is the Atom-Atom Entanglement Probability. N_{epoch} will then have a value of $\frac{1}{N_1 P_{aa}}$. As P_{aa} get larger, eventually the value of N_{epoch} will get close to 1. At this point the experiment sequence must be altered. Since cooling will have to happen after entanglement event, as P_{aa} gets larger the chance of 2 entanglement events occurring within a single addressing and cooling cycle becomes large, and the rate estimate is above what it would actually be. Therefore , the time to generate entanglement will become

$$t \simeq \frac{1}{P_{\mathrm{aa}}}(t_\pi + t_{\mathrm{det}}) + t_{\mathrm{cool}} \sim 160\mu\mathrm{s}, \tag{4.43}$$

, , where the rate is now limited by the cooling time. Even with a P_{aa} of 1, the maximum rate achievable is $1/t_{\text{cool}} \sim 10000s^{(} - 1)$.

Estimate of Atom-Atom Entanglement Probability

As stated in Table 4.1 , the probability of generating atom-atom entanglement between two distinct nodes is

$$P_{aa} = \frac{1}{2} P_{ap}^2 \tag{4.44}$$

$$P_{ap} = 2 * P^{\sigma} \eta_{\text{ext}} \eta_{\text{det}} \tag{4.45}$$

where $2P^{\sigma}\eta_{\text{ext}}$ is the probability that the atom cavity system will generate a suitable photon for producing a Bell-state. $2P^{\sigma}$ is the probability that the atom emits a photon with the correct polarization. By using a resonant cavity with a large cooperativity the Purcell effect[55] causes a large fraction of the photon emission to go into the cavity mode, leading to a significant increase in the useful rate of entangled photons (Eq.4.27). For the scheme that are using this factor is ~ 0.89. η_{ext} is the probability that the photon is emitted into the cavity mode leaves the cavity in a well-defined wave-packet that has a chance to be detected. η_{det} is the probability that a generated photon will be detected, and it depends on the probability the photon couples to the fiber, the probability that the photon is not lost in the fiber, and the probability that the SPCM successfully detects the photon. The factor of $\frac{1}{2}$ accounts for the fact that only half of the generated Bell-states can be detected and identified. Note that in Eq. 4.45 we have assumed P_{ap} to be the same for both nodes.

We can make an initial estimate of P_{aa} using $\eta_{\text{ext}} = 0.48$: the quantum efficiency of our 10mm near-concentric cavity. We are assuming that since the mode in the cavity is the TEM_{00} Gaussian mode, that coupling into a fiber should have an efficiency close to unity. The quantum efficiency of our SPCM at 780 nm is $\sim$0.7, and the attenuation losses in the fiber can be described by $e^{\frac{-L}{\lambda_{att}}}$ where L is in km and λ_{att} for 780nm is

1.091 for a typical 780nm fiber. Thus for a 1 km fiber, the attenuation is ~ 0.4. We can then estimate $\eta_{\text{det}} = 0.7 \times 0.4$. This gives a value for $P_{aa} = 8.9 \times 10^{-3}$. Using the values in Table 4.1 and our estimated value of P_{aa}, we expect a single successful event on average every $\frac{1}{P_{aa}} \approx 112$ attempts with variance $1 - P_{aa} \approx 1$. This gives us a value for N_{epoch} of ~ 2.3, and an expected time to generate atom-atom entanglement of

$$t \simeq 2.3 \times (50(t_\pi + t_{det}) + t_{cool}) \sim 0.59\text{ms} \tag{4.46}$$

This would give an entanglement generation rate of $\sim 1700\ \text{s}^{-1}$ at a node separation of 1km.

These rates could be increased by several times, without improving the optical efficiency, by reducing the electronic latency. The estimate of $t_{det} = 3\ \mu$s is conservative. The experiment in Ref. [73] used an ARTIQ based control system to achieve $t_{det} = 1\ \mu$s. Using this less conservative value for t_{det} gives an entanglement generation rate of $\sim 2700\ \text{s}^{-1}$ Additionally by increasing the trap depth, the likely hood of the atom being lost during the addressing sequence will be reduced. With a trap depth of 3mK, we could address the atom 300 times every addressing cycle instead of 50. This would increase our entanglement generation rate from $\sim 1700\ \text{s}^{-1}$ to $\sim 2500\ \text{s}^{-1}$.

These estimates are based on some assumptions. The most critical are that we can address the atom without losing the atom to a background collision, heating it out of the trap, or depumping to $5s_{1/2}, f = 2$. We have taken into account the probability of loss due to heating out of the trap by assuming that we need to cool the atoms every 50 photon emissions or so, resulting in a loss rate that should be 2s. Each time the atom is lost we would need to reload the trap resulting in $\sim$ 100ms of lost time, and a reduction in rate of $\sim$5%. We have assumed a Doppler cooling time of 100μs, which has been demonstrated in similar experiments.[61] The rates for these

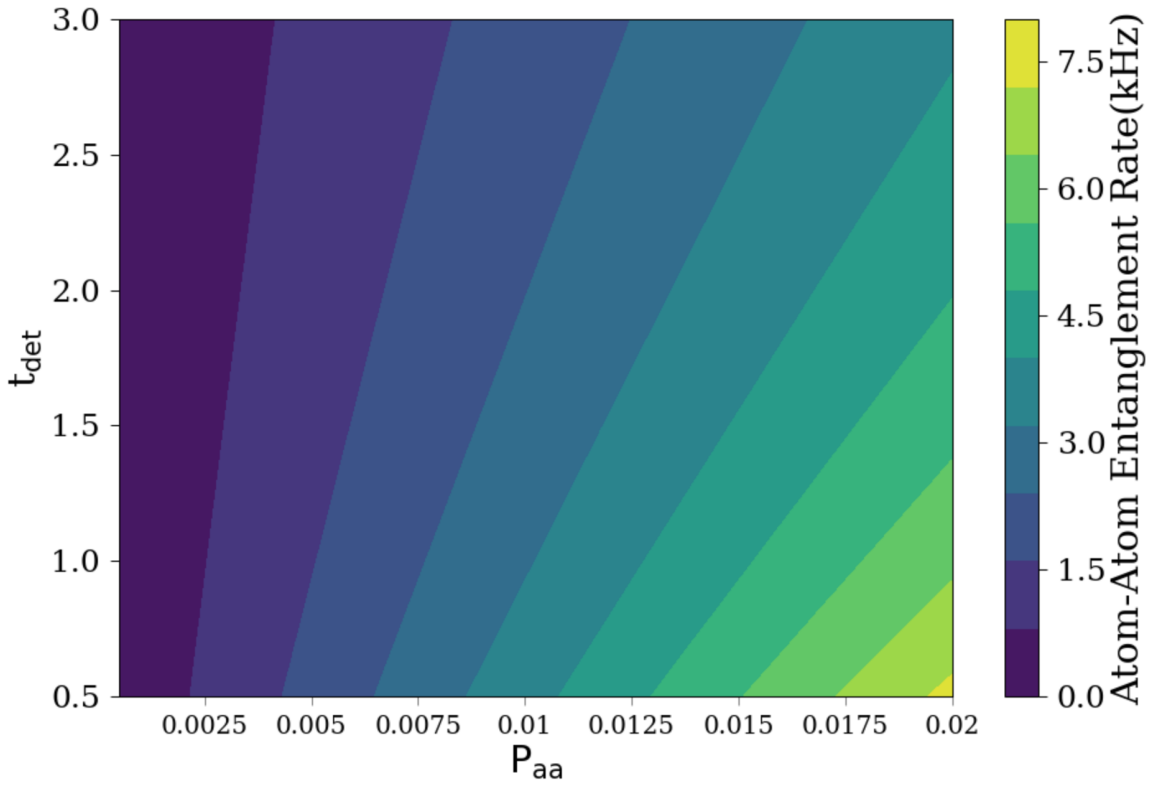

Figure 4.17: Entanglement generation rate for a given value of t_{det} and P_{aa} assuming a 1km fiber.

loss processes will have to be characterized and correction operations either inserted at a regular interval or performed after a fixed number of failed attempts. Leakage to $5s_{1/2}, f = 2$ can be rapidly corrected by shelving to $f = 1$ in less than 1 μs using light resonant with $5s_{1/2}, f = 2 \rightarrow 5p_{3/2}, f = 1$.

Achieving entanglement rates of several kHz will require $P_{aa} > 0.01$ and repetition rates of several 100 kHz, as can be seen in Fig. 4.17.

Achieving a $P_{aa} > 0.01$ will require either positioning the cavity closer to the confocal point, or using a smaller cavity. While a smaller cavity would provide a significant increase in the quantum efficiency, having a very small cavity that neces-

sitates transporting the atoms into the cavity mode may be counterproductive as the time required to do so is long and there is a large increase in complexity. Our goal is to have a cavity that is large enough that a MOT can be formed inside the cavity, and no transport is required. Moving the cavity closer to the confocal point is viable option. It has been demonstrated that a cavity in a near confocal configuration can be maintained with a stability parameter s of -0.99996 [51] using active feedback. Using a similar spacing for our cavity would decrease our mode volume by a factor of ~ 7, and ultimately increase our value for P_{aa} by a factor of ~ 2 to $5.0 * 10^{-3}$, and our rate to $\sim$400Hz. Maintaining this spacing with active feedback requires not only maintaining the spacing of the mirrors precisely, but also the transverse alignment must be actively controlled. As was shown in [51], the FWHM of their cavity transmission with respect to the transverse alignment of the mirrors was only 59nm.

4.7 Entanglement Verification and Quantum State Tomography

To generate an entangled atom pair, we need to do a Bell-state measurement on the photons to project them into a maximally entangled state. The measurement scheme is based off of the Hong-Ou-Mandel effect[32]. When photons hit the detectors, bunching or anti-bunching of the photons allows for the identification of Bell states. A coincidence in detectors H1V1 or H2V2 indicates a projection of the photons onto the symmetric Bell state $\frac{1}{\sqrt{2}} |H\rangle |V\rangle + |V\rangle |H\rangle$. Likewise a coincidence of detectors H1V2 or H2V1 indicates a projection of the photons onto the anti-symmetric Bell state $\frac{1}{\sqrt{2}} |H\rangle |V\rangle - |V\rangle |H\rangle$.The other 2 bell states cannot be determined, and this is the origin of the $\frac{1}{2}$ factor in Eq 4.45. In general this process requires that the photons arriving at the detector are spectrally, spatially, and temporally indistinguishable.

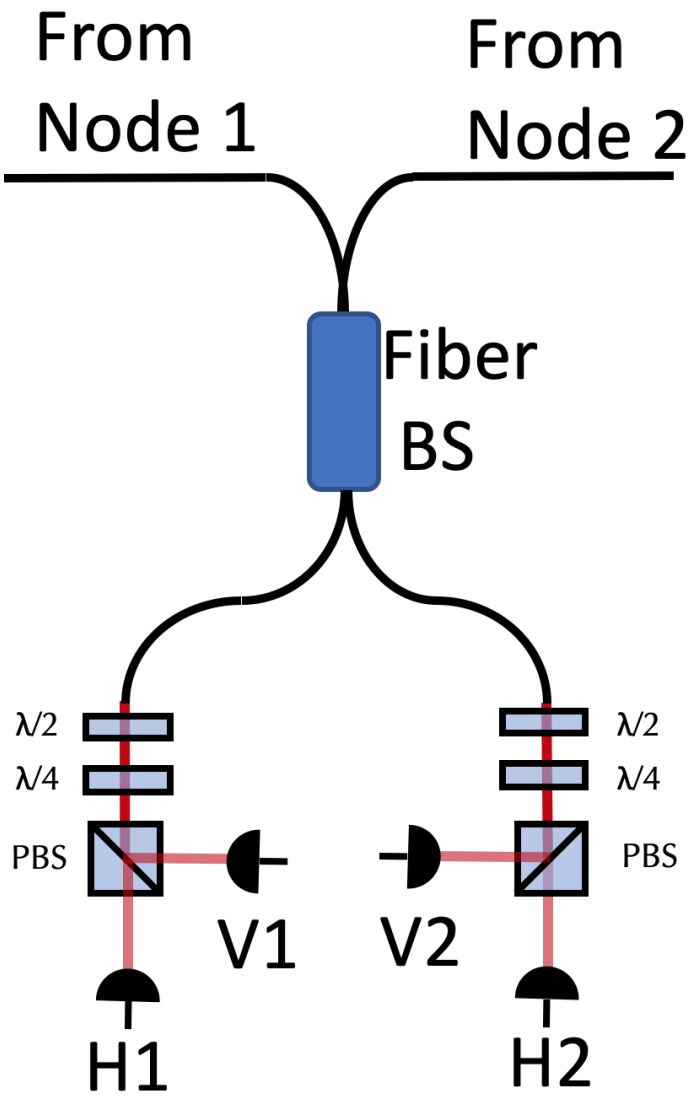

Figure 4.18: Apparatus used to do interferometric Bell state analysis. Photons from the spatially separated nodes. Are projected into a maximally entangled bell state at the beam-splitters, and thus transfer the entanglement from the atom-photon pairs to a bipartite state between atoms at each of the nodes.

This is a difficult engineering challenge; however it has been demonstrated with high fidelity[28]. Once we have generated an entangled Atom-Atom pair, we will map the atomic states to our measurement basis (Table 4.1). Using the procedure outlined in[25], We will map the atom from the $|\mathrm{F}=1,\mathrm{m_F}=-1\rangle$,$|\mathrm{F}=1,\mathrm{m_F}=1\rangle$ basis to the $|\mathrm{F}=1,\mathrm{m_F}=-1\rangle$,$|\mathrm{F}=2,\mathrm{m_F}=1\rangle$ basis through a magnetic dipole microwave transition. Once in this new measurement basis, we can do state tomography and non-destructive readout. Basis rotation is done via a two-photon MW-RF transition. Non-Destructive readout occurs using the $|\mathrm{F}=2\rangle$ and $|\mathrm{F}'=3\rangle$ cycling transition.[38]

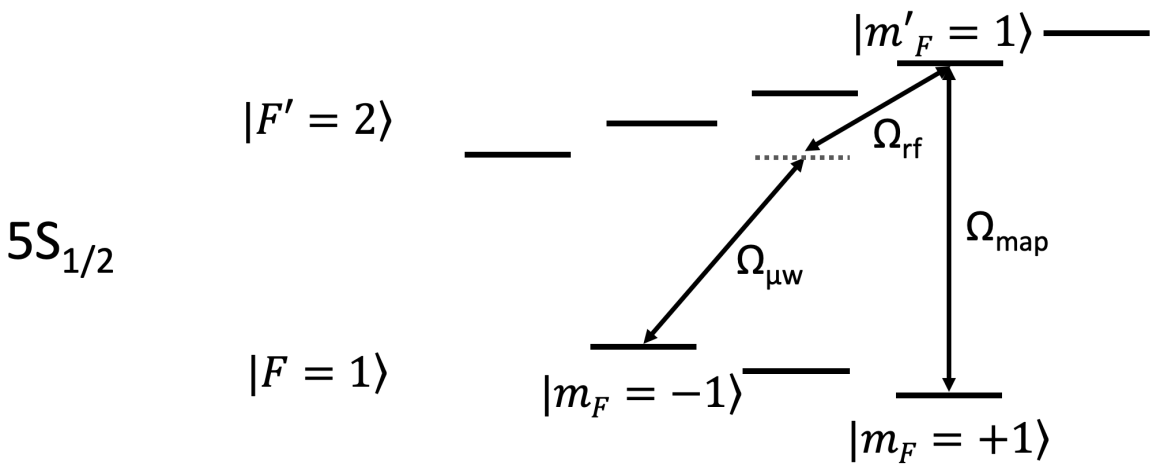

Figure 4.19: Diagram showing our proposed Mapping and Measurement Scheme. Bias Magnetic field is 3.23 G such that the first order differential Zeeman shift between the $|m'_{\mathrm{F}}=1\rangle$ and $|m_{\mathrm{F}}=-1\rangle$ states is zero.[25]

Verification of Entanglement can be done in many ways. One way is to perform tomography on the combined state and extract the entanglement fidelity from the reconstructed density matrix[73]. The requirements for tomography of a bipartite state are nine distinct pairs of analysis pulse settings and four state measurements for each

pair of settings giving a total of 36 distinct measurements. Photonic measurements in a polarization basis are implemented by rotating quarter- and half-wave plates. Atomic qubit measurements are implemented with rotations that can be driven by microwave pulses as discussed above.[25, 75]. Reduction in BSM fidelity should be predominately from dark counts. The probability of a false positive due to dark counts is

$$2 * P_{\mathrm{dc}} * \eta_{\mathrm{ext}}^{(\mathrm{Rb})} * \eta_{\mathrm{det}} * \left(1 - \eta_{\mathrm{ext}}^{(\mathrm{Rb})} * \eta_{\mathrm{det}}\right) + O(P_{\mathrm{dc}}^2) \tag{4.47}$$

Where P_{dc} is the probability of a dark count occurring in a single detector during the detection window. Given our estimated dark count rate of 50Hz, and a detection window of 100ns, P_{dc} should have a value of $\sim 5 \times 10^{-6}$. Given our estimated probability of a true positive, $P_{aa} = 0.89 \times 10^{(} - 3)$, the probability of obtaining an entangled state after measuring one is 0.999. This estimate assumes that that the spatial and temporal overlap of the emitted photons is near unity. There is a possibility of off-resonant coupling to $5p_{3/2}\,|F = 1\rangle$. This would disrupt the entanglement generation and open a decay channel to the $5s_{1/2}\,|F = 2\rangle$ state which would require re-shelving to $5s_{1/2}\,|F = 1\rangle$. The time to re-shelve the atoms, t_{reload} is short,$\sim 1\,\mu$s. The probability of off-resonantly coupling is exceedingly small so the effect on the entanglement generation rate should be negligible. Additionally the photons emitted due to off-resonant coupling will not be resonant to the cavity mode and thus will not affect the fidelity of the bell state measurement.

4.8 Proposed designs

Currently we are in the process of designing and developing the techniques that we need to construct an apparatus that performs in the way described in the above section. Fig 4.20 shows our designs for the first version of our network node. A 1" anodized aluminum breadboard supports a vacuum system consisting of and upper

and lower section. Both sections will be kept under vacuum by Gamma Vacuum 10ST TiTan 10L/s Ion pumps. The lower section consists of a 5-way cross supporting the ion pump, Valve for turbo-pump connection, electrical feed-throughs, and a custom fiber-feed-through. The upper section is separated from the lower section by a differential pumping tube. The upper section also has a flange/valve for turbo pump connection, as well as a vale/bellows section for an ampule of Rb atoms for the experiment. The main cell, which is shown in more detail in figure 4.21, is a custom "pancake cell" design which allows for the compact chip structure to be supported by groves within the cell. The chip is equidistant between two glass windows which allow High-NA objectives to be positioned to collect atomic fluorescence. An example of these lenses can be seen at the bottom of the lower picture in Fig 4.21. The initial version of the quantum node will use a High-NA parabolic mirror to collect photons. This decision is intended to give us an opportunity to perfect our construction/alignment methods, and to also give us an opportunity to practice using the apparatus while we construct and align the cavity for the second version. Fig 4.21 shows this parabolic mirror design. As of the time of this work, construction is underway.

4.9 Looking forward

After demonstrating atom-atom entanglement generation with our proposed design, the next goal is to build a dual species version that uses arrays of atoms within the mode of the cavity. The benefit of such a design is that one type of atom can be used for communication and atom-photon coupling and another atom for memory and processing. The two types of atoms can then be coupled via interspecies Rydberg gates[79], while the optical wavelengths used to couple to communication qubits do not perturb the memory atoms. In a two-species architecture the communication qubits can also be used for non-destructive state measurements without crosstalk

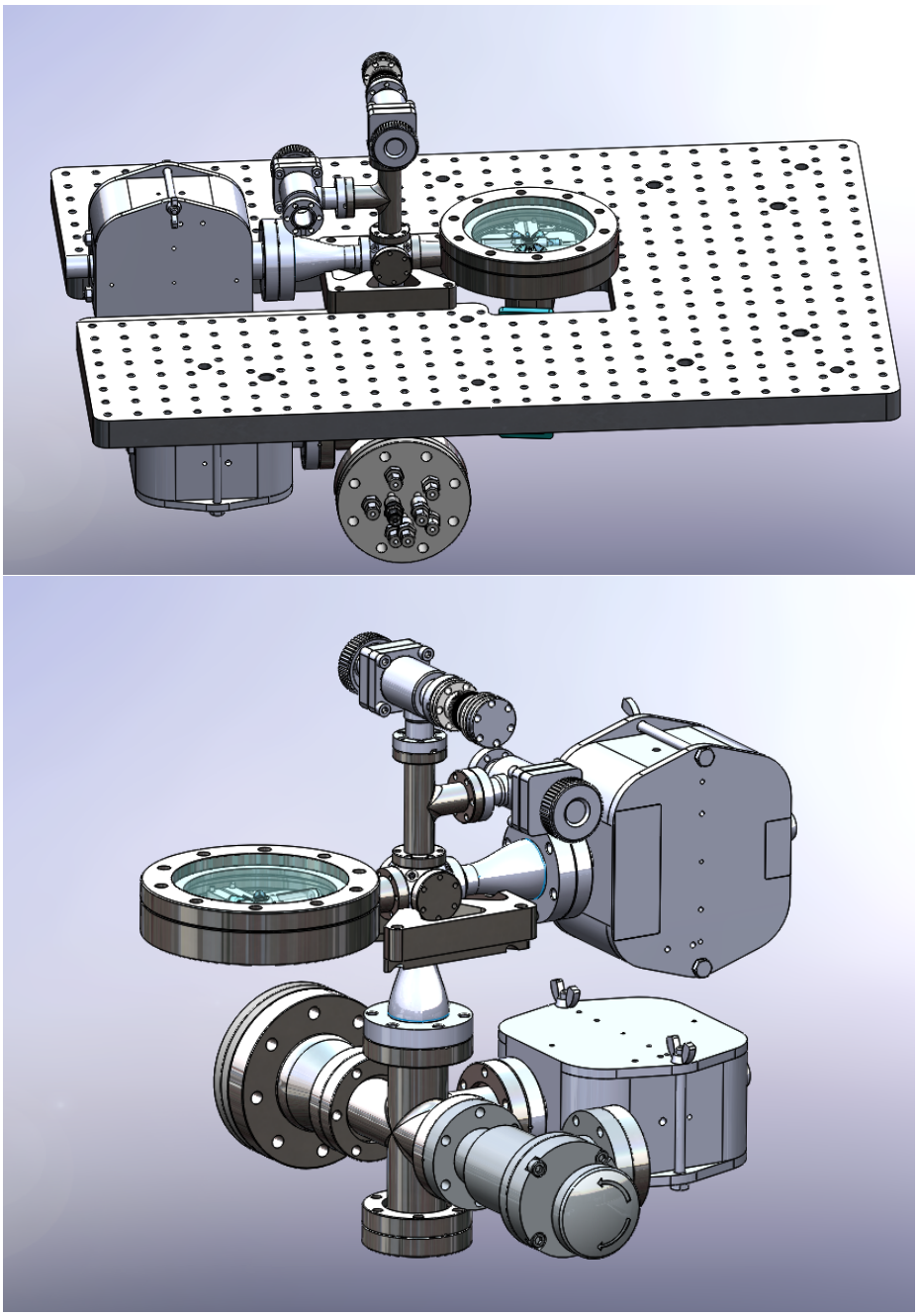

Figure 4.20: Solidworks models of Quantum node design.

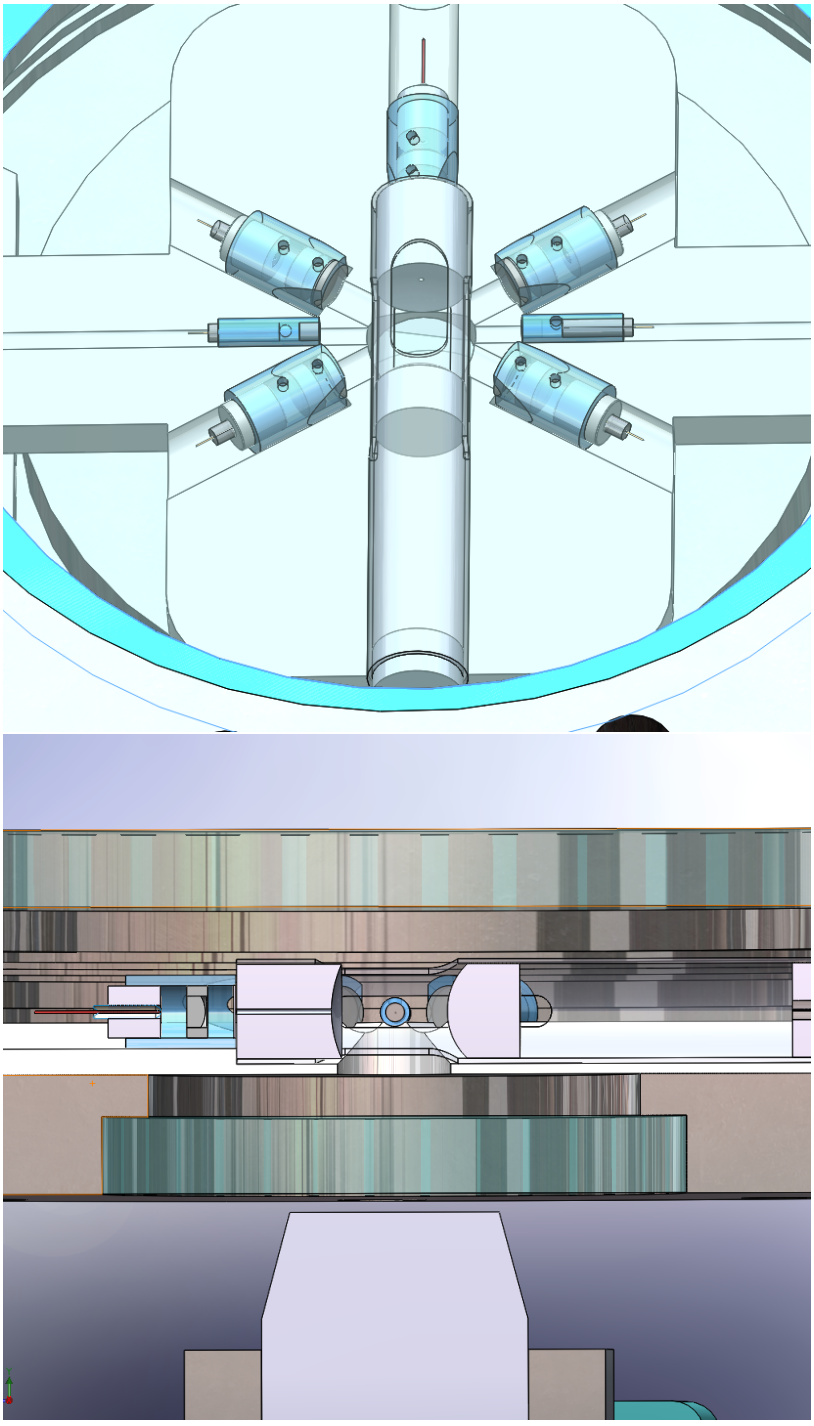

Figure 4.21: Solidworks models of first generation quantum node using a high-NA parabolic mirror to collection photons. Entire apparatus sits inside of a pancake cell. 4 out of 6 MOT lasers and trapping lasers are all launch from optics integrated onto the chip.

Table 4.2: Atom-photon CQED experiments demonstrating remote entanglement of matter qubits. Additional remote entanglement protocols demonstrated between ensemble quantum memories[11, 78] and with superconducting qubits and microwave fields[49] are not included in the table.

Year	research group	description	qubit	rate (s^{-1})	fidelity
2007	Monroe [47]	remote ion-ion entanglement	$^{171}Yb^{+}$	0.0020	0.63
2008	Monroe [44]	remote ion-ion entanglement	$^{171}Yb^{+}$	0.026	0.81
2012	Rempe [57]	remote quantum state transfer and entanglement	^{87}Rb	100	0.85
2012	Weinfurter [29]	atom-atom entanglement	^{87}Rb	0.0094	0.81
2013	Blatt [72]	ion-ion entanglement by photon detection	$^{138}Ba^{+}$	0.23	0.64
2013	Hanson [7]	remote spin-spin entanglement	NV center	0.0017	0.68
2015	Monroe [33]	remote two ion-ion "modular" entanglement	$^{171}Yb^{+}$	4.5	0.78
2016	Imamoğlu [14]	remote entanglement hole spins	hole q. dots	2300.	0.55
2017	Weinfurter [60]	atom-atom entanglement, loophole free Bell test	^{87}Rb	~ 0.03	~ 0.85
2017	Atatüre [74]	remote spin-spin entanglement	InGaAs q. dot	7300.	0.62
2020	Lucas [73]	ion-ion entanglement	$^{88}Sr^{+}$	182	0.94
2021	Hanson [54]	3 node network	NV center	9	0.81

to data qubits, which will enable measurement based error correction protocols[8]. A variety of approaches are possible for mediating atom-photon entanglement in each node[77, 57, 76], including the use of Rydberg states to provide directional single photon emission[64, 66, 42, 53, 24]. Fig 4.22 shows examples of how these dual-species systems might look. Another future goal is to continue to raise the atom-atom entanglement generation rate. As was mentioned in sec 4.6, the initial rate of atom-atom entanglement generation that we expect to achieve with the full near-concentric cavity quantum node design is 1700Hz. When comparing to other similar experiments, like those listed in Table 4.2, a rate entanglement generation of 1700Hz exceeds the rates that have been demonstrated thus far on atom or ion based architectures. However looking further into the future, it will desirable to have atom-atom entanglement generation rates in the several to tens of kHz range for a

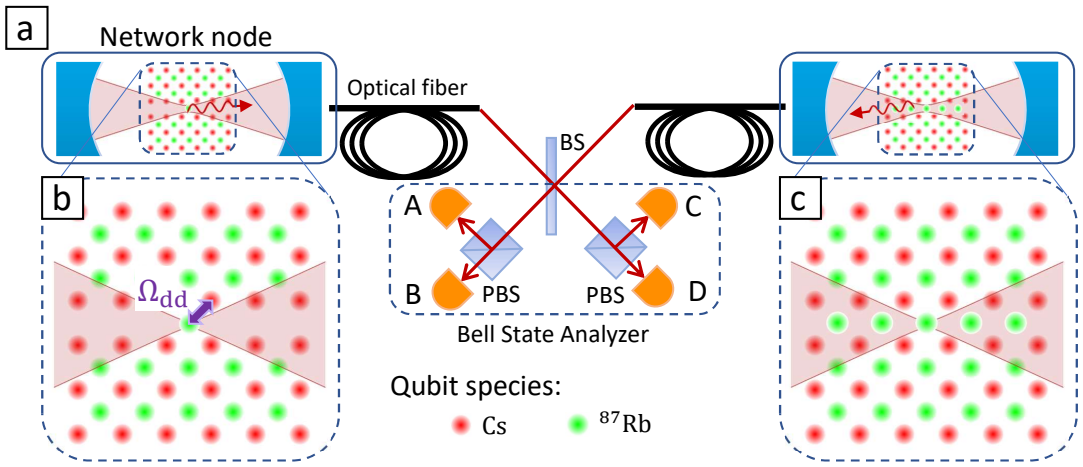

Figure 4.22: Illustration of a two-node quantum network. Two neutral-atom quantum registers are connected by a photonic link. Entanglement between a register atom and the single Rb atom at each node is mediated by Rydberg interactions, indicated by Ω_{dd}. Coherent scattering of photons from the single Rb atoms results in atom-photon entanglements at each node, which are projected onto atom-atom entanglement upon an interference at the Bell state analyzer (BSA).

distributed quantum network. Further increase of the entanglement rate will require not only increasing the photon collection efficiency, but also faster photon detection, and likely switching to a telecom wavelength photon. This can be done either by photon down-conversion to 1540[2] or by using a different excitation scheme[35].

Chapter 5

Conclusion and Outlook

In this thesis, I presented a design and theoretical justification for building a duel-species neutral atom quantum network node. Using the properties of resonant optical cavities, the photon collection efficiency can be enhanced far beyond free-space optics. This can potentially allow for much faster atom-atom entanglement rates than have been demonstrated thus far with atoms.While we have not yet developed the techniques for building and aligning the near concentric cavities, we will be building off the work of others [51]. Furthermore, as was argued in section 4, we believe that this configuration, which will be our second generation node, will yield much better results than the first version being constructed now, which uses a high NA lens. We have already started the process of designing, constructing, and assembling the first version, and plan to have it completed by the end of 2022, at which time the characterization of the system can start while the second iteration starts construction and testing.

Additionally, I have presented the work that I have done towards progressing the Rb-ensemble experiment. In it's previous life, the Rb-ensemble experiment was very successful, and the rebuild was intended to update the experiment in a way that would allow it to continue to do interesting and relevant science. However due to

many persistent technical issues, which I have outlined in this thesis, we were not able to restore functionality to the experiment after the rebuild before our Rb87 atoms ran out. That being said, a lot was learned through this process of trail and error and it is my hope that some of what is written here may help others who are having similar problems.

Appendix A

Appendices

A.1 Optical Diagrams

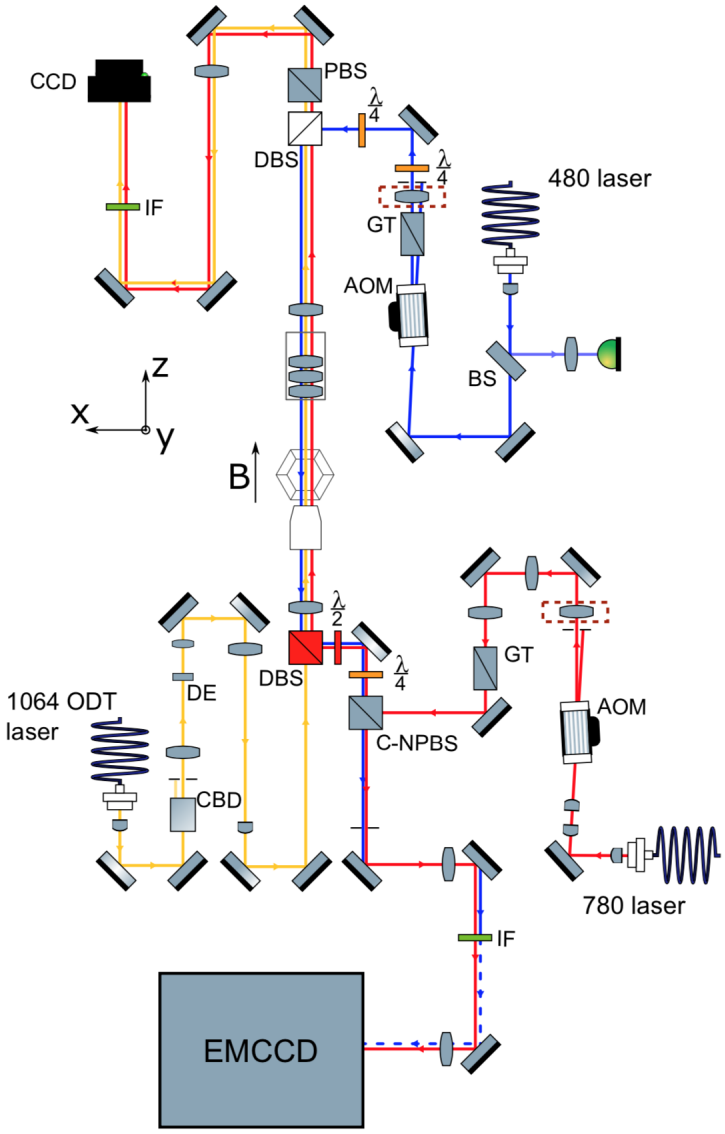

Figure A.1: Optical diagram of Rb Ensemble experiment. Source of Diagram is Matt Ebert's Thesis [17]

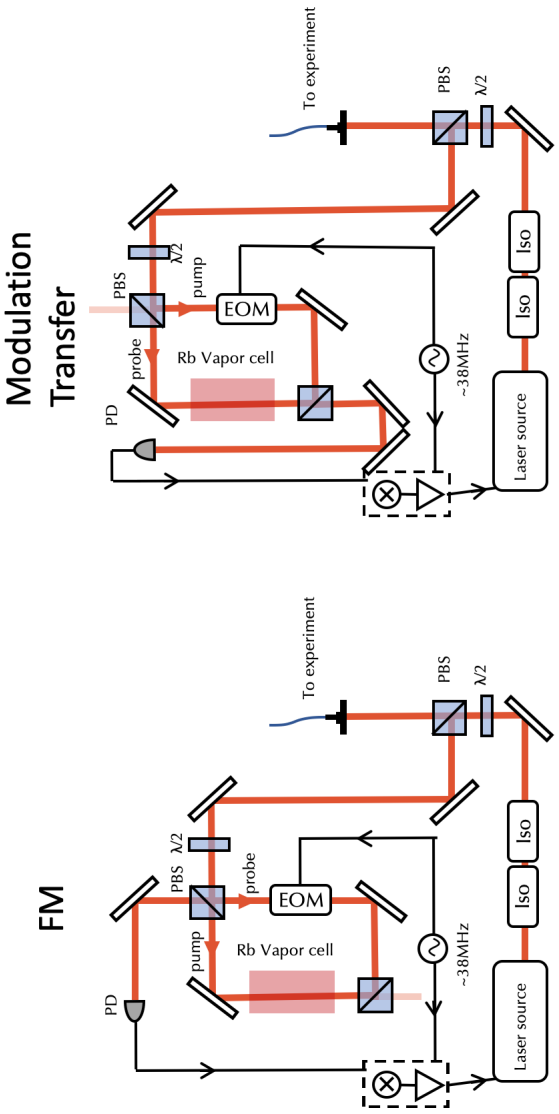

Figure A.2: Optical diagrams Modulation Transfer and Frequency modulation spectroscopy used for the cooling light, repumper, and optical pumping

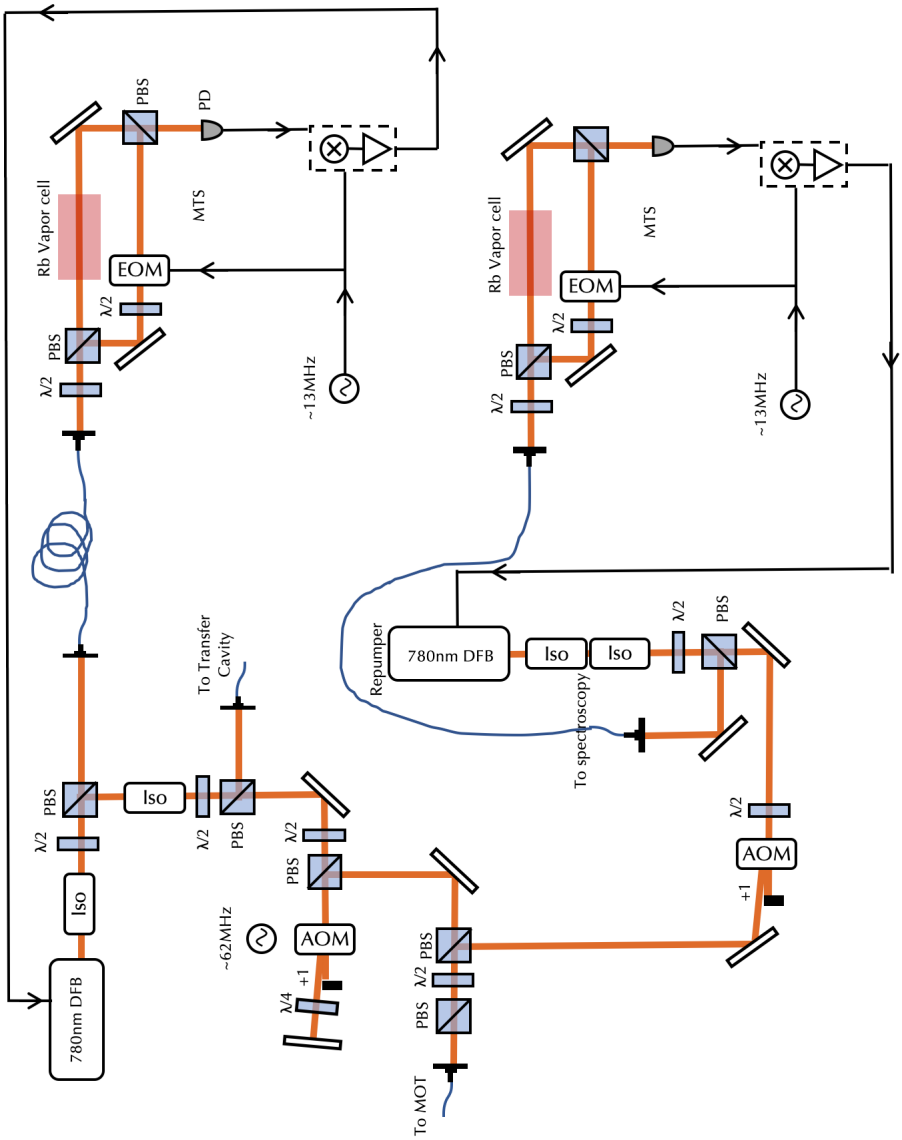

Figure A.3: Optical diagram of the MOT laser optics

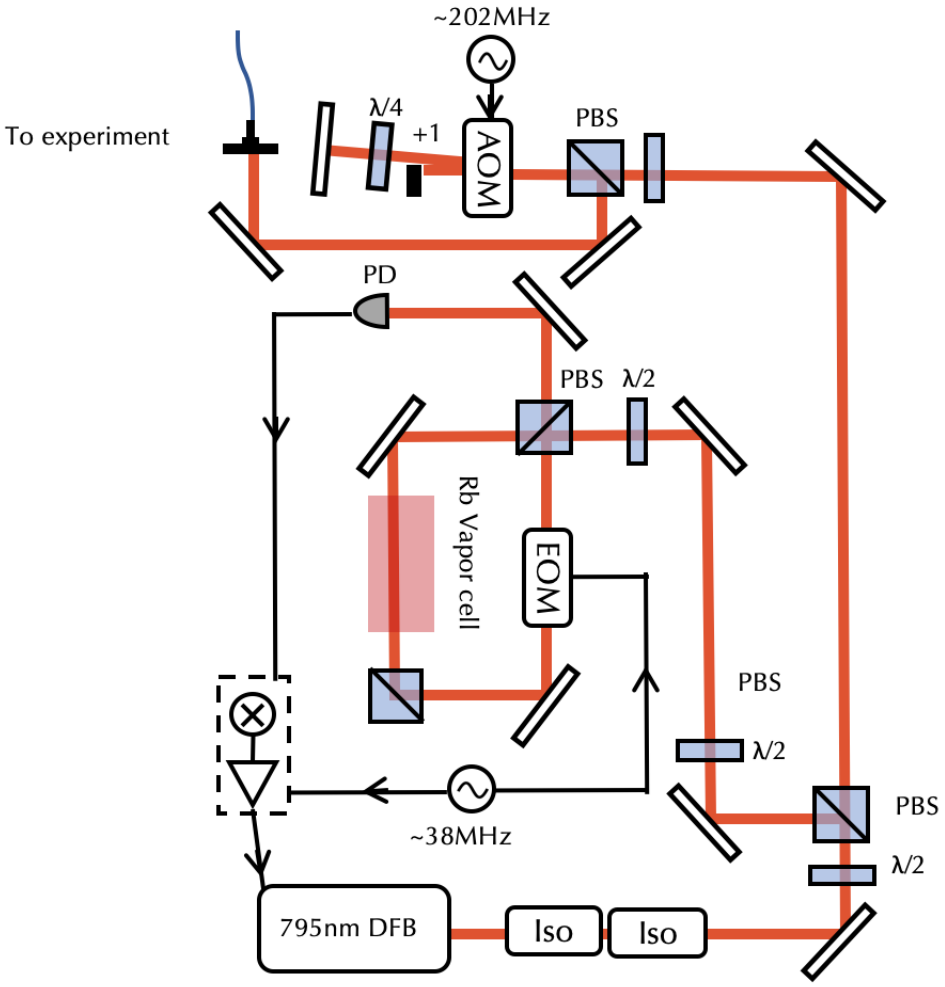

Figure A.4: Optical diagram of the optical pumping laser optics

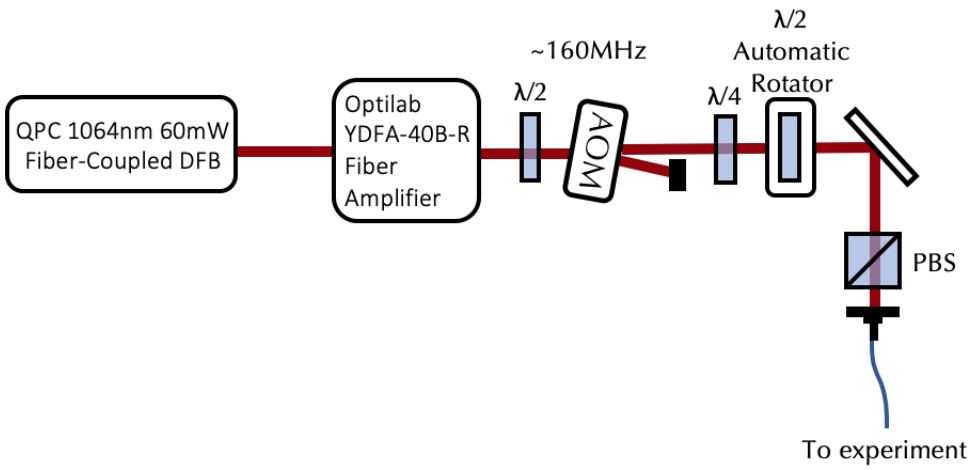

Figure A.5: Optical diagram of the 1064 dipole trap laser optics

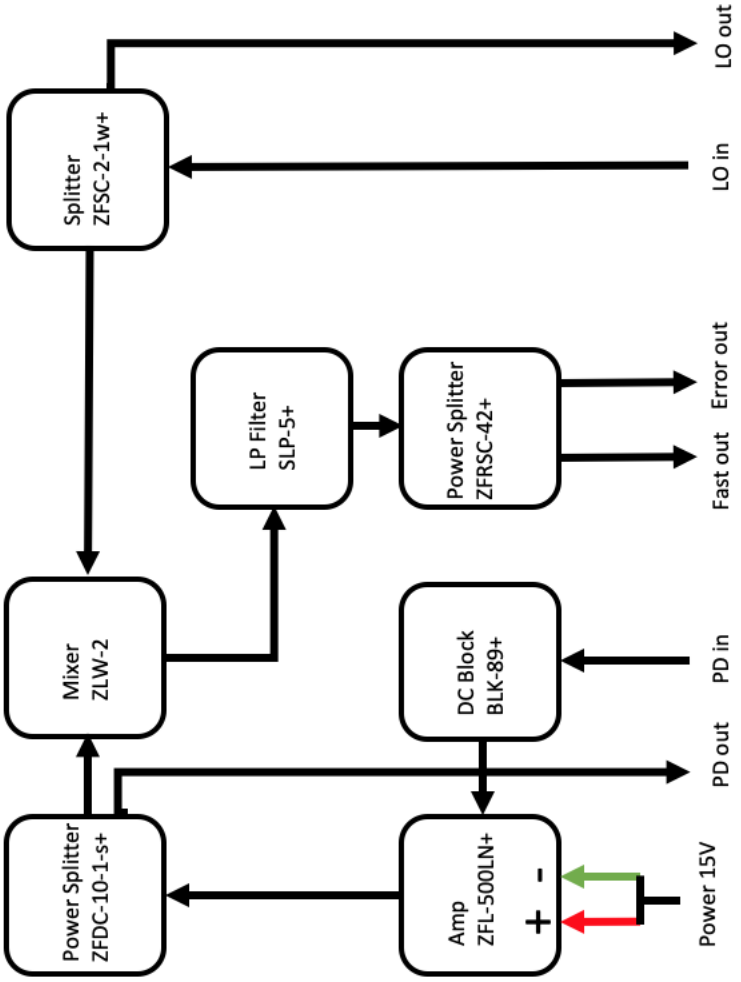

Figure A.6: Schematic of the PDH lock RF components used to lock to the ULE cavity

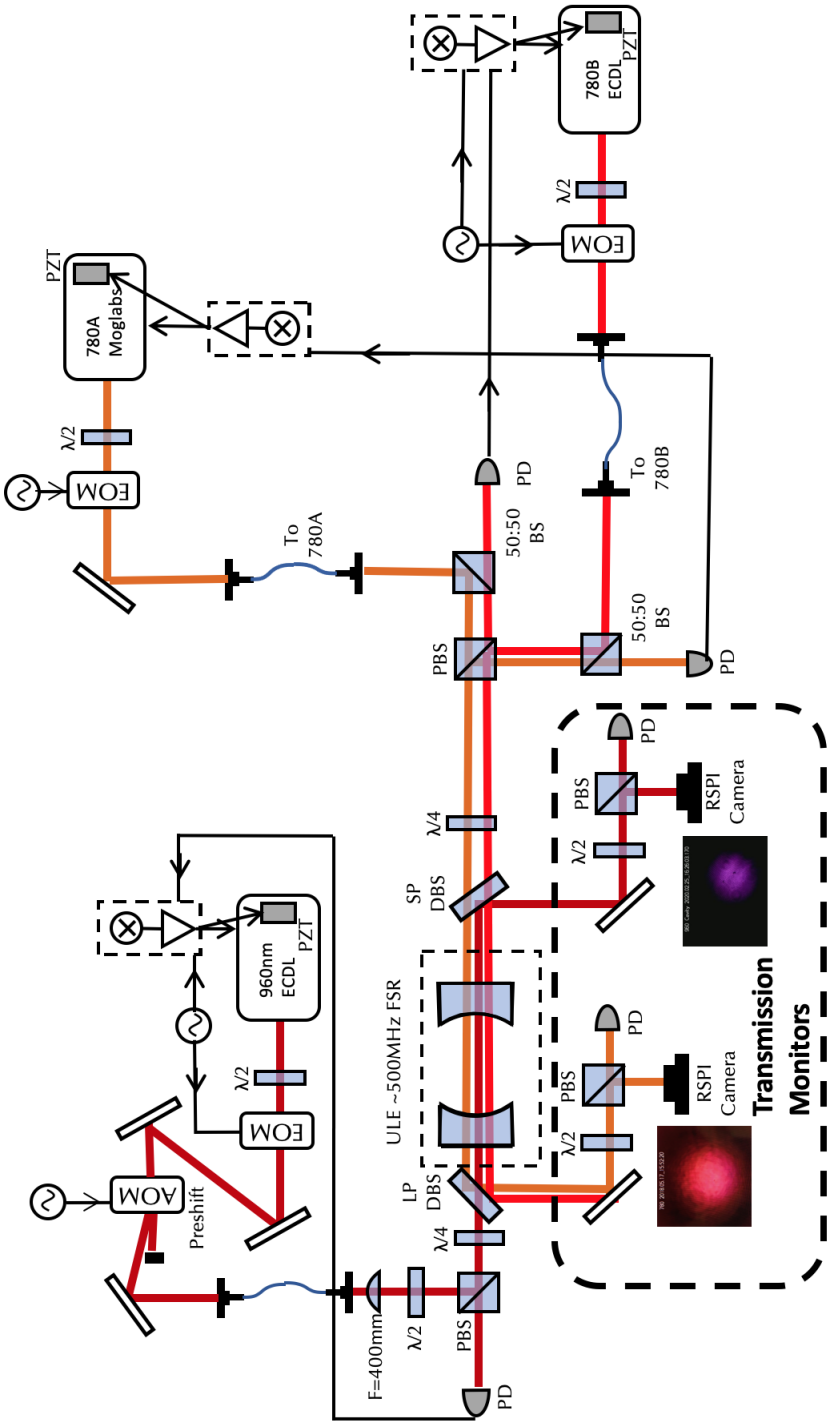

Figure A.7: Full layout of Rydberg laser optics

A.2 AAS extra images

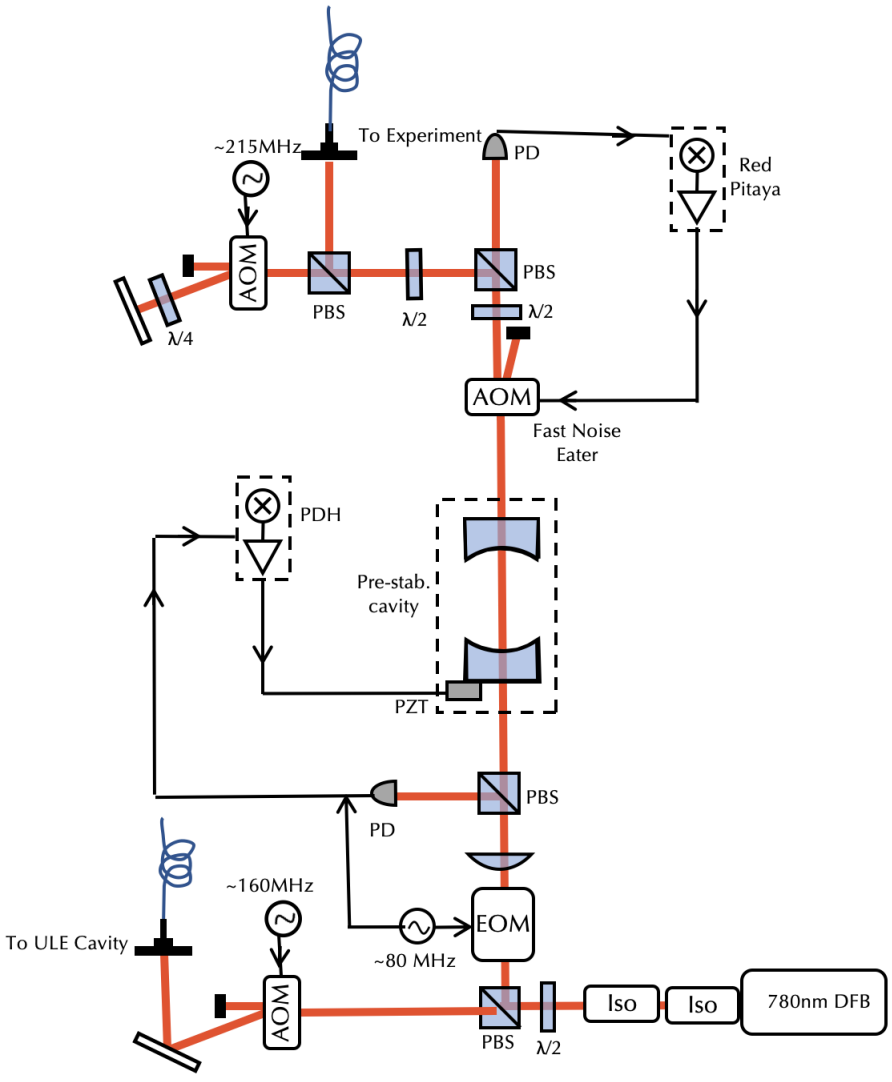

Figure A.8: Layout of Rydberg laser filter optics

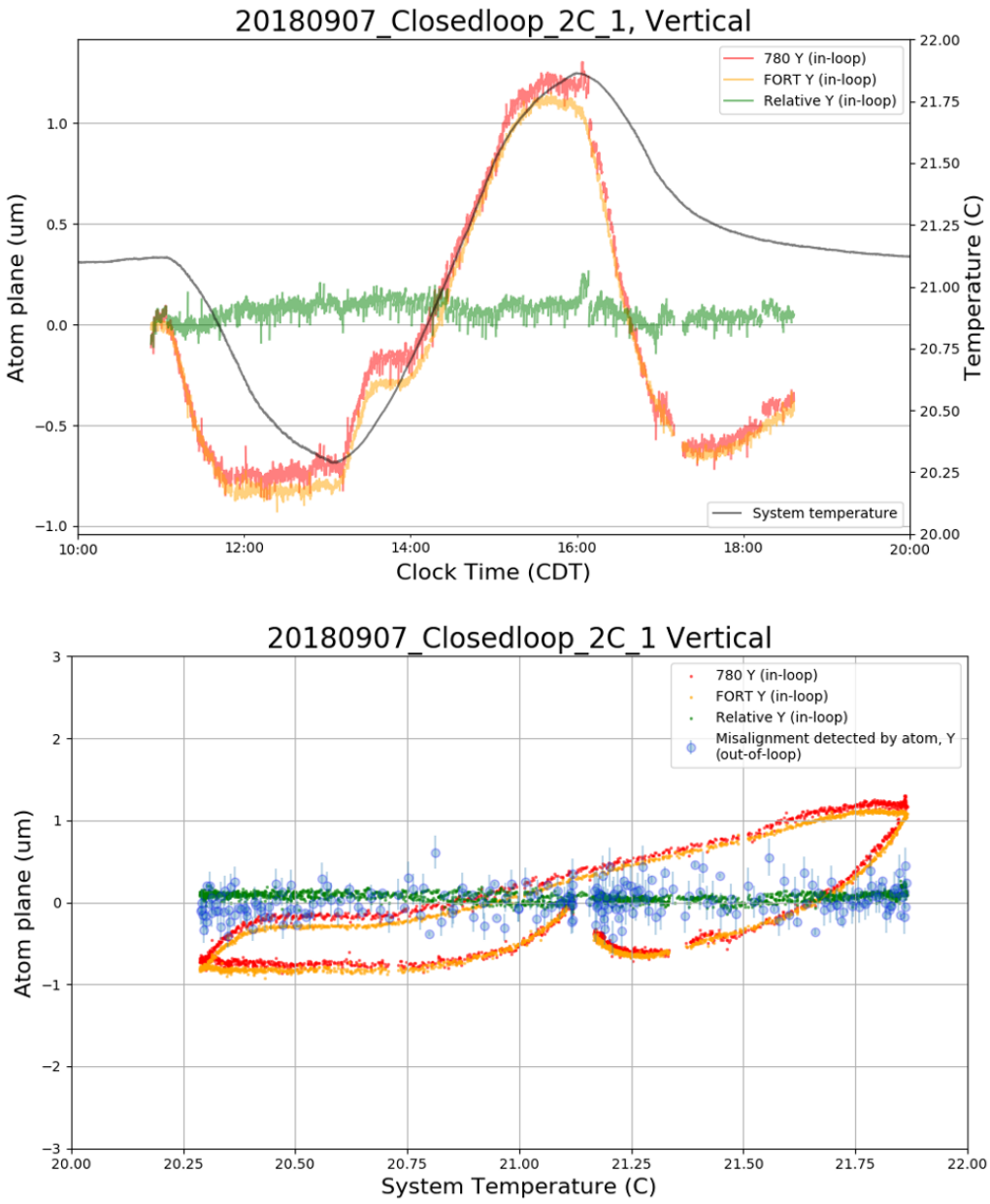

Figure A.9: Time vs Vertical Displacement, and Temperature vs Vertical Displacement graphs for the AAS closed loop data collected on 9/9/2018. Displacement at atoms was measured using a Ramsey fringe

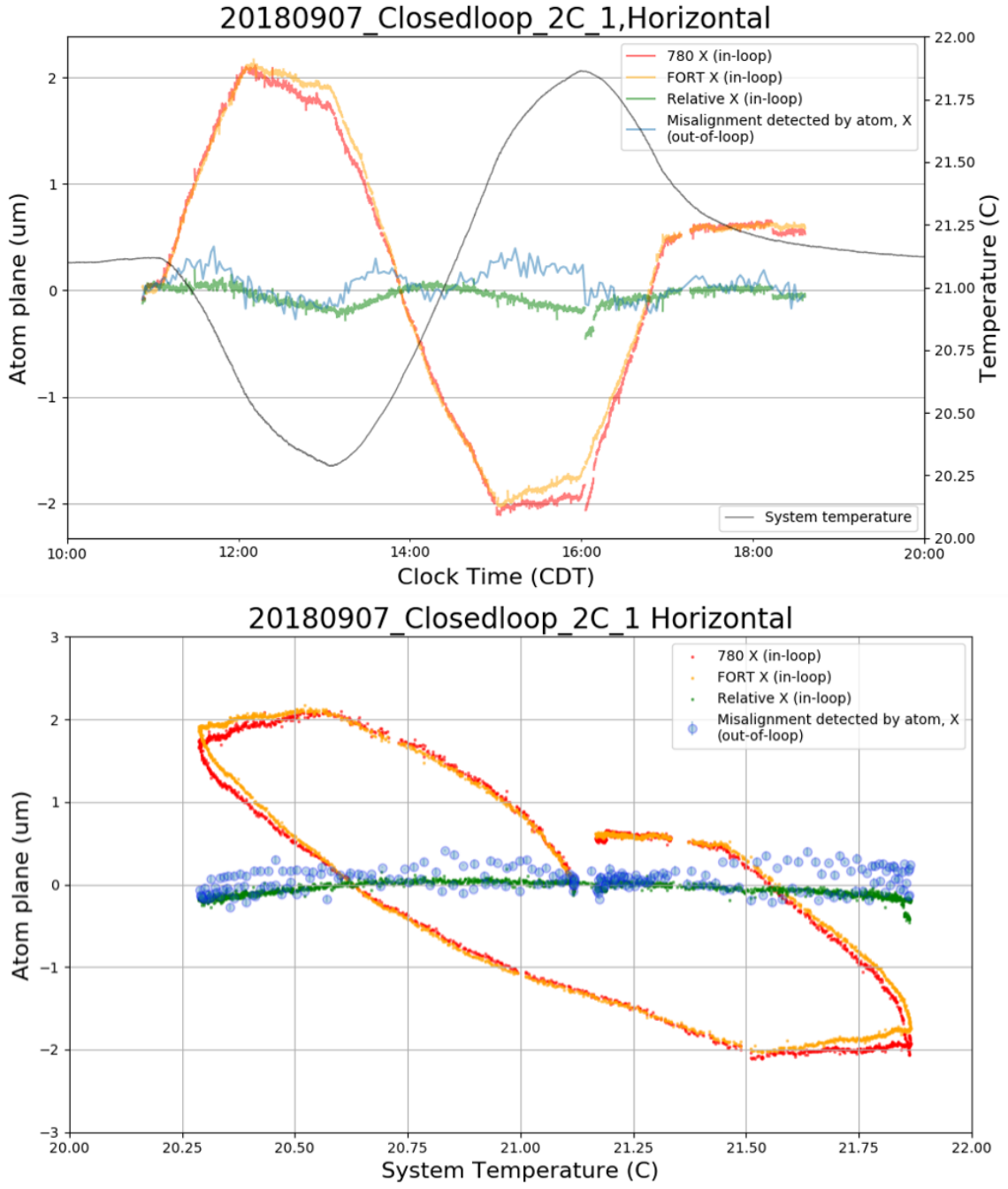

Figure A.10: Time vs Horizontal Displacement, and Temperature vs Horizontal Displacement graphs for the AAS closed loop data collected on 9/9/2018. Displacement at atoms was measured using a Ramsey fringe

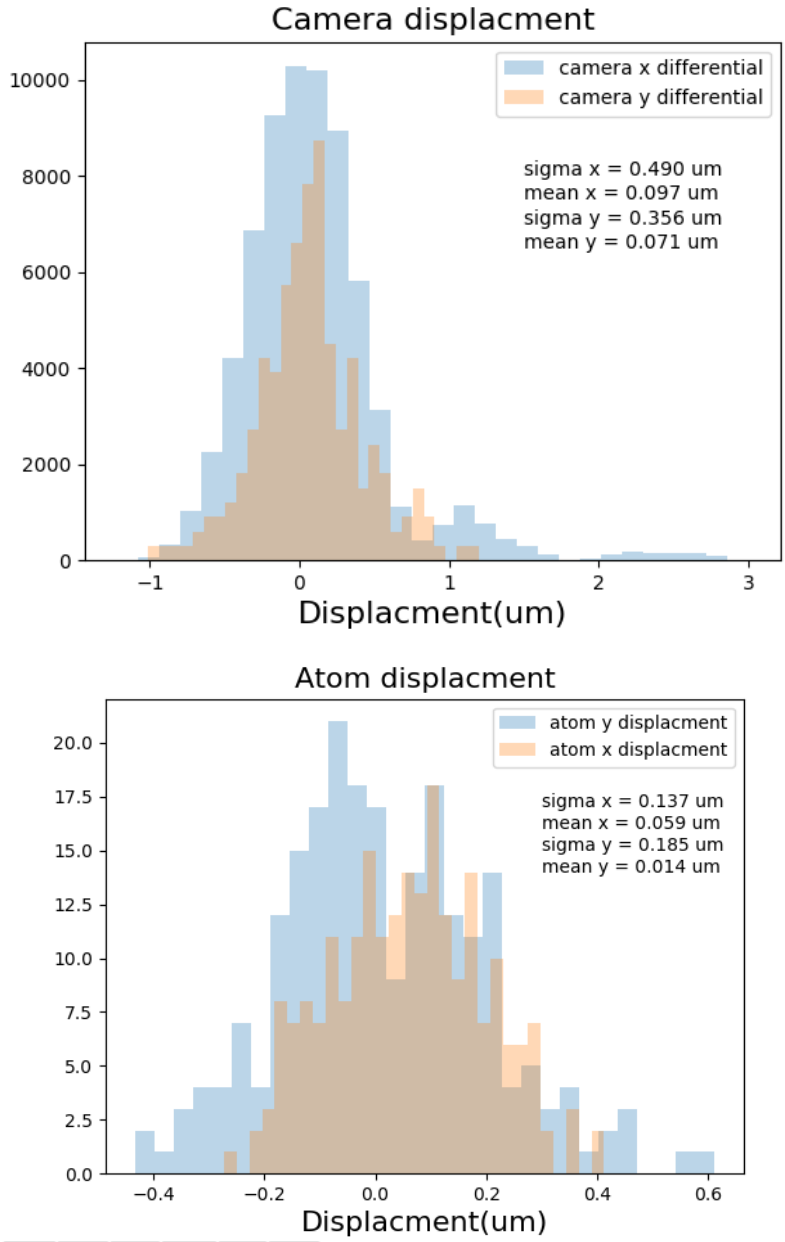

Figure A.11: Histograms showing the measured displacement of the FORT and 780 addressing beams as measured on the CCD camera and at the atoms using a Ramsey fringe for data collected on 9/9/2018

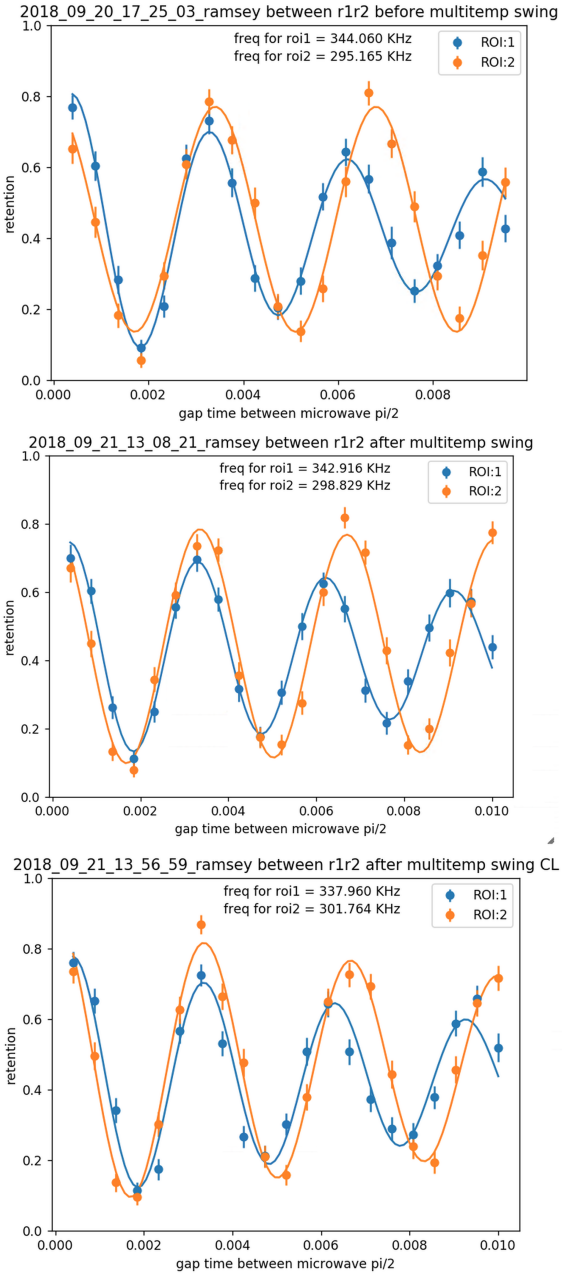

Figure A.12: Data showing that near the end of our testing of the Automatic alignment system, the passive resistance to hysteresis from temperature fluctuations had become so good that we could no longer discern a statistical difference from the closed loop

Bibliography

[1]

[2] B. Albrecht, P. Farrera, X. Fernandez-Gonzalvo, M. Cristiani, and H. de Riedmatten. A waveguide frequency converter connecting rubidium-based quantum memories to the telecom C-band. *Nat. Commun.*, 5:3376, 2014.

[3] David Alexander Anderson, Rachel Elizabeth Sapiro, and Georg Raithel. An atomic receiver for am and fm radio communication. *IEEE Transactions on Antennas and Propagation*, 69(5):2455–2462, May 2021.

[4] F. Arute and et. al. Quantum supremacy using a programmable superconducting processor. *Nature*, 574:505, 2019.

[5] A. Asenjo-Garcia, M. Moreno-Cardoner, A. Albrecht, H. J. Kimble, and D. E. Chang. Exponential improvement in photon storage fidelities using subradiance and "selective radiance" in atomic arrays. *Phys. Rev. X*, 7:031024, 2017.

[6] Daniel Barredo, Vincent Lienhard, Sylvain de Léséleuc, Thierry Lahaye, and Antoine Browaeys. Synthetic three-dimensional atomic structures assembled atom by atom. *Nature*, 561:79, 2018.

[7] H. Bernien, B. Hensen, W. Pfaff, G. Koolstra, M. S. Blok, L. Robledo, T. H. Taminiau, M. Markham, D. J. Twitchen, L. Childress, and R. Hanson. Her-

alded entanglement between solid-state qubits separated by three metres. *Nature*, 497:86, 2013.

[8] I. I. Beterov and M. Saffman. Rydberg blockade, Förster resonances, and quantum state measurements with different atomic species. *Phys. Rev. A*, 92:042710, 2015.

[9] A. Browaeys, D. Barredo, and T. Lahaye. Experimental investigations of dipole-dipole interactions between a few Rydberg atoms. *J. Phys. B: At. Mol. Opt. Phys.*, 49:152001, 2016.

[10] A. Browaeys and T. Lahaye. Many-body physics with individually controlled Rydberg atoms. *Nat. Phys.*, 16:132, 2020.

[11] Goban A. Papp S. et al Choi, K. Entanglement of spin waves among four quantum memories. *Nature*, 468:412–416, 2010.

[12] Jacob P. Covey, Ivaylo S. Madjarov, Alexandre Cooper, and Manuel Endres. 2000-times repeated imaging of Strontium atoms in clock-magic tweezer arrays. *Phys. Rev. Lett.*, 122:173201, 2019.

[13] Kevin C. Cox, David H. Meyer, Fredrik K. Fatemi, and Paul D. Kunz. Quantum-limited atomic receiver in the electrically small regime. *Phys. Rev. Lett.*, 121:110502, Sep 2018.

[14] A. Delteil, Z. Sun, W. b. Gao, E. Togan, S. Faelt, and A. Imamoğlu. Generation of heralded entanglement between distant hole spins. *Nat. Phys.*, 12:218, 2016.

[15] T. orević, P. Samutpraphoot, P. L. Ocola, H. Bernien, B. Grinkemeyer, I. Dimitrova, V. Vuletić, and M. D. Lukin. Entanglement transport and a nanophotonic interface for atoms in optical tweezers. *Science*, 373:1511, 2021.

[16] W. Dür, G. Vidal, and J. I. Cirac. Three qubits can be entangled in two inequivalent ways. *Phys. Rev. A*, 62:062314, 2000.

[17] M. Ebert. "neutral atom ensemble qubits and rydberg blockade" ,phd thesis, university of wisconsin-madison, 2017.

[18] M. Ebert, M. Kwon, T. G. Walker, and M. Saffman. Coherence and Rydberg blockade of atomic ensemble qubits. *Phys. Rev. Lett.*, 115:093601, 2015.

[19] M. F. Ebert, M. Kwon, M. Saffman, and T. G. Walker. A CCD based automatic confocal alignment system. 2017. Manuscript in preparation.

[20] K. M. Fortier, S. Y. Kim, M. J. Gibbons, P. Ahmadi, and M. S. Chapman. Deterministic loading of individual atoms to a high-finesse optical cavity. *Phys. Rev. Lett.*, 98:233601, 2007.

[21] J. Gallego, W. Alt, T. Macha, M. Martinez-Dorantes, D. Pandey, and D. Meschede. Strong purcell effect on a neutral atom trapped in an open fiber cavity. *Phys. Rev. Lett.*, 121:173603, Oct 2018.

[22] J. Gallego, W. Alt, T. Macha, M. Martinez-Dorantes, D. Pandey, and D. Meschede. Strong Purcell effect on a neutral atom trapped in an open fiber cavity. *Phys. Rev. Lett.*, 121:173603, 2018.

[23] S. Garcia, D. Maxein, L. Hohmann, J. Reichel, and R. Long. Fiber-pigtailed optical tweezer for single-atom trapping and single-photon generation. *Applied Physics Letters*, 103(11):114103, Sep 2013.

[24] A. Grankin, P. O. Guimond, D. V. Vasilyev, B. Vermersch, and P. Zoller. Free-space photonic quantum link and chiral quantum optics. *Phys. Rev. A*, 98:043825, 2018.

[25] D. M. Harber, H. J. Lewandowski, J. M. McGuirk, and E. A. Cornell. Effect of cold collisions on spin coherence and resonance shifts in a magnetically trapped ultracold gas. *Phys. Rev. A*, 66:053616, 2002.

[26] G. Hickman, M. Ebert, T. Graham, X. Jiang, S. Vanga, C. Vollbrecht, R. Goldsmith, and M. Saffman. Progress towards a dual species atomic quantum repeater node using a high-finesse fiber resonator. *Bull. Am. Phys. Soc., DAMOP*, page E01.00093, 2019.

[27] G. T. Hickman and M. Saffman. Speed, retention loss, and motional heating of atoms in an optical conveyor belt. *Phys. Rev. A*, 101:063411, 2020.

[28] J. E. Hoffman, J. A. Grover, Z. Kim, A. K. Wood, J. R. Anderson, A. J. Dragt, M. Hafezi, C. J. Lobb, L. A. Orozco, S. L. Rolston, J. M. Taylor, C. P. Vlahacos, and F. C. Wellstood. Atoms talking to SQUIDs. *Rev. Mex. Fisica*, 57:1, 2011.

[29] J. Hofmann, M. Krug, N. Ortegel, L. Gérard, M. Weber, W. Rosenfeld, and H. Weinfurter. Heralded entanglement between widely separated atoms. *Science*, 337:72–75, 2012.

[30] Julian Hofmann, Michael Krug, Norbert Ortegel, Lea Gérard, Markus Weber, Wenjamin Rosenfeld, and Harald Weinfurter. Heralded entanglement between widely separated atoms. *Science (New York, N.Y.)*, 337:72–5, 07 2012.

[31] Christopher Holloway, Matthew Simons, and Joshua Gordon. A multi-band rydberg-atom based receiver/antenna: Am/fm stereo reception. 2020-04-02 2020.

[32] C. K. Hong, Z. Y. Ou, and L. Mandel. Measurement of subpicosecond time intervals between two photons by interference. *Phys. Rev. Lett.*, 59:2044–2046, 1987.

[33] D. Hucul, I. V. Inlek, G. Vittorini, C. Crocker, S. Debnath, S. M. Clark, and C. Monroe. Modular entanglement of atomic qubits using photons and phonons. *Nat. Phys.*, 11:37, 2015.

[34] W. Huie, S. G. Menon, H. Bernien, and J. P. Covey. Multiplexed telecommunication-band quantum networking with atom arrays in optical cavities. *Phys. Rev. Research*, 3:043154, 2021.

[35] William Huie, Shankar G. Menon, Hannes Bernien, and Jacob P. Covey. Multiplexed telecommunication-band quantum networking with atom arrays in optical cavities. *Physical Review Research*, 3(4), Dec 2021.

[36] Calil Kores C. Geskus D. Pollnau M. Ismail, N. The fabry-pérot resonator: Spectral line shapes, generic and related airy distributions, linewidths, finesses, and performance at low or frequency-dependent reflectivity. *Optics Express*, 4(15):16366–16389, 2016.

[37] J.D. Jackson. *Classical electrodynamics*. Wiley, New York, 3 edition, 1998.

[38] D. F. V James, P. G. Kwiat, W. J. Munro, and A. G. White. Measurement of qubits. *Phys. Rev. A*, 64:052312, 2001.

[39] E. T. Jaynes and F. W. Cummings. Comparison of quantum and semiclassical radiation theories with application to the beam maser. *Proc. IEEE*, 51:89, 1963.

[40] A. Kawasaki, B. Braverman, E. Pedrozo-Peñafiel, C. Shu, S. Colombo, Z. Li, Ö. Özel, W. Chen, L. Salvi, A. Heinz, D. Levonian, D. Akamatsu, Y. Xiao, and V. Vuletić. Geometrically asymmetric optical cavity for strong atom-photon coupling. *Phys. Rev. A*, 99:013437, 2019.

[41] M. Kwon. "rydberg-mediated atomic ensemble entanglement and hyperfine qubit detection" ,phd thesis, university of wisconsin-madison, 2019.

[42] L. Li, Y. O. Dudin, and A. Kuzmich. Entanglement between light and an optical atomic excitation. *Nature*, 498:466, 2013.

[43] M. D. Lukin, M. Fleischhauer, R. Cote, L. M. Duan, D. Jaksch, J. I. Cirac, and P. Zoller. Dipole blockade and quantum information processing in mesoscopic atomic ensembles. *Phys. Rev. Lett.*, 87:037901, 2001.

[44] D. N. Matsukevich, P. Maunz, D. L. Moehring, S. Olmschenk, and C. Monroe. Bell inequality violation with two remote atomic qubits. *Phys. Rev. Lett.*, 100:150404, 2008.

[45] S. G. Menon, K. Singh, J. Borregaard, and H. Bernien. Nanophotonic quantum network node with neutral atoms and an integrated telecom interface. *New J. Phys.*, 22:073033, 2020.

[46] H. J. Metcalf and P. van der Straten. *Laser cooling and trapping*. Springer-Verlag, New York, 1999.

[47] D. L. Moehring, P. Maunz, S. Olmschenk, K. C. Younge, D. N. Matsukevich, L.-M. Duan, and C. Monroe. Entanglement of single-atom quantum bits at a distance. *Nature*, 449:68, 2007.

[48] C. Monroe, R. Raussendorf, A. Ruthven, K. R. Brown, P. Maunz, L.-M. Duan, and J. Kim. Large-scale modular quantum-computer architecture with atomic memory and photonic interconnects. *Phys. Rev. A*, 89:022317, 2014.

[49] A. Narla, S. Shankar, M. Hatridge, Z. Leghtas, K. M. Sliwa, E. Zalys-Geller, S. O. Mundhada, W. Pfaff, L. Frunzio, R. J. Schoelkopf, and M. H. Devoret. Robust concurrent remote entanglement between two superconducting qubits. *Phys. Rev. X*, 6:031036, 2016.

[50] C. H. Nguyen, A. N. Utama, N. Lewty, K. Durak, G. Maslennikov, S. Straupe, M. Steiner, and C. Kurtsiefer. Single atoms coupled to a near-concentric cavity. *Phys. Rev. A*, 96:031802, 2017.

[51] Chi Huan Nguyen, Adrian Nugraha Utama, Nick Lewty, Kadir Durak, Gleb Maslennikov, Stanislav Straupe, Matthias Steiner, and Christian Kurtsiefer. Single atoms coupled to a near-concentric cavity. *Phys. Rev. A*, 96:031802, Sep 2017.

[52] M. A. Norcia, A. W. Young, W. J. Eckner, E. Oelker, J. Ye, and A. M. Kaufman. Seconds-scale coherence on an optical clock transition in a tweezer array. *Science*, 366:93, 2019.

[53] D. Petrosyan and K. Mølmer. Deterministic free-space source of single photons using Rydberg atoms. *Phys. Rev. Lett.*, 121:123605, 2018.

[54] M. Pompili, S. L. N. Hermans, S. Baier, H. K. C. Beukers, P. C. Humphreys, R. N. Schouten, R. F. L. Vermeulen, M. J. Tiggelman, L. dos Santos Martins, B. Dirkse, S. Wehner, and R. Hanson. Realization of a multinode quantum network of remote solid-state qubits. *Science*, 372:259, 2021.

[55] E. Purcell. Spontaneous emission probabilities at radio frequencies. *Phys. Rev.*, 69:681, 1946.

[56] A. Reiserer and G. Rempe. Cavity-based quantum networks with single atoms and optical photons. *Rev. Mod. Phys.*, 87:1379, 2015.

[57] S. Ritter, C. Nölleke, C. Hahn, A. Reiserer, A. Neuzner, M. Uphoff, M. Mücke, E. Figueroa, J. Bochmann, and G. Rempe. An elementary quantum network of single atoms in optical cavities. *Nature*, 484:195–200, 2012.

[58] C. Robens, J. Zopes, W. Alt, S. Brakhane, D. Meschede, and A. Alberti. Low-entropy states of neutral atoms in polarization-synthesized optical lattices. *Phys. Rev. Lett.*, 118:065302, 2017.

[59] Carsten Robens, Stefan Brakhane, Wolfgang Alt, Felix Kleißler, Dieter Meschede, Geol Moon, Gautam Ramola, and Andrea Alberti. High numerical aperture (na = 092) objective lens for imaging and addressing of cold atoms. *Optics Letters*, 42(6):1043, Mar 2017.

[60] W. Rosenfeld, D. Burchardt, R. Garthoff, K. Redeker, N. Ortegel, M. Rau, and H. Weinfurter. Event-ready Bell test using entangled atoms simultaneously closing detection and locality loopholes. *Phys. Rev. Lett.*, 119:010402, 2017.

[61] Wenjamin Rosenfeld, Daniel Burchardt, Robert Garthoff, Kai Redeker, Norbert Ortegel, Markus Rau, and Harald Weinfurter. Event-ready bell test using entangled atoms simultaneously closing detection and locality loopholes. *Phys. Rev. Lett.*, 119:010402, Jul 2017.

[62] M. Saffman, I. I. Beterov, A. Dalal, E. J. Paez, and B. C. Sanders. Symmetric Rydberg c_z gates with adiabatic pulses. *arXiv:1912.02977*, 2019.

[63] M. Saffman and K. Mølmer. Scaling the neutral-atom Rydberg gate quantum computer by collective encoding in Holmium atoms. *Phys. Rev. A*, 78:012336, 2008.

[64] M. Saffman and T. G. Walker. Creating single-atom and single-photon sources from entangled atomic ensembles. *Phys. Rev. A*, 66:065403, 2002.

[65] M. Saffman and T. G. Walker. Analysis of a quantum logic device based on dipole-dipole interactions of optically trapped Rydberg atoms. *Phys. Rev. A*, 72:022347, 2005.

[66] M. Saffman and T. G. Walker. Entangling single- and N-atom qubits for fast quantum state detection and transmission. *Phys. Rev. A*, 72:042302, 2005.

[67] M. Saffman, T. G. Walker, and K. Mølmer. Quantum information with Rydberg atoms. *Rev. Mod. Phys.*, 82:2313, 2010.

[68] J. J. Sakurai. *Modern Quantum Mechanics*. Addison-Wesley, 1994.

[69] S. Saskin, J. T. Wilson, B. Grinkemeyer, and J. D. Thompson. Narrow-line cooling and imaging of Ytterbium atoms in an optical tweezer array. *Phys. Rev. Lett.*, 122:143002, 2019.

[70] P. W. Shor. Algorithms for quantum computation: Discrete logarithms and factoring. *in Proc. 35th Annual Symposium on Foundations of Computer Science, IEEE Computer Society Press*, pages 124–134, 1994.

[71] Anthony E Siegman. *Lasers*. University Science Books, 1986.

[72] L. Slodička, G. Hétet, N. Röck, P. Schindler, M. Hennrich, and R. Blatt. Atom-atom entanglement by single-photon detection. *Phys. Rev. Lett.*, 110:083603, 2013.

[73] L. J. Stephenson, D. P. Nadlinger, B. C. Nichol, S. An, P. Drmota, T. G. Ballance, K. Thirumalai, J. F. Goodwin, D. M. Lucas, and C. J. Ballance. High-rate, high-fidelity entanglement of qubits across an elementary quantum network. *Phys. Rev. Lett.*, 124:110501, 2020.

[74] R. Stockill, M. J. Stanley, L. Huthmacher, E. Clarke, M. Hugues, A. J. Miller, C. Matthiesen, C. Le Gall, and M. Atatüre. Phase-tuned entangled state generation between distant spin qubits. *Phys. Rev. Lett.*, 119:010503, 2017.

[75] P. Treutlein, P. Hommelhoff, T. Steinmetz, T. W. Hänsch, and J. Reichel. Coherence in microchip traps. *Phys. Rev. Lett.*, 92:203005, 2004.

[76] M. Uphoff, M. Brekenfeld, G. Rempe, and S. Ritter. An integrated quantum repeater at telecom wavelength with single atoms in optical fiber cavities. *Appl. Phys. B*, 122:46, 2016.

[77] J. Volz, M. Weber, D. Schlenk, W. Rosenfeld, J. Vrana, K. Saucke, C. Kurtsiefer, and H. Weinfurter. Observation of entanglement of a single photon with a trapped atom. *Phys. Rev. Lett.*, 96:030404, 2006.

[78] Y. Yu, F. Ma, X.-Y. Luo, B. Jing, P.-F. Sun, R.-Z. Fang, C.-W. Yang, H. Liu, M.-Y. Zheng, X.-P. Xie, W.-J. Zhang, L.-X. You, Z. Wang, T.-Y. Chen, Q. Zhang, X.-H. Bao, and J.-W. Pan. Entanglement of two quantum memories via fibres over dozens of kilometres. *Nature*, 578:240, 2020.

[79] Yong Zeng, Peng Xu, Xiaodong He, Yangyang Liu, Min Liu, Jin Wang, D. J. Papoular, G. V. Shlyapnikov, and Mingsheng Zhan. Entangling two individual atoms of different isotopes via rydberg blockade. *Phys. Rev. Lett.*, 119:160502, 2017.

[80] Han-Sen Zhong, Hui Wang, Yu-Hao Deng, Ming-Cheng Chen, Li-Chao Peng, Yi-Han Luo, Jian Qin, Dian Wu, Xing Ding, Yi Hu, Peng Hu, Xiao-Yan Yang, Wei-Jun Zhang, Hao Li, Yuxuan Li, Xiao Jiang, Lin Gan, Guangwen Yang, Lixing You, Zhen Wang, Li Li, Nai-Le Liu, Chao-Yang Lu, and Jian-Wei Pan. Quantum computational advantage using photons. *Science*, 370(6523):1460–1463, 2020.